

Washington University in St. Louis

## Washington University Open Scholarship

---

McKelvey School of Engineering Theses & Dissertations

McKelvey School of Engineering

---

Winter 12-15-2021

### Acoustic radiation force and its application for cell manipulation and ion channels activation

Xiangjun Peng

*Washington University in St. Louis*

Follow this and additional works at: [https://openscholarship.wustl.edu/eng\\_etds](https://openscholarship.wustl.edu/eng_etds)



Part of the [Mechanical Engineering Commons](#)

---

#### Recommended Citation

Peng, Xiangjun, "Acoustic radiation force and its application for cell manipulation and ion channels activation" (2021). *McKelvey School of Engineering Theses & Dissertations*. 731.  
[https://openscholarship.wustl.edu/eng\\_etds/731](https://openscholarship.wustl.edu/eng_etds/731)

This Dissertation is brought to you for free and open access by the McKelvey School of Engineering at Washington University Open Scholarship. It has been accepted for inclusion in McKelvey School of Engineering Theses & Dissertations by an authorized administrator of Washington University Open Scholarship. For more information, please contact [digital@wumail.wustl.edu](mailto:digital@wumail.wustl.edu).

WASHINGTON UNIVERSITY IN ST. LOUIS

Department of Biomedical Engineering

Dissertation Examination Committee:

Guy Genin, Chair

Hong Chen

Jianmin Cui

Mark Meacham

Jinyu Shao

Acoustic Radiation Force and its Application for Cell Manipulation and Ion Channels Activation

by

Xiangjun Peng

A dissertation presented to  
The Graduate School  
of Washington University in  
partial fulfillment of the  
requirements for the degree  
of Doctor of Philosophy

December 2021  
St. Louis, Missouri

© 2021, Xiangjun Peng

# Table of Contents

List of Figures .....	v
List of Tables .....	ix
Acknowledgments.....	x
Abstract of the dissertation .....	xiv
Chapter 1: Introduction .....	1
1.1 Harnessing defined acoustic radiation force: a frontier in mechanobiology .....	1
1.2 Acoustic radiation force .....	3
1.3 Ultrasound manipulation on ion channels.....	4
1.4 Plant responses to sound .....	6
1.5 Overview of dissertation .....	7
Chapter 2: The acoustic radiation force of a focused ultrasound beam on a suspended eukaryotic cell.....	8
2.1 Abstract .....	8
2.2 Introduction.....	8
2.3 Theoretical model .....	10
2.4 Acoustic radiation force .....	15
2.5 Parametric analyses and numerical simulations .....	18
2.5 Results and discussion .....	20
2.5.1 Influence of cell components on ARF.....	21
2.5.2 Influence of cell geometry on ARF.....	22
2.5.3 Influence of acoustic parameters on ARF .....	24
2.5.4 Influence of the Gaussian beam waist size.....	27
2.5.5 Influence of cell size on ARF.....	28
2.5.6 Influence of the cell shape on ARF .....	29
2.6 Conclusions.....	31
Chapter 3: Standing surface acoustic waves, and the mechanics of acoustic tweezer manipulation of eukaryotic cells .....	33
3.1 Abstract .....	33
3.2 Introduction .....	33

3.3 Theoretical model.....	37
3.4 Results .....	40
3.4.1 ARF in the x direction .....	40
3.4.2 ARF in the y direction .....	53
3.5. Conclusion.....	58
Chapter 4: Mechanical memory in ion channel function.....	61
4.1 Abstract .....	61
4.2 Introduction .....	61
4.3 Results .....	62
4.4 Discussion .....	70
4.5 Methods.....	72
Chapter 5: The mechanics of a sound wave impinging upon a long cylinder, and the prospect of acoustic signal transduction by tomato trichomes .....	76
5.1 Abstract .....	76
5.2 Introduction .....	76
5.3 Materials and methods .....	79
5.3.1 Imaging of tomato trichomes .....	79
5.3.2 Mechanical and acoustical properties of trichomes .....	80
5.3.3 Theoretical model.....	82
5.3.4 First-order equations of the acoustic wave field .....	86
5.3.5 Calculation of scattering coefficients .....	87
5.3.6 Calculation of acoustic radiation force.....	89
5.3.7 Normal stresses in a trichome .....	93
5.3.8 Finite element simulations.....	94
5.4 Results and discussion.....	97
5.4.1 Imaging of trichomes.....	97
5.4.2 Validation of the model.....	97
5.4.3 A tomato trichome is both acoustically and mechanically rigid compared to air .....	99
5.4.3 Effects of animal sound emissions on tomato trichomes .....	100
5.5 Conclusions .....	106
Chapter 6: Conclusions and future perspectives.....	107

6.1 Conclusion.....	107
6.2 Perspective .....	108
References.....	111
Appendix A1. Standing surface acoustic waves, and the mechanics of acoustic tweezer manipulation of eukaryotic cells.....	122
Appendix A2. Mechanical memory in ion channel function.....	124
Curriculum Vitae .....	126

# List of Figures

FIG. 2.1 Schematic of a Gaussian beam incident upon a triple-layered shell (three-layer model) model of a eukaryotic cell.....	12
FIG. 2.2 Finite element model: (a) representative mesh for eukaryotic cell; (b) enlarged FE mesh. .....	20
FIG. 2.3 Acoustic radiation force amplification factor $Y_p$ as a function of frequency for the three-layer model with $z_0=0$ . A fictional cell with the acoustic properties of the outer layer changed to match those of the cytoplasm had a response similar to that of the full cell. However, changing the acoustic properties of the nucleus to match those of the cytoplasm attenuated $Y_p$ substantially. Symbols: numerical simulations; curves: theoretical predictions.....	22
FIG. 2.4 Contour plots showing the effects of (a) excitation frequency and nuclear radius, $r_3$ , and (b) excitation frequency and outer layer thickness, $l = r_1 - r_2$ , on the acoustic radiation force amplification factor $Y_p$ for a three-layered model. The beam waist of the Gaussian ultrasound wave was fixed at $W=3\lambda$ . Baseline values: $z_0=0$ , $r_1=50\mu\text{m}$ , $r_2=45\mu\text{m}$ and $r_3=30\mu\text{m}$ .....	24
FIG. 2.5 Contour plots showing the effects on the acoustic radiation force amplification factor of (a) cell membrane density, (b) cytoplasm density and (c) nucleus density. $z_0=0$ , $r_1=50\mu\text{m}$ , $r_2=45\mu\text{m}$ and $r_3=30\mu\text{m}$ . .....	26
FIG. 2.6 Contour plots showing the effects on the acoustic radiation force amplification factor of (a) outer layer velocity of sound, (b) cytoplasmic velocity of sound and (c) nuclear velocity of sound. $z_0=0$ , $r_1=50\mu\text{m}$ , $r_2=45\mu\text{m}$ and $r_3=30\mu\text{m}$ . .....	27
FIG. 2.7 (a) Acoustic radiation force function plotted as a function of frequency for selected values of beam waist (eukaryotic cell immersed in water, with $z_0=0$ , $r_1=50\mu\text{m}$ , $r_2=45\mu\text{m}$ and $r_3=30\mu\text{m}$ ). (b) Angular distribution of the scattered Gaussian ultrasound wave, with frequency fixed at 50 MHz. ....	28
FIG. 2.8 (a) Acoustic radiation force function plotted as a function of frequency for selected values of cell radius (eukaryotic cell immersed in water, with $z_0=0$ , $r_2= 0.9r_1$ , $r_3= 0.6r_1$ , $W=3\lambda$ ). (b) Backscattering amplitude of the scattered Gaussian ultrasound wave, with beam radius fixed at $W=3\lambda$ . ....	29
FIG. 2.9 Acoustic radiation force amplification factor plotted as a function of frequency for spheroids of varying aspect ratio. (a) Schematic of a Gaussian beam incident upon a spheroidal three-layer model. (b) Cross-sectional view of the spheroidal three-layer model. (c) Frequency dependence of the ARF amplification factor of a prolate three-layer model generated by a focused Gaussian wave, for several values of aspect ratio $b/a$ . (d) Frequency dependence of the ARF amplification factor of oblate three-layer models, showing values of ARF an order of magnitude lower than those of the prolate cells in panel.....	30
FIG. 3.1. (a) Schematic of a SSAW incident upon a three-layered model of a eukaryotic cell. (b) The origin of the local spherical coordinate system $r, \theta, \varphi$ resides at the instantaneous center of the eukaryotic cell. ....	37
FIG. 3.2. Representative finite element model for a eukaryotic cell in a fluid medium excited by a piezoelectric device that produces SSAWs.....	43
FIG. 3.3 (a) Dimensionless acoustic radiation force, $Y_{px}$ , versus frequency for an entire cell, a cell lacking a cortical layer, and a cell lacking a nucleus. For the case shown, the cell position parameter is $y_0 = \lambda_s/2$ so that the cell is centered at the pressure antinodes, and the Rayleigh angle is $\theta_R = 20^\circ$ . (b) Dimensionless ARF, $Y_{px}$ , versus frequency for an entire cell with several	

different Rayleigh angles. For the case shown, the position parameter is  $y_0 = \lambda_s/2$  so that the cell is centered at the pressure antinodes. For certain frequency ranges at higher Rayleigh angles, the cell is drawn back towards the substrate. (c) Normalized time-independent scattering potential for both the repulsive and attractive behavior are listed with the frequencies being 10 MHz and 60 MHz, respectively. The Rayleigh angle is  $\theta_R = 60^\circ$ . Symbols: numerical (finite element, FE) simulations; curves: theoretical predictions. .... 45

FIG. 3.4 Contour plots of negative values of the dimensionless ARF,  $Y_{px}$ , for (a) pressure antinodes ( $y_0 = \lambda_s/2$ ) and (b) pressure nodes ( $y_0 = \lambda_s/4$ ). Over the majority of parameter space (gray space),  $Y_{px}$  is positive and the cell is predicted to be pushed away from the substrate. .... 48

FIG. 3.5 (a) Dimensionless ARF  $Y_{px}$  plotted as a function of  $y_0$  for selected Rayleigh angles, with wavelength  $\lambda_s = 100 \mu\text{m}$ . (b) The dimensionless ARF,  $Y_{px}$ , is a strong function of the Rayleigh angle  $\theta_R$  and the wavenumber (and hence wavelength), as is evident from Eqs. (3.15)-(3.16). (c) Dimensionless ARF  $Y_{px}$  plotted as a function of Rayleigh angle  $\theta_R$  for selected  $k_1 y_0$ . Symbols: numerical (finite element, FE) simulations; curves: theoretical predictions. .... 50

FIG. 3.6 (a) Dimensionless ARF  $Y_{px}$  and (b) backscattering amplitude as a function of frequency for selected values of cell radius (eukaryotic cell immersed in water); here, cells are self-similar, with layer sizes scaling with cell size ( $r_2 = 14r_1/15$  and  $r_3 = 6r_1/15$ ,  $\theta_R = 20^\circ$  and  $y_0 = \lambda_s/2$ ). (c) Dimensionless ARF  $Y_{px}$  and (d) backscattering amplitude for identical cells, but now with the nuclear and cortical layer sizes held constant to represent changes in volume associated with the cell cycle. Here, the thickness of the outer layer  $l = r_1 - r_2 = 1 \mu\text{m}$ , the nuclear radius is  $r_3 = 6 \mu\text{m}$ ,  $\theta_R = 20^\circ$  and  $y_0 = \lambda_s/2$ . Symbols: numerical (finite element, FE) simulations; curves: theoretical predictions. .... 52

FIG. 3.7 Dimensionless in-plane ARF versus frequency of an entire cell, a cell lacking a cortical layer, and a cell lacking a nucleus. Position  $y_0 = \lambda_s/8$  and Rayleigh angle  $\theta_R = 80^\circ$ . (b) Dimensionless in-plane ARF,  $Y_{py}$ , versus frequency for an entire cell with several different Rayleigh angles. For the case shown, the position parameter is  $y_0 = \lambda_s/8$ . Symbols: numerical (finite element, FE) simulations; curves: theoretical predictions. .... 55

FIG. 3.8 Conditions for and magnitudes of in-plane, attractive values of the dimensionless ARF  $Y_{py}$  for a cell located at  $y_0 = \lambda_s/8$  for  $1 \leq f \leq 80\text{MHz}$  and  $1^\circ \leq \theta_R \leq 90^\circ$ . .... 56

FIG. 3.9 (a) Dimensionless in-plane ARF  $Y_{py}$  plotted as a function of  $y_0$  for selected Rayleigh angles, with wavelength fixed at  $\lambda_s = 100 \mu\text{m}$ . (b) Dimensionless in-plane ARF  $Y_{py}$  plotted as a function of Rayleigh angle  $\theta_R$  for three different wavelengths, with  $y_0 = \lambda_s/8$ . (c) Dimensionless in-plane ARF  $Y_{py}$  plotted as a function of  $k_1 y_0$ . Symbols: numerical (finite element, FE) simulations; curves: theoretical predictions. .... 57

FIG. 3.10 (a) Dimensionless in-plane ARF  $Y_{py}$  plotted as a function of frequency for selected values of cell radius, with  $r_2 = 14r_1/15$  and  $r_3 = 6r_1/15$ ,  $\theta_R = 80^\circ$ , and  $y_0 = \lambda_s/8$ . (b) Dimensionless in-plane ARF  $Y_{py}$  plotted as a function of a cell circle, but now with the nuclear and cortical layer sizes held constant to represent changes in volume associated with the cell cycle. Here, the thickness of the outer layer  $l = r_1 - r_2 = 1 \mu\text{m}$ , the nuclear radius is  $r_3 = 6 \mu\text{m}$ ,  $\theta_R = 80^\circ$  and  $y_0 = \lambda_s/8$ . Symbols: numerical (finite element, FE) simulations; curves: theoretical predictions. .... 58

FIG. 4.1 Functional expression of TRAAK channels in *Xenopus* oocytes. (a) Experimental set-up. A *Xenopus* oocyte expressing TRAAK channel is placed in the focus of the ultrasound field. The membrane current was recorded by using the two-electrode voltage clamp. (b) Effects of



ultrasound on TRAAK channels. The membrane voltage was held at -80 mV before stepping to 40 mV (time 3 s). After 10 s, the membrane voltage returned to -80 mV. The black line shows the current without ultrasound activation. To test the effects of ultrasound, we turned on the ultrasound at time 3 s and lasted for 1 s. The sound pressure was increased gradually from 0.04 MPa to 0.254 MPa. 5 s period was held before next sequence. (c) The comparison between the membrane current before the ultrasound sound activation and the current at the end of the activation. (d) After the ultrasound activation, we turned off the ultrasound and ran more sequences. The current would decrease gradually. (e) Periodic loading. Membrane current showed cumulative, creep-like increase. (f) The comparison between the membrane current for baseline and the peak value of each ultrasound activation..... 64

FIG. 4.2 (a) ‘Direct Deformation Estimation’ algorithm (DDE) was used to calculate the first principal strain  $t=0$  s, and  $t=0.5$  s. Averaged first principal strain versus time. The image before the moment we turned on the ultrasound was used as the reference image for the following warping to get the estimated deformation gradient. After that, a direct calculation of averaged first principal strain could be obtained for a (b) 1-second ultrasound activation and (c) comparison between the peak value and the strain before the ultrasound. (d) Periodic loading for the strain change. (e) The corresponding peak strains for each ultrasound activation. The color from dark to light means the sound pressure increase gradually. Simulated spatial profiles of cell mechanics. (f) Displacement and (g) First principal strain change for the oocyte under the activation of ultrasound. Averaged first principal strain versus time by FEM in COMSOL. (h) 1-second activation, (i) comparison between the peak average strain and the baseline value. (j) and (k) are the corresponding results to show the periodic loading. The color from dark to light means the sound pressure increase gradually..... 66

FIG. 4.3 The membrane current change is plotted versus time and fitted curve with Eq. (4.3). .. 70

FIG. 5.1 (a) Trichomes on the stem of *S. lyopersicum*, showing non-glandular trichomes. (b) Much shorter glandular trichomes (e.g., as denoted by the arrow) were not considered in the analysis.80

FIG. 5.2. Side view (a) and top view (b) of schematic of a circular and infinitely long rigid cylinder, which is immersed in viscous fluid and impinged by plane travelling waves. .... 92

FIG. 5.3. Finite element model for validating acoustic radiation force on a rigid cylinder in viscous fluid. Perfect matched layer is marked as PML. .... 95

FIG. 5.4. Convergence of the infinite series. Progressively higher order terms improved the estimation of acoustic radiation force for a rigid cylinder in plane travelling wave for  $\delta/R = 0.1$ ,  $\mu' = 0$  and  $\rho' = 1000$ . Beyond  $n = 2$ , the increase in accuracy associated with including additional terms was negligible. However, to ensure convergence in all simulations,  $n = 20$  terms were used. .... 98

FIG. 5.5. (a) Comparison of theoretical model predictions and numerical simulations for the acoustic radiation force function  $Y_{tr}$  (Eq. 5.42) on a rigid cylinder for a plane travelling wave. Shown are results for  $\rho' = 1000$  and  $\mu' = 0$ . (b) Effect of bulk viscosity on acoustic radiation force in a plane travelling wave for  $\delta/R = 0.1$  and  $\rho' = 1000$ . .... 99

FIG. 5.6. Effect of density ratio on the acoustic radiation force on an acoustically rigid cylinder subjected to a plane travelling wave for  $\delta/R = 0.1$  and  $\mu' = 0$ . .... 101

Fig. 5.7. Estimates of the membrane tension,  $T$ , that would arise in the membrane of a tomato trichome in response to acoustic excitation from a range of species that emit different combinations of frequency and pressure..... 102

FIG. A2.1 A generalized Kelvin viscoelastic model ( $n$  Voigt elements in serial)..... 124

FIG. A2.2 A representative fitting for the averaged first principal strain by generalized Kelvin model. Three time constants  $\tau_1 = 0.18 s$ ,  $\tau_2 = 1.38 s$ ,  $\tau_3 = 21 s$  can be enough to obtain a great fitting..... 125

FIG. A2.3 (a) and (b) are the three branches' contribution on the first principal strain..... 125

# **List of Tables**

Table 2.1. Acoustic parameters .....	19
Table 3.1. Acoustic parameters .....	42
Table 5.1 Mechanical properties ranges studied for model trichomes.....	81
Table 5.2 Acoustic properties of air .....	82
Table 5.3. Range of sound frequency and sound pressure for different species .....	104
Table A2.1. Values of material properties used in finite element simulations.....	124

# **Acknowledgments**

I am so lucky to be admitted for the dual-degree program and to have had the chance to study at Washington University. Besides the happiness, I would like to express my sincere gratitude to my supervisor, Prof. Guy Genin. He paved the way for me to the exciting scientific research. During the last two years in his lab, he always guided me patiently, supported me and encouraged me to use my background of solid mechanics to solve mechanobiology problems. His motivation and commitment always inspire me to be confident with my research and believe my work is meaningful. I still remember he suggested that I submit my paper to Journal of Mechanics and Physics of Solids, which is the number one journal for mechanics, and remember when it was finally accepted. It was unreal for me and brought me much confidence in the following days. After that, I got my IJSS paper accepted. We then focused on much more challenging work and got many progresses. During the last two years, he is not only my supervisor, but also my good friend who really cares about me, always brings me a lot of happiness. He has amazing social talent and always can find suitable collaborator for me to solve the troublesome problem.

I would also like to express my sincere gratitude to my second mentor, Prof. Elliot Elson. Besides my research about my thesis, I also learnt mechanobiology with Elliot. He is knowledgeable and always bright us with intrinsic ideas. I enjoy the lunch meeting every week with him and am happy to obtain constructive suggestions to my project. I would also like to thank my committee members, including Prof. Hong Chen, Prof. Jianmin Cui, Prof. Mark Meacham, and Prof. Jinyu Shao for the resources they provided, the helpful discussion, and their valuable time to review the dissertation and their insightful comments.

I would also like to thank all the members of Genin lab, Dr. Ethan Hoppe, Dr. Delaram Shakiba, Mr. Shumeng Jiang, Dr. Roger Rowe, Dr. Tony Pryse, Mr. Ms. Ghiska Ramahdita, Mr. Yuan Hong, and Mr. Chengqing Qu, as well as the frequent visitors, Profs. Farid Alisafaei and Silviya Zustiak, and the late Prof. Barbara Pickard. I thank them for all the help and their inspirations to me. Especially, I would like to show my great appreciation to Ethan, he helped me with my experiments from the very beginning. He is talented at experimentation and always has excellent suggestions for me when I meet any trouble. Besides that, he also helped me with coding and calculation. We spend a lot of time to brainstorm interesting scientific problems. I also want to thank Tony, who is always ready to help anyone in the lab. He taught me how to use the confocal microscope and the high speed camera, showed me his new invention: RCS. I really enjoy the happiness we share both in the lab and outside the lab.

I would like to thank my collaborators, like Mr. Yaoheng Yang, Dr. Lu Zhao, Mr. Mingyang Cui, Ms. Sorina Munteanu, Mr. Wenbin Wang, Mr. Liang Shen. Without your help, I cannot get a setup so fast to conduct the experiment. Also, Wenbin gave me a lot of help with programming. Without him, it might take me a much longer time to analyze the experiment results quantitatively.

I would like to thank my roommate, Dr. Zhi Wang, who helped me a lot outside the lab. He has solid understanding of the physics and always brainstorming scientific problem with me. He is a great support on my back when I met trouble. Good at cooking, he always shares his tasty food with me. I would also thank my lifetime friend and also lab member in China, Dr. Wei He, Dr. Chenlei Yu, who helped me a lot for the paperwork in Xi'an. I would also like to thank my lifetime friends, Zhen Chen, Juan Feng, Feng Bie, Liyuan Bai for they didn't be angry for my not attending their wedding. My other lifetime friends, Weibing Wang, Tingju Yuan, Chengxin Ou,

Lei Chen, Hexu Lu, Yue Li, Chen Liang, Shuang Nie, Wei Ding, Ningning Li, Kaixuan Liang.  
You guys care me and also give me support and encourage me. Special thanks to my girlfriend,  
for her understanding my being oversea for such a long time.

I want to thank my family members. My two elder sisters helped me to take care of my parents. I  
know they are always my backbone, supporting me to pursue the dream. Whatever decision I  
made, they just support and encourage me to pursue the happiness. Their unconditional love and  
encouragement always equipped me the power to keep moving without fear.

Xiangjun Peng

*Washington University in St. Louis*

*December 2021*

Dedicated to my parents.

## ABSTRACT OF THE DISSERTATION

Acoustic Radiation Force and its Application for Cell Manipulation and Ion Channels Activation

by

Xiangjun Peng

Doctor of Philosophy in Department of Biomedical Engineering

Washington University in St. Louis, 2021

Professor Guy Genin, Chair

Sound is a stress wave that carries energy and momentum flux. Scattered sound waves can generate acoustic radiation force that can be used to manipulate particles or cells. This dissertation demonstrates the physics behind cell manipulation by ultrasound. The work begins with a detailed analysis of the mechanics of using standing surface acoustic waves to fabricate acoustic tweezers for contactless particle manipulation using acoustic radiation force. Models to design and analyze acoustic radiation force have traditionally relied on plane wave theories that cannot predict how standing surface acoustic waves can levitate cells in the direction perpendicular to the substrate. We therefore developed a revised model for how standing surface acoustic waves lead to acoustic radiation force in three dimensions. The dissertation then explored use of ultrasound for manipulating mechanosensitive ion channels in both plant and animal cells. Although evidence that such manipulation can occur is strong, it is still unclear how ultrasound activates the mechanosensitive ion channels. The dissertation therefore developed mathematical models of these forces, of how they deform the cell membrane, and of how these membrane deformations activate mechanosensitive ion channels. The modeling approach was verified in an idealized system involving measuring ion channel currents in frog oocytes that



were transfected with mechanosensitive ion channels and irradiated using ultrasound. The model predicted these currents, and a modified version of the approach was then used to predict the sensitivity of stress activated ion channels in tomato trichomes to the acoustic radiation force arising from acoustic emissions by insect and other animals. The integrated modeling approach shows promise for design and analysis of experiments and tools that probe and harness the function of stress activated ion channels via ultrasound.

# Chapter 1: Introduction

## 1.1 Harnessing defined acoustic radiation force: a frontier in mechanobiology

New technology often enables new scientific discoveries. The invention of the microscope enabled the visualization of cells and paved the way for cell theory. The invention of fluorescence correlation spectroscopy (FCS) <sup>1</sup> and fluorescence photobleaching recovery (FPR/FRAP) <sup>2</sup> paved the way to understanding diffusion and heterogeneity on cell membranes. The invention of the cell pocker and later the atomic force microscope paved the way to understanding cell membrane mechanics <sup>3</sup>. In each case, the application of these new technologies has formed a key step in the quantitative understanding of cell mechanobiology. This dissertation explores the application of a technology that seems poised to enable another round of advances in mechanobiology: quantitative control of cell electrophysiology through the application of pressure to cells via structured ultrasound.

In recent years, the ability to manipulate single cells and biomolecules have promoted the development of biophysics <sup>4</sup>, mechanobiology <sup>5</sup>, microbiology <sup>6</sup>, and bioanalytical chemistry <sup>7</sup>. The pioneering work of Arthur Ashkin and co-workers resulted in the invention of optical tweezers, which were quickly adopted as an invaluable tool in physics, biology, and chemistry. Such novel tweezers have been used to trap the bacteria, viruses, and cells <sup>8</sup>. The driving force for optical tweezers is known as optical radiation force, which consists of two components: the gradient force and the scattering force. Usually, to generate enough radiation force, high intensity laser is needed. This may heat up the surrounding medium and cause some irreversible damages to biological samples. As a result, to improve the accessibility of contact-free

particle-manipulation technology, many other alternatives to optical tweezers have been developed.

Different from the optical tweezers, which is based on the optical radiation force, the additional technologies depend on different mechanisms, such as magnetic force, optoelectronic, plasmonic, electrokinetic, and hydrodynamic forces <sup>9</sup>. Magnetic tweezers can provide very high degree of spatial resolution just as optical tweezers do. However, they cannot handle particles or structures smaller than 100 nm. To deal with nanosized particles or structures, the plasmonic tweezers were invented, which make use of locally enhanced electromagnetic fields on the tiny samples. Even though the plasmonic tweezers need lower laser power, the localized laser intensities can trap particles but also heat the sample. To avoid the sample heating and locally convective flows, researchers invented the electrokinetic tweezers, which relies on the electrophoretic and dielectrophoretic forces. The trapped samples could be nanometers to millimeters. Unfortunately, they rely on particle or cell polarizability and usually need low-conductivity media, which could affect cell physiology.

As the dynamic counterpart of electrokinetic tweezers, the optoelectronic tweezers do not need the electrodes. Instead, they use a light source and photoconductive substrate to generate dielectrophoresis. However, they also need to use low-conductivity media and cannot widely used for many biological studies. By controlling the fluid flow to manipulate the particles, the hydrodynamic tweezers may be the simplest approach for micromanipulation. It will not cause heating problems, but the precision is low and the ability to control nanoparticles is limited.

Acoustic tweezers can serve as an alternative since they can address many of the limitations of different technologies mentioned above. It's easy to tune the sound frequency from kilohertz to

megahertz, thus, the acoustic tweezers can directly manipulate particles range from hundreds of nanometers to tens of millimeters. Both the acoustic frequency and power used in acoustic tweezers are similar to those used in ultrasound imaging and clinical applications<sup>10</sup>. This dissertation therefore explores the quantitative application of acoustic radiation force, arising from ultrasound, to mechanobiology and electrophysiology.

## **1.2 Acoustic radiation force**

The key factor for the acoustic tweezers is the acoustic radiation force, analogous to optical radiation force. Sound carries momentum and can thus exert forces on matter. In 1902, Lord Rayleigh first pointed out the existence of the acoustic radiation force<sup>11</sup>. After his pioneering work, many researchers made tremendous contributions on the physics behind the acoustic radiation force. It is worth noting that in 1934, King derived the closed form solution for the acoustic radiation force on rigid sphere in inviscid fluid<sup>12</sup>. Such theory was then extended elastic speres, droplets, and gas bubbles by accounting for the compressibility of the spere particles<sup>13</sup>. The theoretical study was finally validated by experiment with no restrictions placed on the size of the sphere<sup>14</sup>.

Those early work only considered the plane wave. Traveling plane waves can only exert force that push the particles, which cannot trap the particles. With the development of fabrication, people now can create different kind of transducers to improve the flexibility of acoustic manipulation, including focused Gaussian beams, Bessel beams, standing surface acoustic waves<sup>5</sup>. The wave forms may be different, but the mechanism for acoustic manipulation is the same, with all due to the acoustic radiation force. These kinds of waves can generate stable trap for particles in the potential well or the pressure nodes, bringing us opportunities to conduct fancy

research ranges from biology, physics, and chemistry. In 1991, Junru Wu and co-workers first used two opposing traveling ultrasounds to generate standing wave and trapped the oocyte <sup>15</sup>. This new technology was first named as acoustic tweezers. Besides the bulk wave, the surface acoustic wave was also used to fabricate the acoustic tweezers because the apparatus is tiny and easily incorporated within microfluidics. Although many groups use these ultrasound setups based acoustic tweezers to manipulate cells, the basic mechanisms are still largely unknown. This dissertation therefore develops a mathematical foundation for improving this understanding.

### **1.3 Ultrasound manipulation on ion channels**

Neuron stimulation techniques are vital tools for the treatment of neurological disorders including depression <sup>16</sup>, Parkinson's disease <sup>17</sup>. Ion channels can serve as the molecular switches for manipulating the activity of specific cells within neuronal circuits. External means have been used to activate the ion channels embedded in neurons, such as electrical activation <sup>18</sup>, magnetic field activation <sup>19</sup>, and optical evaluation <sup>20</sup>. These methods are either invasive or unable to focus at specific cortical areas. Ultrasound offers an alternative owing to its unique advantages as it can noninvasively carry energy flux through the skull to the deep brain <sup>21</sup>. This new approach has been termed sonogenetics, and aims to use focused ultrasound to manipulate mechanosensitive ion channels and thereby change downstream signaling pathways.

Ultrasound modulation of electrical activity in excitable tissues dates back to 1929 with the discovery that high frequency ultrasound might affect heart muscles <sup>22</sup>. Following this was the discovery that ultrasound could also tune activity of the central nervous system <sup>23</sup> and of neural structures <sup>24</sup>. More recently, the potential application for “sonogenetic” ultrasound manipulation of excitable tissue has been studied broadly *ex vivo* <sup>25-27</sup> and *in vivo* <sup>28,29</sup>. With numerous

potential applications, such technology motivates studies in this dissertation on the mechanisms of ultrasound manipulation of cell membrane currents.

What is the molecular basis? Some groups focus on the mechanosensitive ion channels tuned by ultrasound. These are K2P channels (TREK-1, TREK-2, TRAAK)<sup>28,30</sup>, the Piezo 1 channel<sup>26</sup>, MscL channels<sup>25</sup>. Despite much research effort in this area, the molecular basis for such manipulation is still unclear. Like the cavitation effect, ultrasound could be amplified by microbubbles to evoke behavioral responses in *C. elegans* with TRP-4 channels<sup>31</sup>. Meanwhile, ultrasound could also cause thermal effects sufficient to activate thermosensitive ion channels like the TRPV1 channel<sup>32</sup>. By expressing TRPV1 channels in the deep brain of mouse and applying ultrasound heating, a degree of neural motor control via ultrasound has been demonstrated<sup>32</sup>.

The coupled acoustic and fluid flow fields are likely factors, and separating them is a challenge. The nonlinearity of ultrasound could lead to mechanical effect likes including acoustic streaming and acoustic radiation force. With very high frequency (e.g., 43 MHz), ultrasound beams can be focused to narrow regions, just tens of microns. High pressure gradients and energy absorption contribute to local acoustic streaming. Due to fluid viscosity, microstreaming flow can expand away from cells, but also decay relatively fast, in a way that is sensitive to boundary conditions. At the center, high speed fluid flow can lead to elevated shear stress on the cell membrane and activate the Piezo 1 channel<sup>26</sup>. Standing surface acoustic waves can activate MscL and its mutation, I92L, but although these neuronal responses are definitively induced by ultrasound, the effects of fluid flow known as acoustic streaming cannot be ruled out<sup>25</sup>. However, a radiation force model, in the absence of acoustic streaming, can explain retinal ultrasound neurostimulation<sup>33</sup>. Thus, debate continues about how the ion channels sense ultrasound.

Although multiple pathways are likely possible, this dissertation shows for the first time that strain in the cell membrane can explain ultrasound modulation of mechanosensitive ion channels, and makes the first quantitative link between ultrasound-related electrophysiology and mechanobiology<sup>34</sup>.

## 1.4 Plant responses to sound

The evolutionary battle between plants and their insect herbivores has led to a diverse array of sensing abilities in both (e.g.,<sup>35-38</sup>). For a broad range of plants, hair cells known as trichomes are a key mediator of sensing ability, providing a sensation of touch<sup>39-43</sup>. The leaves of *Arabidopsis thaliana* can meaningfully respond to the noise of *Pieris rapae* caterpillars feeding on them<sup>44,45</sup>, possibly due to hearing by trichomes<sup>45</sup>. Although 1950s claims of plants appreciating music were falsified by the 1960s<sup>46</sup>, evidence that plants can transduce sound exists in the form of transcriptomic, proteomic, and hormonal changes<sup>47-52</sup>. Although there is no consensus on how sound signals are transduced<sup>53</sup>, mechanisms that have been identified for mechanosensation include stretch-activated ion channels and plasmodesmata-based interactions between the cytoskeleton, plasma membrane, and cell wall<sup>54</sup>. Trichomes can in this way work as an active mechanosensory switch, with mechanical stimulus eliciting Ca<sup>2+</sup> oscillations of the trichome and pH shifts in surrounding cells. We therefore explored the possibility that trichomes might also serve as mediators that can convert the acoustic radiation force of an insect into strain sufficient to open stretch-activated ion channels.

Acoustic radiation force from sound is typically too small to be felt, but nevertheless can be used to manipulate small particles, droplets, cells, and organisms<sup>55-57</sup>. Specifically, when subjected to a sound field, particles experience a net force, typically interpreted as time-averaged pressure.

Our focus was computing this force on long, cylindrical bodies, representative of trichomes such as those of tomato plants.

Although the acoustic radiation force on a cylinder in an inviscid medium is known <sup>58</sup>, the distribution of acoustic radiation force on a cylinder in a viscous medium has never before been derived to our knowledge. This dissertation therefore presents the first derivation of the acoustic radiation force on a long cylinder in a viscous medium and applies it to the problem of a trichome vibrating in response to acoustic stimulus.

## **1.5 Overview of dissertation**

Chapters 2 and 3 lay out a framework for predicting acoustic radiation force on living cells, both numerically and analytically. Chapter 4 then applies these to design and interpret experiments that, for the first time, definitively demonstrate membrane-strain-induced opening of ion channels via ultrasound. The chapter also presents an integrated model of ultrasound excitation, membrane viscoelasticity, and membrane electrophysiology. Chapter 5 applies these techniques to a plant cell, tomato trichomes, and assesses the range over which acoustic signals might be transduced in these cells via the opening of membrane mechanosensitive ion channels. Finally, Chapter 6 draws some conclusions and outlines critical future directions for this work.



# Chapter 2: The acoustic radiation force of a focused ultrasound beam on a suspended eukaryotic cell

## 2.1 Abstract

Although ultrasound tools for manipulating and permeabilizing suspended cells have been available for nearly a century, accurate prediction of the distribution of acoustic radiation force (ARF) continues to be a challenge. We therefore developed an analytical model of the acoustic radiation force (ARF) generated by a focused Gaussian ultrasound beam incident on a eukaryotic cell immersed in an ideal fluid. The model had three layers corresponding to the nucleus, cytoplasm, and membrane, of a eukaryotic cell. We derived an exact expression for the ARF in relation to the geometrical and acoustic parameters of the model cell components. The mechanics of the cell membrane and nucleus, the relative width of the Gaussian beam, the size, position and aspect ratio of the cell had significant influence on the ARF. The model provides a theoretical basis for improved acoustic control of cell trapping, cell sorting, cell assembly, and drug delivery.

## 2.2 Introduction

Ultrasound has been applied to manipulate<sup>59</sup> and lyse<sup>60</sup> cells since the 1920s. These were amongst the first contactless particle trapping and manipulation methods in biology and continue to find application in bio-medical research<sup>61,62</sup>. A particularly sensitive application of ultrasound manipulation is acoustic tweezers, which has received particular attention due to its advantages

in contamination-free and label-free cell handling <sup>15,63-65</sup>. Numerous experimental, theoretical and numerical studies have demonstrated that acoustic tweezers can be used to align, move and sort microparticles and cells <sup>61,64,66-68</sup>. Higher energy versions of these focused ultrasound technologies can be used to permeabilize membranes to ions and drugs <sup>69-73</sup>.

Underlying all of these applications is fine control of acoustic radiation force (ARF). The study of ARF, which is the period-averaged force caused by a sound wave, is just like the optical radiation force generated by electromagnetic waves striking on electrically or magnetically responsive objects <sup>74</sup>, therefore has a long history <sup>75</sup>. Investigation of ARF on microparticles dates back to King's theoretical study of ARF on a rigid sphere in an ideal fluid subjected a planar progressive sound field <sup>76</sup>. Yosioka and Hasegawa extended King's work to compressible spherical particles <sup>14</sup>, and extensive subsequent theoretical and experimental works have shown the ARF exerted by a planar acoustic field on a microsphere <sup>77-79</sup> to be very sensitive to the structure and acoustic properties of the micro-particle.

Two theoretical approaches are commonly used to calculate the ARF: the partial-wave expansion method and the ray acoustics method. The ray acoustics method is limited to cases when the wavelength of the acoustic wave is far smaller than the radius of the sphere, but the partial-wave expansion method is applicable to an arbitrary frequency range <sup>80</sup>. The partial-wave expansion method has been used to explore a range of waves in spherical coordinates, including plane waves <sup>14</sup>, Bessel waves <sup>81</sup> and Gaussian waves <sup>82</sup>.

Gaussian waves are widely used to model optical and acoustical wavefields converging to or diverging from focal regions <sup>82</sup>. Particles can become trapped by a Gaussian wave in the focal

region<sup>6</sup>. Focused Gaussian ultrasound waves have found utility in bioscience because they can trap suspended cells for quantification of the cell's mechanical properties<sup>83</sup>.

In existing theoretical studies of ARF in cell manipulation, cells were modeled as homogeneous microspheres<sup>84</sup>. However, eukaryotic cells are heterogeneous, and the nucleus has been reported to affect wave propagation significantly. Thus, the simple homogeneous sphere model does not accurately represent eukaryotic cells.

As a first step towards understanding how cell shape and heterogeneity affect ARF, we studied an ellipsoidal cell consisting of a membrane, cytoplasm, and nucleus. This three-layered model was embedded in an ideal fluid that was subjected to a focused Gaussian ultrasound wave. The partial wave expansion method was employed to calculate the ARF on the cell. Results show that the nucleus and membrane play an important role in determining the ARF, along with the aspect ratio of the cell and the size of the cell relative to the Gaussian beam waist.

## 2.3 Theoretical model

With reference to Fig. 2.1, a focused Gaussian ultrasound wave is incident on a eukaryotic cell immersed in an inviscid fluid, with  $z_0$  being the location of the center of the cell relative to the origin of the Cartesian coordination system, which is also the beam waist center. The wave with beam waist radius  $W$  propagates along the  $+z$  direction. The eukaryotic cell consists of an outer cell membrane with radius  $r_1$ , a middle layer (cytoplasm) with radius  $r_2$ , and an inner core (cell nucleus) with radius  $r_3$ . Let the mass densities and acoustic velocities of the surrounding medium, the cell membrane, the cytoplasm and the nucleus be denoted by  $(\rho_1, c_1)$ ,  $(\rho_2, c_2)$ ,  $(\rho_3, c_3)$

and  $(\rho_4, c_4)$ , respectively. Corresponding acoustic impedances and wave numbers are

$Z_i = \rho_i c_i$  ( $i = 1, 2, 3, 4$ ) and  $k_i = \omega / c_i$  ( $i = 1, 2, 3, 4$ ),  $\omega$  being the circular frequency of the Gaussian wave.

In a progressive focused Gaussian ultrasound wave field, the incident wave pressure is expressed by:

$$p_i(x, y, z, t) = \frac{p_0 W}{w(z)} \exp\left[-\frac{(x^2 + y^2)}{w^2(z)}\right] \exp\left\{-i\left\{k\left[\frac{(x^2 + y^2)}{2R(z)} + z\right] - \tan^{-1}\left(\frac{z}{f_c}\right)\right\}\right\} \exp(-i\omega t) \quad (2.1)$$

where  $w(z) = W\sqrt{1 + (z/f_c)^2}$  is the beam width,  $R(z) = f_c(z/f_c + f_c/z)$  is the radius of curvature of the isophase surface,  $\tan^{-1}(z/f_c)$  is the phase factor, and  $f_c = kW^2/2$  is the confocal factor.

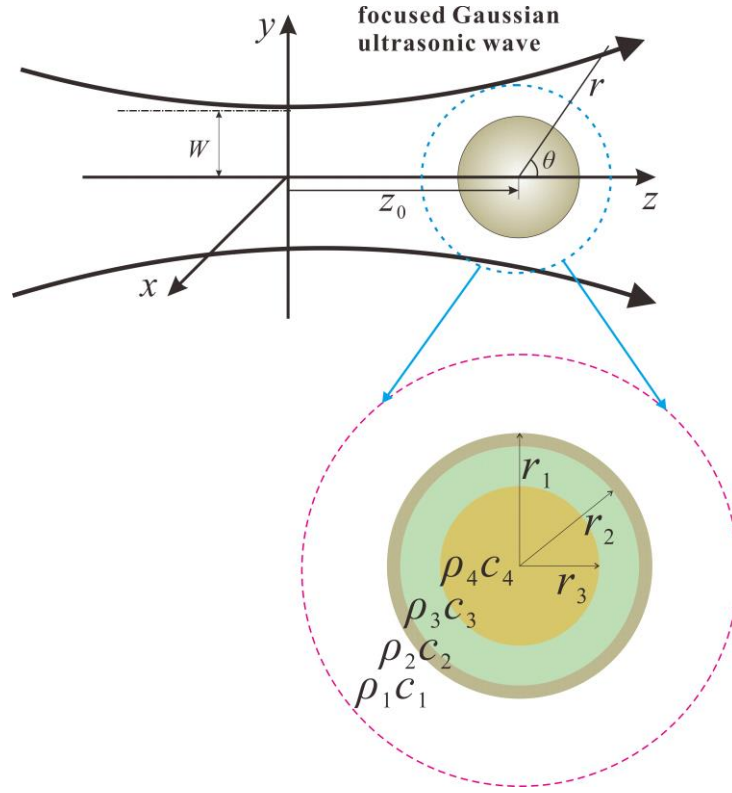


FIG. 2.1 Schematic of a Gaussian beam incident upon a triple-layered shell (three-layer model) model of a eukaryotic cell.

Although the phase front of the fundamental mode of the incident Gaussian wave is not planar in general, it is very nearly planar in the neighborhood of the beam waist and can be approximated as an acoustic wave with Gaussian amplitude distribution<sup>85</sup>:

$$p_i(x, y, z, t) \gg p_0 \exp\left(-\frac{x^2 + y^2}{W^2}\right) \exp(ik_1 z) \exp(-i\omega t) \quad (2.2)$$

We define the wavelength in a particular medium as  $l = 2\rho/k_1 = 2\rho c_1/\omega$  and  $s = 1/(kW)$ . In a spherical coordinate system, with  $x = r \sin \theta \cos \varphi$ ,  $y = r \sin \theta \sin \varphi$ ,  $z = r \cos \theta$ , the incident acoustic wave pressure may be expanded into a generalized Rayleigh wave series, as:

$$p_i(r, q, t) = p_0 \sum_{n=0}^{\infty} L_n i^n (2n+1) j_n(k_1 r_1) P_n(\cos q) \exp(-i\omega t) \quad (2.3)$$

where:

$$\Lambda_{2p} = \frac{\Gamma(p+1)}{\Gamma(p+1/2)} \sum_{j=0}^p \frac{\Gamma(p+j+1/2)}{(p-j)! j!} Q_0 (-4Q_0 s^2)^j \exp(-i\alpha_1 z_0) \quad (2.4)$$

$$\Lambda_{2p+1} = \frac{\Gamma(p+1)}{\Gamma(p+3/2)} \sum_{j=0}^p \frac{\Gamma(p+j+3/2)}{(p-j)! j!} (Q_0 - Q_1 - jQ_1) (-4Q_0 s^2)^j \exp(-i\alpha_1 z_0) \quad (2.5)$$

Here,  $Q_0 = 1/(1+2iz_0/l)$ ,  $Q_1 = 2/[\alpha_1 l(i-2z_0/l)^2]$ ,  $l = \alpha_1 W^2$ ,  $j_n(\cdot)$  is the spherical Bessel function of the first kind,  $P_n(\cdot)$  is the Legendre polynomial of order  $n$ , and  $\Gamma(\cdot)$  is the Gamma function.

The scattered wave field can be expressed as:

$$p_s(r, q, t) = p_0 \sum_{n=0}^{\infty} L_n i^n (2n+1) A_n h_n^{(1)}(k_1 r_1) P_n(\cos q) \exp(-i\omega t) \quad (2.6)$$

in which  $A_n$  is the scattering coefficient to be determined by the boundary condition. Therefore,

the total wave field outside the three-layer model (eukaryotic cell) takes the form:

$$p_1(r_1, q, t) = p_0 \sum_{n=0}^{\infty} L_n i^n (2n+1) \left[ j_n(k_1 r_1) + A_n h_n^{(1)}(k_1 r_1) \right] P_n(\cos q) \exp(-i\omega t) \quad (2.7)$$

The acoustic wave field in the cell membrane  $p_2$ , in the cytoplasm  $p_3$ , and in the nucleus  $p_4$

can be expressed as:

$$p_2(r_2, q, t) = p_0 \sum_{n=0}^{\infty} \mathcal{L}_n i^n (2n+1) \left[ B_n j_n(k_2 r_2) + C_n y_n(k_2 r_2) \right] P_n(\cos q) \exp(-i\omega t) \quad (2.8)$$

$$p_3(r_3, q, t) = p_0 \sum_{n=0}^{\infty} \mathcal{L}_n i^n (2n+1) \left[ D_n j_n(k_3 r_3) + E_n y_n(k_3 r_3) \right] P_n(\cos q) \exp(-i\omega t) \quad (2.9)$$

$$p_4(r_4, q, t) = p_0 \sum_{n=0}^{\infty} \mathcal{L}_n i^n (2n+1) \left[ F_n j_n(k_2 r_2) \right] P_n(\cos q) \exp(-i\omega t) \quad (2.10)$$

where  $y_n(\cdot)$  is the spherical Bessel function of the second kind.

To determine the unknown coefficients  $B_n$ ,  $C_n$ ,  $D_n$ ,  $E_n$  and  $F_n$ , we followed previous researchers in approximating the three layers as having shear resistance that is small compared to their resistance to dilatation<sup>86,87</sup>. Therefore, at their interfaces, the boundary condition was that the velocity and pressure must be continuous, leading to the following form for  $A_n$ :

$$A_n = - \frac{\rho_2 c_2 j_n'(k_1 r_1) \left[ \mathcal{Q}_2 j_n(k_1 r_2) - y_n(k_1 r_2) \right] - \rho_1 c_1 j_n(k_1 r_1) \left[ \mathcal{Q}_2 j_n'(k_1 r_2) - y_n'(k_1 r_2) \right]}{\rho_2 c_2 h_n^{(1)'}(k_1 r_1) \left[ \mathcal{Q}_2 j_n(k_1 r_2) - y_n(k_1 r_2) \right] - \rho_1 c_1 h_n^{(1)}(k_1 r_1) \left[ \mathcal{Q}_2 j_n'(k_1 r_2) - y_n'(k_1 r_2) \right]} \quad (2.11)$$

where

$$\begin{aligned} \mathcal{Q}_1 &= \frac{\rho_4 c_4 y_n'(k_3 r_4) j_n(k_4 r_4) - \rho_3 c_3 y_n(k_3 r_4) j_n'(k_4 r_4)}{\rho_4 c_4 j_n'(k_3 r_4) j_n(k_4 r_4) - \rho_3 c_3 j_n(k_3 r_4) j_n'(k_4 r_4)} \\ \mathcal{Q}_2 &= \frac{\rho_3 c_3 \left[ \mathcal{Q}_1 j_n(k_3 r_3) - y_n(k_3 r_3) \right] y_n'(k_2 r_3) - \rho_2 c_2 \left[ \mathcal{Q}_1 j_n'(k_3 r_3) - y_n'(k_3 r_3) \right] y_n(k_2 r_3)}{\rho_3 c_3 \left[ \mathcal{Q}_1 j_n(k_3 r_3) - y_n(k_3 r_3) \right] j_n'(k_2 r_3) - \rho_2 c_2 \left[ \mathcal{Q}_1 j_n'(k_3 r_3) - y_n'(k_3 r_3) \right] j_n(k_2 r_3)} \end{aligned} \quad (2.12)$$

## 2.4 Acoustic radiation force

For a continuous focused Gaussian ultrasound wave, the ARF is obtained by integrating the excess of pressure  $(p(r, q, t) - p_0)$  generated by the sound field over the instantaneous surface  $S(t)$  of the sphere, as:

$$\mathbf{F}(t) = - \dot{\int}_{S(t)} (p(r, q, t) - p_0) \mathbf{n} dS \quad (2.13)$$

where  $\mathbf{n}$  is the outward normal to  $S(t)$ . To evaluate the ARF, the excess of pressure should be taken up to second-order terms in the velocity potential. For a periodic wave, the ARF is defined as a time-averaged quantity over period of the sound field. The time-averaged force acting on a sphere immersed in an infinite ideal fluid is:

$$\begin{aligned} \langle \mathbf{F} \rangle &= - \int \int_{S(t)} \langle (p - p_0) \rangle \mathbf{n} dS \\ &= - \left\langle \int \int_{S_0} \rho \langle (v_n \mathbf{n} + v_t \mathbf{t}) v_n \rangle \mathbf{n} dS \right\rangle + \int \int_{S_0} \left[ \frac{1}{2} \frac{\rho}{c^2} \left\langle \left( \frac{\partial \psi}{\partial t} \right)^2 \right\rangle - \frac{1}{2} \rho \langle |\nabla \psi|^2 \rangle \right] \mathbf{n} dS \end{aligned} \quad (2.14)$$

where  $\langle \cdot \rangle$  represents the time average,  $\mathbf{t}$  is an in-plane unit tangential vector of  $S(t)$ ,  $S_0$  is the surface of the target at its equilibrium position,  $dS = r dr d\theta$ , and the parameters

$v_n|_{r=r_1} = -\frac{\partial \psi}{\partial r}$  and  $v_t|_{r=r_1} = -\frac{1}{r} \frac{\partial \psi}{\partial q}$  are the radial and tangential components of the velocity at the

surface, respectively. Here,  $\psi = \text{Re}[\phi]$ , for which  $\phi$  is the velocity potential expressed as:

$$\phi = \frac{P_1}{-i\omega\rho} = \frac{P_0}{-i\omega\rho_1} \sum_{n=0}^{\infty} \Lambda_n i^n (2n+1) \left[ j_n(k_1 r_1) + A_n h_n^{(1)}(k_1 r_1) \right] P_n(\cos\theta) \exp(-i\omega t) \quad (2.15)$$



It follows that:

$$\psi = \text{Re}[\phi] = \left| \frac{P_0}{\omega \rho_1} \right| \sum_{n=0}^{\infty} (2n+1) R_n P_n(\cos \theta) \quad (2.16)$$

$$R_n = \text{Re}(\Lambda_n i^n (U_n + iV_n) \exp(-i\omega t)) \quad (2.17)$$

in which  $U_n$  and  $V_n$  are given by:

$$\begin{aligned} U_n &= (1 + \alpha_n) j_n(\alpha_1 r_1) - \beta_n y_n(\alpha_1 r_1) \\ V_n &= \beta_n j_n(\alpha_1 r_1) + \alpha_n y_n(\alpha_1 r_1) \end{aligned} \quad (2.18)$$

where  $\alpha_n$  and  $\beta_n$  are the real part and imaginary part of the scattering coefficient  $A_n$ , respectively.

In the direction of wave propagation, the total radiation force on the three-layer model is:

$$\langle F_z \rangle = \langle F_r \rangle + \langle F_\theta \rangle + \langle F_{r,\theta} \rangle + \langle F_t \rangle \quad (2.19)$$

where

$$\langle F_r \rangle = \left\langle -\pi r_1^2 \rho_1 \int_0^\pi \left( \frac{\partial \psi}{\partial r} \right)_{r=r_1}^2 \sin \theta \cos \theta d\theta \right\rangle \quad (2.20)$$

$$\langle F_\theta \rangle = \left\langle \pi \rho_1 \int_0^\pi \left( \frac{\partial \psi}{\partial \theta} \right)_{r=r_1}^2 \sin \theta \cos \theta d\theta \right\rangle \quad (2.21)$$

$$\langle F_{r,\theta} \rangle = \left\langle 2\pi r_1 \rho_1 \int_0^\pi \left( \frac{\partial \psi}{\partial r} \right)_{r=r_1} \left( \frac{\partial \psi}{\partial \theta} \right)_{r=r_1} \sin^2 \theta d\theta \right\rangle \quad (2.22)$$

$$\langle F_t \rangle = \left\langle -\frac{\pi r_1^2 \rho_1}{c_1^2} \int_0^\pi \left( \frac{\partial \Psi}{\partial t} \right)_{r=r_1}^2 \sin^2 \theta \cos \theta d\theta \right\rangle \quad (2.23)$$

Substituting Eq. (2.16) into Eqs. (2.20)-(2.23) and using the following equations of time average:

$$\begin{aligned} \langle R_n R_{n+1} \rangle &= \frac{1}{2} \left[ \text{Re}(\Lambda_n \Lambda_{n+1}^*) (U_n V_{n+1} - V_n U_{n+1}) - \text{Im}(\Lambda_n \Lambda_{n+1}^*) (U_n U_{n+1} + V_n V_{n+1}) \right] \\ \langle R_n' R_{n+1}' \rangle &= \frac{1}{2} \left[ \text{Re}(\Lambda_n \Lambda_{n+1}^*) (U_n' V_{n+1}' - V_n' U_{n+1}') - \text{Im}(\Lambda_n \Lambda_{n+1}^*) (U_n' U_{n+1}' + V_n' V_{n+1}') \right] \\ \langle R_n R_{n+1}' \rangle &= \frac{1}{2} \left[ \text{Re}(\Lambda_n \Lambda_{n+1}^*) (U_n V_{n+1}' - V_n U_{n+1}') - \text{Im}(\Lambda_n \Lambda_{n+1}^*) (U_n U_{n+1}' + V_n V_{n+1}') \right] \\ \langle R_n' R_{n+1} \rangle &= \frac{1}{2} \left[ \text{Re}(\Lambda_n \Lambda_{n+1}^*) (U_n' V_{n+1} - V_n' U_{n+1}) - \text{Im}(\Lambda_n \Lambda_{n+1}^*) (U_n' U_{n+1} + V_n' V_{n+1}) \right] \end{aligned} \quad (2.24)$$

where the superscript “\*” denotes the complex conjugate. We obtain the following components of the radiation force:

$$\langle F_r \rangle = -\frac{2\pi r_1 p_0^2}{\omega^2 \rho_1} \sum_{n=0}^{\infty} \langle R_n' R_{n+1}' \rangle \Big|_{r=r_1} \quad (2.25)$$

$$\langle F_\theta \rangle = \frac{2\pi r_1 p_0^2}{\omega^2 \rho_1} \sum_{n=0}^{\infty} n(n+1) \langle R_n R_{n+1} \rangle \Big|_{r=r_1} \quad (2.26)$$

$$\langle F_{r,\theta} \rangle = \frac{2\pi r_1 p_0^2}{\omega^2 \rho_1} \sum_{n=0}^{\infty} \left[ n \langle R_n R_{n+1}' \rangle \Big|_{r=r_1} - (n+1) \langle R_n' R_{n+1} \rangle \Big|_{r=r_1} \right] \quad (2.27)$$

$$\langle F_t \rangle = -\frac{2\pi r_1 p_0^2}{\omega^2 \rho_1} \sum_{n=0}^{\infty} \langle R_n R_{n+1} \rangle \Big|_{r=r_1} \quad (2.28)$$

Upon substituting Eqs. (2.25)-(2.28) into Eq. (2.19), the radiation force on the three-layer model exerted by the incident focused Gaussian wave can be expressed as:

$$\langle F_z \rangle = Y_p F_0 \quad (2.29)$$

where  $F_0 = E_0 A_0$  is characteristic ARF on a cell of cross-sectional area  $A_0 = \rho r_1^2$  for a wave with characteristic volumetric energy density  $E_0 = p_0^2 / (2r_1 c_1^2)$ , and  $Y_p$  is the dimensionless ARF amplification factor that describes the degree to which the shape and heterogeneity of the cell amplify the ARF.

The dimensionless ARF amplification factor,  $Y_p$ , is thus the metric used to compare the ARF on different cells.  $Y_p$  can be calculated by:

$$Y_p = -\frac{4}{(\alpha_1 r_1)^2} \sum_{n=0}^{\infty} (n+1) \left\{ \begin{array}{l} \text{Re}[\Lambda_n \Lambda_{n+1}^*] [\alpha_n + \alpha_{n+1} + 2\alpha_n \alpha_{n+1} + 2\beta_n \beta_{n+1}] \\ + \text{Im}[\Lambda_n \Lambda_{n+1}^*] [\beta_{n+1} (1 + 2\alpha_n) - \beta_n (1 + 2\alpha_{n+1})] \end{array} \right\} \quad (2.30)$$

The series of Eq. (2.30) can be truncated when  $\Lambda_n < 0.0001$ . ARF can be obtained by substituting Eqs. (2.25)-(2.28) and (2.30) into Eq. (2.29).

## 2.5 Parametric analyses and numerical simulations

A series of parametric analyses were performed to determine how the dimensionless ARF amplification factor,  $Y_p$ , varied with the geometry and composition of cells. Finite element (FE) simulations were performed for many of these to validate the model.

The baseline geometric parameters were chosen to model an oocyte. The outer layer was taken as a homogenization of the corona radiata, zona pellucida, and vitelline membrane, with outer radius  $r_1 = 50 \mu\text{m}$  and inner radius  $r_2 = 45 \mu\text{m}$ . Because the nucleus can account for 21-50% of

cell volume<sup>88</sup>, the outer radius of the nucleus was taken as  $r_3=30 \mu\text{m}$ . Although the position of the nucleus within the cytoplasm of an oocyte can vary, it was modeled as being concentric with the other layers for simplicity.

The Gaussian ultrasound wave beam waist dimension  $W$  was set to three times the wavelength ( $W = 6\rho c/\omega$ ) for an acoustic signal with angular frequency  $\omega$ . The baseline acoustic material parameters used in all graphs and simulations are listed in Table 1.

*Table 2.1. Acoustic parameters<sup>86,89</sup>*

<b>Material</b>	<b>Density</b> $\rho_i$ (kg/m <sup>3</sup> )	<b>Speed of sound</b> $c_i$ (m/s)	<b>Impedance</b> $Z_i$ (MRayl)
Outer layer	970	1450	1.41
Cytoplasm	1000	1508	1.51
Nucleus	1430	1508.5	2.16
Water	1000	1500	1.50

FE simulations were performed using the commercial FE code COMSOL Multiphysics (COMSOL, Inc., Burlington, MA, USA). Because the Gaussian ultrasound wave field is axisymmetric, the calculation was simplified by taking advantage of axisymmetry. The “pressure acoustics” module of COMSOL was adopted to model wave propagation, and Eq. (1) was used to set the background sound field. The nucleus and surrounding medium of the FE model were meshed with linear, triangular elements, and the swept mesh method was used to create linear

quadrilateral meshes for the cytoplasm and cell membrane (Fig. 2.2). To model an infinite medium surrounding the cell, non-reflecting boundary conditions were used. The “perfectly matched layer” routine in COMSOL was used. A set of elements around the periphery of extracellular medium introduced an acoustic field through pressure boundary conditions, but cancelled acoustic energy that was received back from the medium with minimal reflection back into the medium. Convergence studies were performed to ensure grid independence for each simulation performed. In these, each element edge length was kept smaller than one sixth of the wavelength. Acoustic pressure and velocity fields in the cell and surrounding medium were obtained directly from the FE simulations. Accordingly, based on the numerical results of sound field, the ARF was calculated by using Eq. (14).

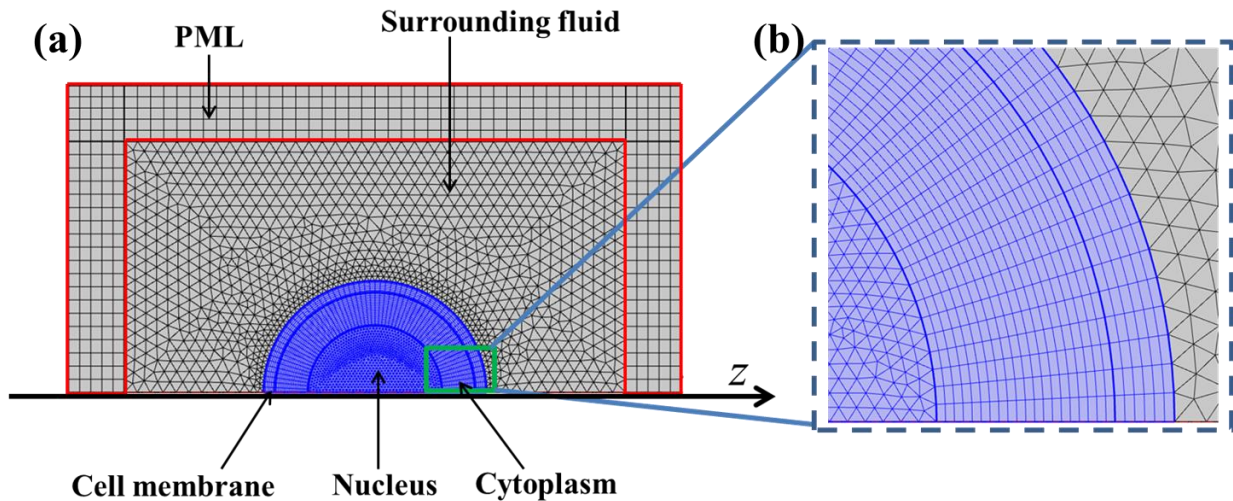


FIG. 2.2 Finite element model: (a) representative mesh for eukaryotic cell; (b) enlarged FE mesh.

## 2.5 Results and discussion

The theoretical and the finite element predictions of the ARF amplification factor  $Y_p$  were

within a few percent for all cases and acoustic excitation frequencies studied (Fig. 2.3). For an entire cell (top curve, Fig. 2.3),  $Y_p$  was a nonmonotonic function of excitation frequency, with prominent peaks and dips associated with resonant vibration. The ARF was almost entirely attenuated at low frequencies. We studied how changes to cell geometry, mechanics, and size contributed to the ARF, and how the different components of the cell affected these responses.

### **2.5.1 Influence of cell components on ARF**

We first asked how the cell membrane and nucleus contributed to the ARF on the entire cell. ARF was greatly attenuated in the absence of a cell nucleus (Fig. 2.3, plotted for the case of  $z_0 = 0$ ), as would be expected because the acoustic impedance of the nucleus is relatively large compared to that of other cell components (cf. Table 1). This result is consistent with previous observations of backscatter from cells, which is strongly dependent upon the size of the nucleus<sup>88</sup>. By contrast, changing the acoustic properties of the outer layer of the model to match those of the cytoplasm had a relatively effect on the ARF.

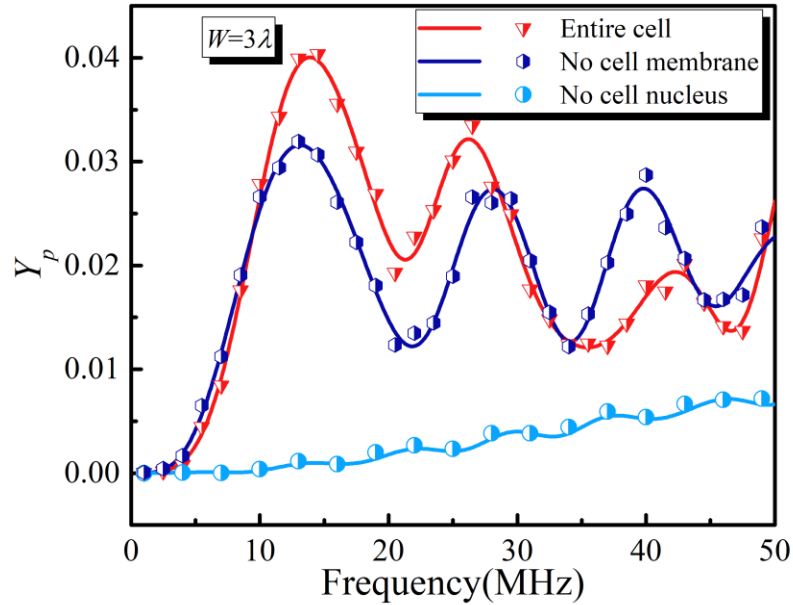


*FIG. 2.3 Acoustic radiation force amplification factor  $Y_p$  as a function of frequency for the three-layer model with  $z_0=0$ . A fictional cell with the acoustic properties of the outer layer changed to match those of the cytoplasm had a response similar to that of the full cell. However, changing the acoustic properties of the nucleus to match those of the cytoplasm attenuated  $Y_p$  substantially. Symbols: numerical simulations; curves: theoretical predictions.*

## 2.5.2 Influence of cell geometry on ARF

The relative sizes of the nuclear and outer layers of the three-layer model affected the magnitude and the frequency dependence of the acoustic radiation force amplification factor  $Y_p$  (Fig. 2.4).

In studying these, the focus was the frequency range of 1-20 MHz relevant to standard ultrasound probes, and in particular the peak ARF observed for a spherical cell in the vicinity of 13 MHz (Fig. 2.3). Note that the several factors are conflated in the contour plots of Fig. 2.4. As

above, the beam waist of the focused Gaussian ultrasound wave was fixed at  $W = 3\lambda$ . However, because  $l = 2\rho/k_1 = 2\rho c_1/w$ , the size of the beam and hence the relative sizes of these layers change as a function of excitation frequency.

Increasing nuclear radius  $r_3$  while keeping all other dimensions at their baseline values generally increased ARF (Fig. 2.4a), due to the relatively high impedance of the nucleus (Table 1) and hence the relatively higher efficiency of scattering. Increasing membrane thickness,  $l = r_1 - r_2$ , with the outer and nuclear radii fixed at their baseline values also generally increased ARF on the three-layer model (Fig. 2.4b). Because the contrast between the impedances of the outer layer and the medium is stronger than that between the cytoplasm and surrounding medium (Table 1), replacing cytoplasm with a thicker outer layer, increased the total acoustic scattering of the three-layer model and thus the ARF.

Note that the increases in  $Y_p$  are strongly dependent upon frequency. Also, due in part to the conflation of beam waist size and frequency and in part to the vibratory nature of the ARF, certain regions can frequency and size ranges can be found in which an increase in size causes a decrease in ARF. Examples include increasing nuclear radius  $r_3$  beyond  $40\ \mu\text{m}$  for an excitation frequency of 12 MHz, and increasing  $l$  for an excitation frequency of 7.5 MHz (Fig. 2.4).



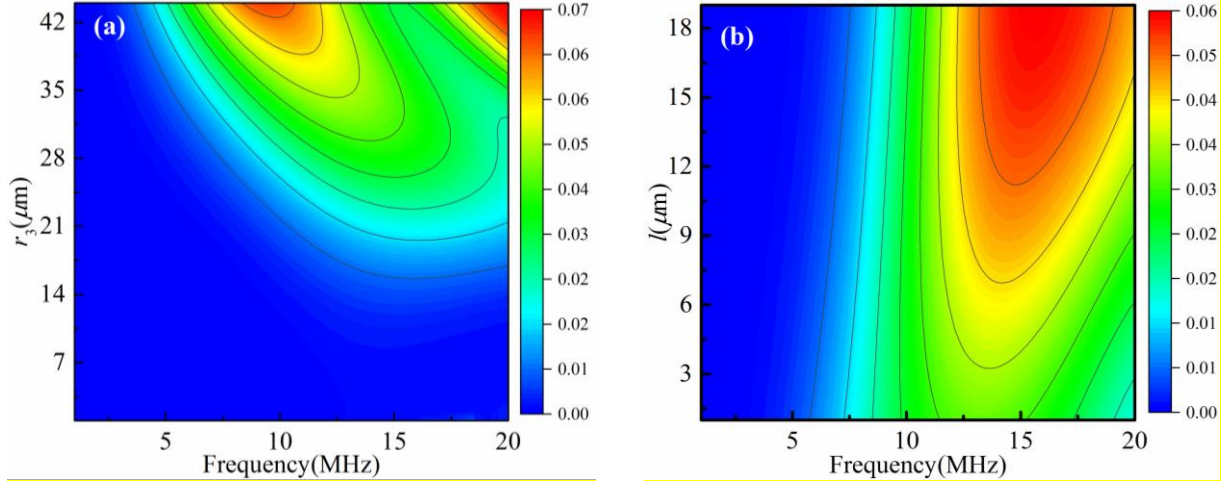


FIG. 2.4 Contour plots showing the effects of (a) excitation frequency and nuclear radius,  $r_3$ , and (b) excitation frequency and outer layer thickness,  $l = r_1 - r_2$ , on the acoustic radiation force amplification factor  $Y_p$  for a three-layered model. The beam waist of the Gaussian ultrasound wave was fixed at  $W=3\lambda$ . Baseline values:  $z_0=0$ ,  $r_1=50\mu\text{m}$ ,  $r_2=45\mu\text{m}$  and  $r_3=30\mu\text{m}$ .

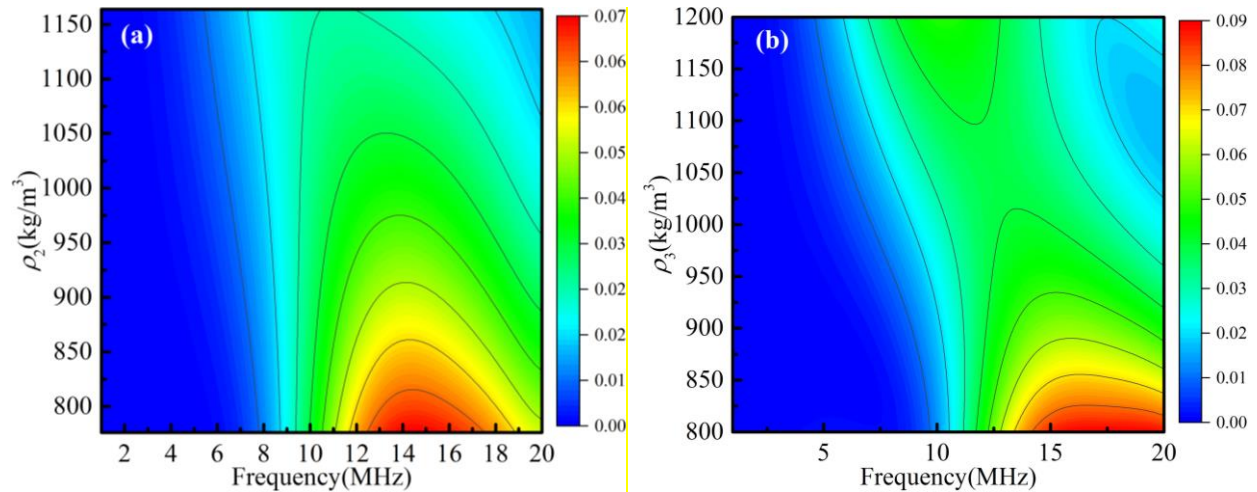
### 2.5.3 Influence of acoustic parameters on ARF

With all other parameters held at their baseline levels and again with  $W = 3\lambda$ , increasing the densities of the layers could increase or decrease the ARF, depending upon the change in contrast of the impedances and upon the vibratory nature of the problem (Fig. 2.5). Densities were varied  $\pm 20\%$  from baseline values.

Increasing the density of the outer layer over this range ( $776 \text{ kg/m}^3 \leq \rho_2 \leq 1160 \text{ kg/m}^3$ ) while holding all other densities at baseline values decreased the ARF (Fig. 2.5a). This was expected because the outer layer's acoustic impedance became closer to that of the medium and cytoplasm over most of this range ( $1.12 \text{ MRayl} \leq \rho_2 c_2 \leq 1.69 \text{ MRayl}$ ) (Table 2.1). A plateau in this trend was reached as the contrast diminished.

Varying the density of the cytoplasm from 800 to 1200 kg/m<sup>3</sup> led to a non-monotonic change in the ARF (Fig. 2.5b). As the acoustic impedance of cytoplasm increased over the range 1.20 MRayl  $\leq \rho_3 c_3 \leq$  1.80 MRayl, the ARF first decreased as acoustic impedance contrast with the outer layer and nucleus decreased, but then increased again as the acoustic impedance surpassed that of the outer layer. Although the impedance contrast with the nucleus decreased steadily over this range, the rise in ARF for higher cytoplasmic densities indicated that the contrast with the outer layer was dominant over this range.

Finally, increasing the density of nucleus from 1144 to 1716 kg/m<sup>3</sup> increased the acoustic impedance over 1.73 MRayl  $\leq \rho_4 c_4 \leq$  2.59 MRayl. Because this corresponded to a steady increase in contrast with the impedance of the cytoplasm, scattering and hence ARF increased monotonically with nuclear density.



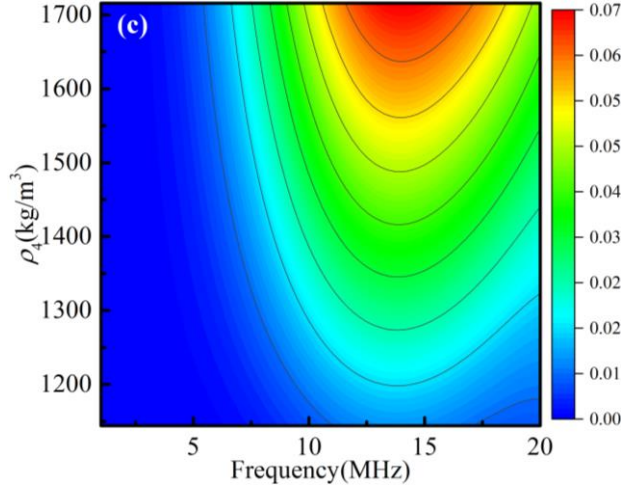
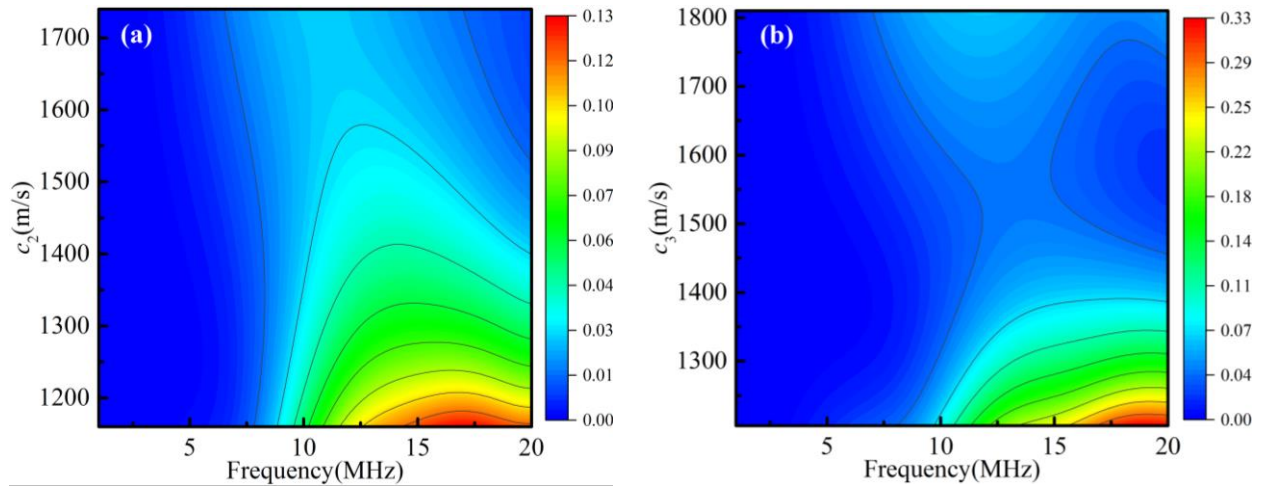


FIG. 2.5 Contour plots showing the effects on the acoustic radiation force amplification factor of (a) cell membrane density, (b) cytoplasm density and (c) nucleus density.  $z_0=0$ ,  $r_1=50\mu\text{m}$ ,  $r_2=45\mu\text{m}$  and  $r_3=30\mu\text{m}$ .

Changes of  $\pm 20\%$  to the velocity of sound had effects on the ARF identical to those in Fig. 2.5. This is expected because acoustic impedance is the product of the velocity of sound and the density within each constituent of the cell, and further confirms that acoustic impedance contrast is the key parameter that governs ARF. This underscores the utility of the present theoretical model in providing guidance for tuning ARF by changing the extracellular medium.



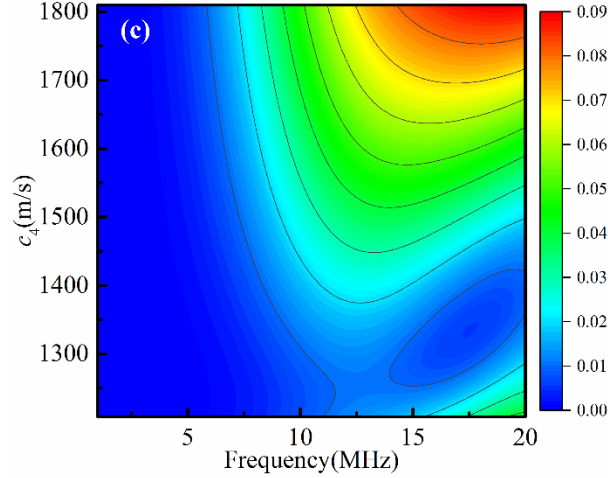


FIG. 2.6 Contour plots showing the effects on the acoustic radiation force amplification factor of (a) outer layer velocity of sound, (b) cytoplasmic velocity of sound and (c) nuclear velocity of sound.  $z_0=0$ ,  $r_1=50\mu\text{m}$ ,  $r_2=45\mu\text{m}$  and  $r_3=30\mu\text{m}$ .

#### 2.5.4 Influence of the Gaussian beam waist size

Varying the beam waist size,  $W$ , had little effect on the amplitude of  $Y_p$ , and had no effect on the locations of the frequencies for which ARF exhibited local maxima (Fig. 2.7). As  $W$  increased, the amplitudes increased slightly, although the difference between  $W = 5\lambda$  and  $W = \infty$  (which is the case of a planar wave) was almost negligible (Fig. 2.7a). The effects of beam size can be further understood by considering the spatial distribution of the scattered wave field, which follows to form <sup>90</sup>:

$$f_n(f, \theta) = \frac{2}{\alpha_1 r_1} \sum_{n=0}^{\infty} \Lambda_n (2n+1) A_n P_n(\cos \theta) \quad (2.31)$$

For a frequency of 50 MHz, at which the maximum differential was observed in Fig. 2.7a for  $1 \leq W \leq \infty$ , the scattered wave amplitude can be seen to increase with beam waist uniformly (Fig. 2.7b). However, as is evident from the separation of amplitude and angular effects in Eq.

(31), the changes in amplitude occur without altering the angular distribution of the scattering.

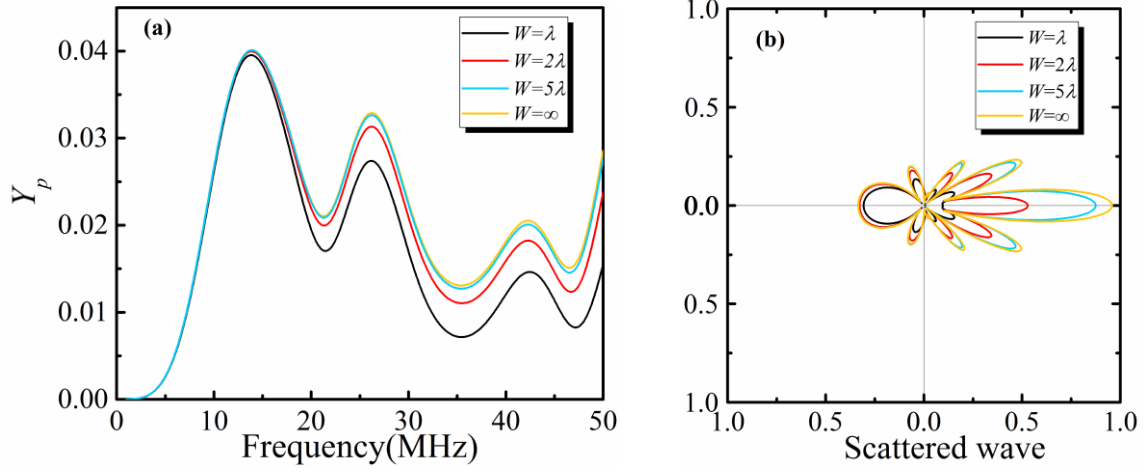


FIG. 2.7 (a) Acoustic radiation force function plotted as a function of frequency for selected values of beam waist (eukaryotic cell immersed in water, with  $z_0=0$ ,  $r_1=50\mu\text{m}$ ,  $r_2=45\mu\text{m}$  and  $r_3=30\mu\text{m}$ ). (b) Angular distribution of the scattered Gaussian ultrasound wave, with frequency fixed at 50 MHz.

### 2.5.5 Influence of cell size on ARF

The size of the eukaryotic cell affects the acoustic radiation force amplification factor  $Y_p$  (Fig. 2.8a). In studying this, we varied the cell radius  $r_1$  while maintaining the relative dimensions so that the inner radius of the outer layer remained at  $r_2 = 0.9r_1$  and the nuclear radius remained at  $r_3 = 0.6r_1$ . The beam waist of the Gaussian ultrasound wave was fixed at  $W = 3\lambda$ .

The results in Fig. 2.8 indicate that, as the size of the cell increased, the ARF peak shifted to a lower frequency, while the magnitude of this force peak remained constant. For the case of  $r_1=10\mu\text{m}$ , this peak was shifted so far that the ARF increased monotonically with frequency over the 50 MHz frequency range studied. For the other cases studied, the resonant frequencies

all shifted to lower values with increasing cell size.

The effects of cell size could be further understood by considering the backscattering of the scattered wave, which means that  $\theta = \pi$  in Eq. (31). Correspondingly, as the size of the cell increased, the peak of the backscattering amplitude  $f_n(f, \pi)$  shifted to a lower frequency without significant change in backscattering amplitude. As a result of this shift, more resonant frequencies and associated peaks appeared for larger cells over the frequency range studied. Based on these theoretical results, for smaller cells with radius ranges from 10-20  $\mu\text{m}$ , we need to increase the frequency of the Gaussian ultrasound wave to generate larger ARF.

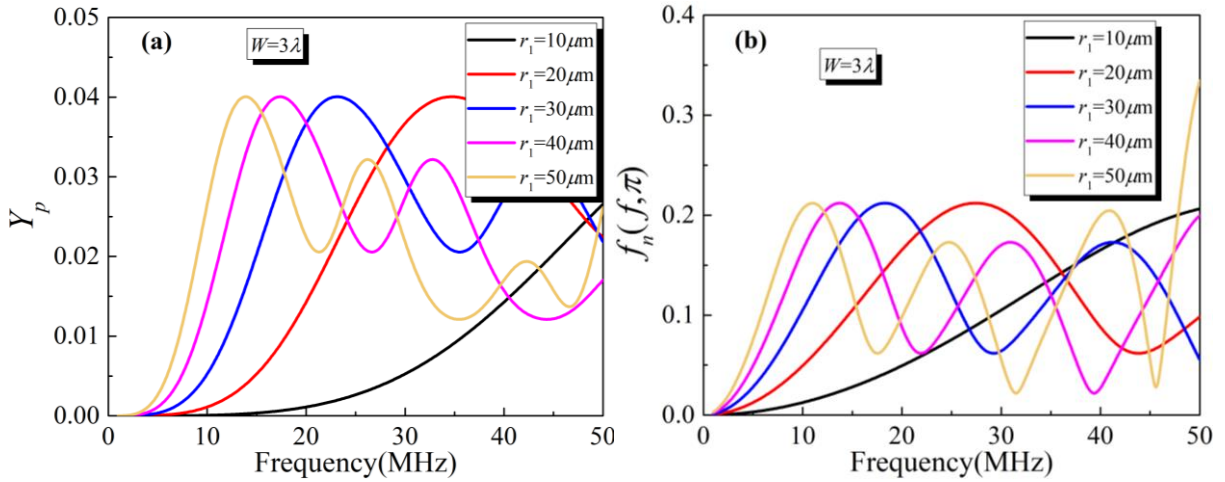


FIG. 2.8 (a) Acoustic radiation force function plotted as a function of frequency for selected values of cell radius (eukaryotic cell immersed in water, with  $z_0=0$ ,  $r_2=0.9r_1$ ,  $r_3=0.6r_1$ ,  $W=3\lambda$ ). (b) Backscattering amplitude of the scattered Gaussian ultrasound wave, with beam radius fixed at  $W=3\lambda$ .

## 2.5.6 Influence of the cell shape on ARF

Although scattering by ellipsoidal objects is challenging to study analytically, the problem is of interest because most cells elongate upon spreading. We therefore used the FE model to consider

two kinds of ellipsoidal three-layer models: prolate and oblate spheroids. The cell had an axis of axisymmetry aligned with the centerline of a focused acoustical Gaussian beam and was centered in the beam waist. Due to this symmetry, the ARF exists without any acoustic radiation torque. The partially enlarged view of the three-layer model is shown in Fig. 2.9b, with the cell membrane and cytoplasm thickness being  $5\ \mu\text{m}$  and  $15\ \mu\text{m}$ . With the reference to Fig. 2.9c, the ARF is sensitive to the aspect ratio  $b/a$ . Prolate spheroids (higher  $b/a$ , with the long axis parallel to the beam axis) have dramatically larger peak ARF. For oblate spheroids, sensitivity to aspect ratio is smaller. The reason for this is that a larger value of aspect ratio  $b/a$  means a larger curvature on the illuminated side, leading to enhanced acoustic scattering and ARF.

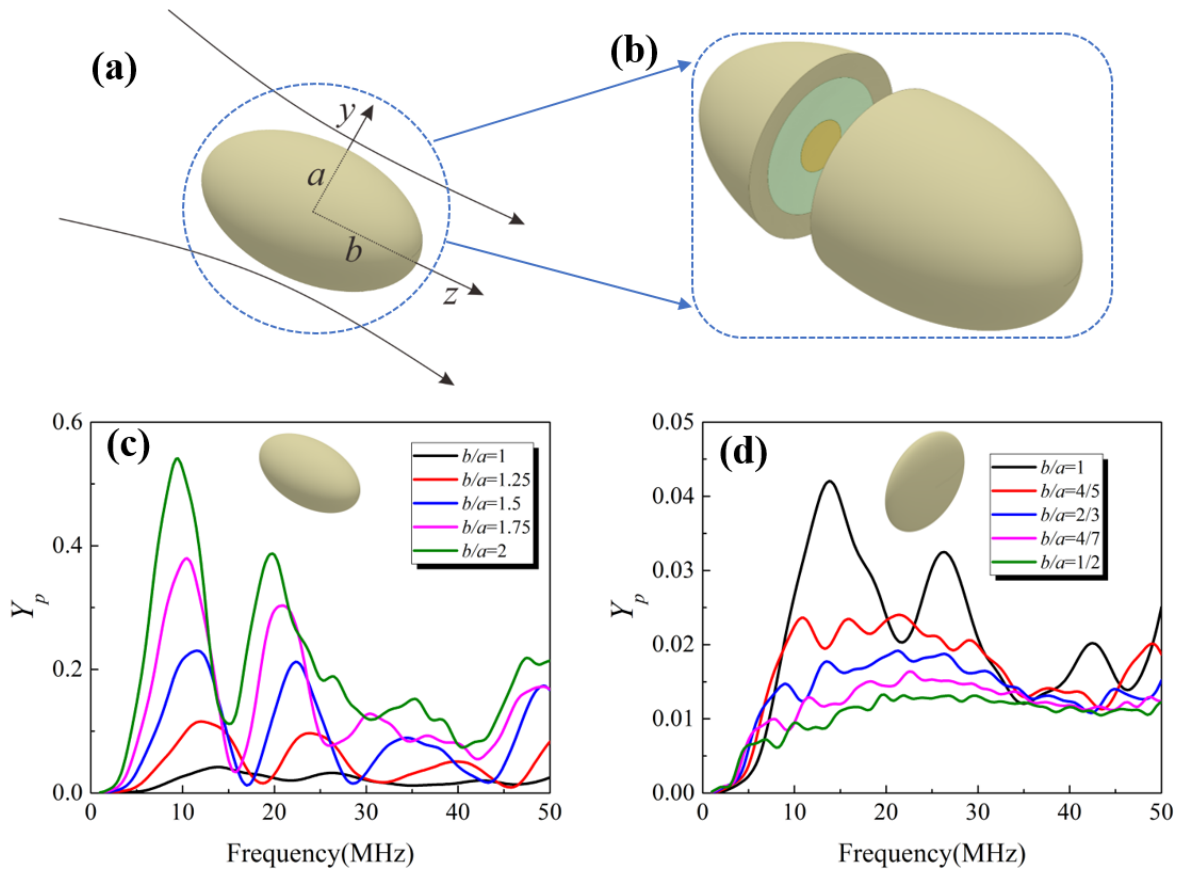


FIG. 2.9 Acoustic radiation force amplification factor plotted as a function of frequency for spheroids of varying aspect ratio. (a) Schematic of a Gaussian beam incident upon a spheroidal

*three-layer model. (b) Cross-sectional view of the spheroidal three-layer model. (c) Frequency dependence of the ARF amplification factor of a prolate three-layer model generated by a focused Gaussian wave, for several values of aspect ratio  $b/a$ . (d) Frequency dependence of the ARF amplification factor of oblate three-layer models, showing values of ARF an order of magnitude lower than those of the prolate cells in panel.*

## **2.6 Conclusions**

An analytical model has been developed to predict the acoustic radiation force (ARF) generated by a focused Gaussian ultrasound beam incident on a spherical three-layered shell (three-layer model) immersed in ideal fluid. The method of finite series is employed, with the Gaussian progressive wave simulated using spherical harmonic functions. The model is subsequently used to calculate the ARF on a eukaryotic cell suspended freely in a focused progressive Gaussian ultrasound wave. Finite element simulations are performed to validate the proposed model, with good agreement achieved. Main conclusions drawn are:

(1) As the cell membrane thickness or nucleus radius is increased, the ARF increases distinctly.

(2) The impedance of each constituent of the cell plays an important role in affecting the ARF: increasing the impedance of cell membrane reduces the ARF; as the impedance of cytoplasm is increased, the ARF decreases first and then increases; increasing the impedance of cell nucleus leads to enhanced ARF.

(3) The influence of the beam width of the Gaussian ultrasound wave on the ARF is significant only when it is relatively small.



(4) The size of the cell can significantly affect the peaks of the ARF. Larger cells show more resonant frequencies and hence more ARF peaks in the 1-50 MHz range of excitation frequencies.

(5) The aspect ratio  $b/a$  (=major axis/minor axis) of the spheroid three-layer model significantly affects the ARF.

The results presented in this study provide theoretical basis for the further development of acoustic control technology for cell trapping/sorting/assembling and drug delivery applications.

# **Chapter 3: Standing surface acoustic waves, and the mechanics of acoustic tweezer manipulation of eukaryotic cells**

## **3.1 Abstract**

Manipulation by focused ultrasound is an emerging technology with much promise for non-contact handling of microscale objects. A particularly promising approach for achieving this with living cells involves incorporating standing surface acoustic waves (SSAWs) into a microfluidic device. SSAWs must be tuned to provide the necessary range of acoustic radiation force (ARF), but models enabling this tuning have neglected the mechanics of the cells themselves, treating cells as rigid or homogenous spheres, and have also neglected energy transfer from the substrate to the fluid at the Rayleigh angle. We therefore applied Mie scattering theory to develop a model of the ARF arising from a SSAW impacting an idealized eukaryotic cell in an inviscid fluid. The cell was treated as a three-layered body with a nucleus, cytoplasm, and cortical layer. Results showed strong dependence on cell structures and the Rayleigh angle that can be harnessed to develop novel applications for cell manipulation and sorting. ARF can be tuned using the new model to both push away and pull back a cell towards the sound source. The proposed analytical model provides a foundation for design of microfluidic systems that manipulate and sort cells based upon their mechanical properties.

## **3.2 Introduction**

Recent advances in non-contact manipulation of single cells by acoustic tweezers have contributed to breakthroughs in biophysics, microbiology, and cell biology<sup>9</sup>. The sound

frequency and pressure of acoustic tweezers must be optimized to avoid damage to cells and tissues<sup>91</sup>, and to control cell positions precisely<sup>9</sup>. Standing surface acoustic wave-based (SSAW-based) acoustic tweezers are widely integrated with microfluidics for this purpose<sup>92</sup>, and 3D (three-dimensional) SSAW acoustic tweezers have been proposed<sup>61,93</sup>. Theoretical analysis of acoustic manipulation with SSAW is crucial for understanding the underlying mechanisms of acoustic tweezers and for refining the technique.

Acoustic tweezers operate through control of acoustic radiation force (ARF), a time-averaged, second-order force arising from the scattering of incident waves. To a certain extent, ARF is analogous to the optical radiation force generated by electromagnetic waves impinging upon an electrically or magnetically responsive object<sup>74</sup>. The large body of literature on the mechanisms and practical applications of ARF begins with Lord Rayleigh's pioneering work on the ARF arising from acoustic waves in compressional fluids<sup>94</sup>. Literature relevant to manipulation of cells begins in 1934, when King theoretically calculated the ARF due to a plane wave incident on a small rigid particle surrounded by inviscid fluid<sup>95</sup>. Yosioka and Kawasima extended the theory to elastic spheres, droplets, and gas bubbles by accounting for compressibility of the spherical particle<sup>96</sup>. Hasegawa further theoretically and experimentally investigated the ARF on solid elastic and viscous spheres, with no restriction placed on the size of the sphere<sup>14,97</sup>.

This early work considered only plane incident waves. Recently, other kinds of acoustic beams have been employed to improve the flexibility of acoustic manipulation, including focused Gaussian beams, Bessel beams, cross-plane beams, and SSAWs<sup>82,98-100</sup>. This includes earlier work from our group demonstrating significant effects of inhomogeneity in acoustic impedance, as can arise with a cell nucleus, on the scattering of a focused, traveling Gaussian ultrasound

wave, and on the ARF that such a traveling wave exerts on a cell <sup>100</sup>. That work identified that, for a simple, traveling waveform, the ARF can be sensitive to cell size. However, such a simplified waveform is applicable only to individual cells and is not practical for biotechnology applications involving cell populations sufficiently large to be of interest physiologically or commercially. The need to identify schemes for ultrasound activation that might be capable of delineating cell sizes in larger cell populations motivated us to develop an entirely new solution based upon more complicated standing (non-traveling) waves in a substantially more advanced device: SSAWs.

However, a theoretical study to establish a foundation for developing this technology has not yet been undertaken <sup>92</sup>. We therefore undertook such a study with the aim of improving SSAW technologies by revealing the mechanisms underlying acoustic tweezer manipulation of heterogeneous bodies like cells. Conventional theories for estimating ARF are based upon planar standing waves, and therefore fail to consider the transmission of energy from solid to fluid, and the associated influence of the Rayleigh angle, as is needed for the study of surface standing waves <sup>101</sup>. Moreover, theories for planar standing waves cannot predict the component of ARF acting perpendicular to substrate, as is needed for modeling and controlling particles or cells (Fig. 3.1a). Generally, a SSAW device consists of two identical interdigital transducers (IDTs) affixed to a piezoelectric substrate, so that the periodic redistribution of charges associated with a periodic electrical signal sent to the IDTs will cause alternating contraction and expansion of the piezoelectric substrate and produce a SSAW (Fig. 3.1a). When the SSAW contacts the liquid, vibrational energy is transferred as a bulk compressional wave in the liquid, arising at a special refracted angle, the Rayleigh angle,  $\theta_R$  <sup>102</sup>. Therefore, the bulk wave inside the fluid is not always parallel to the piezoelectric substrate.

The components of this bulk compressional wave can sum to a resultant force to that can move a cell relative to the piezoelectric substrate. The first model of this is that of Shen et al.<sup>103</sup>, who studied how the Rayleigh angle affects the ARF exerted by a SSAW on an elastic, homogeneous, spherical particle immersed in an inviscid fluid. However, eukaryotic cells typically violate the assumptions of this model because they are inhomogeneous and have nonuniform acoustic impedance, with the nucleus reported to affect wave propagation significantly. Although the model of Shen, et al. has been applied to as a first order estimate of ARF in such situations, this motivated us to extend the model to a more realistic framework for designing acoustical trapping of cells.

We therefore developed a spherically symmetric, three-layered model and calculated the ARF vector induced by a SSAW incident on a three-layered cell using the partial wave expansion method (Fig. 3.1). Results revealed significant effects of the Rayleigh angle and of the geometrical and acoustic parameters of the nucleus.

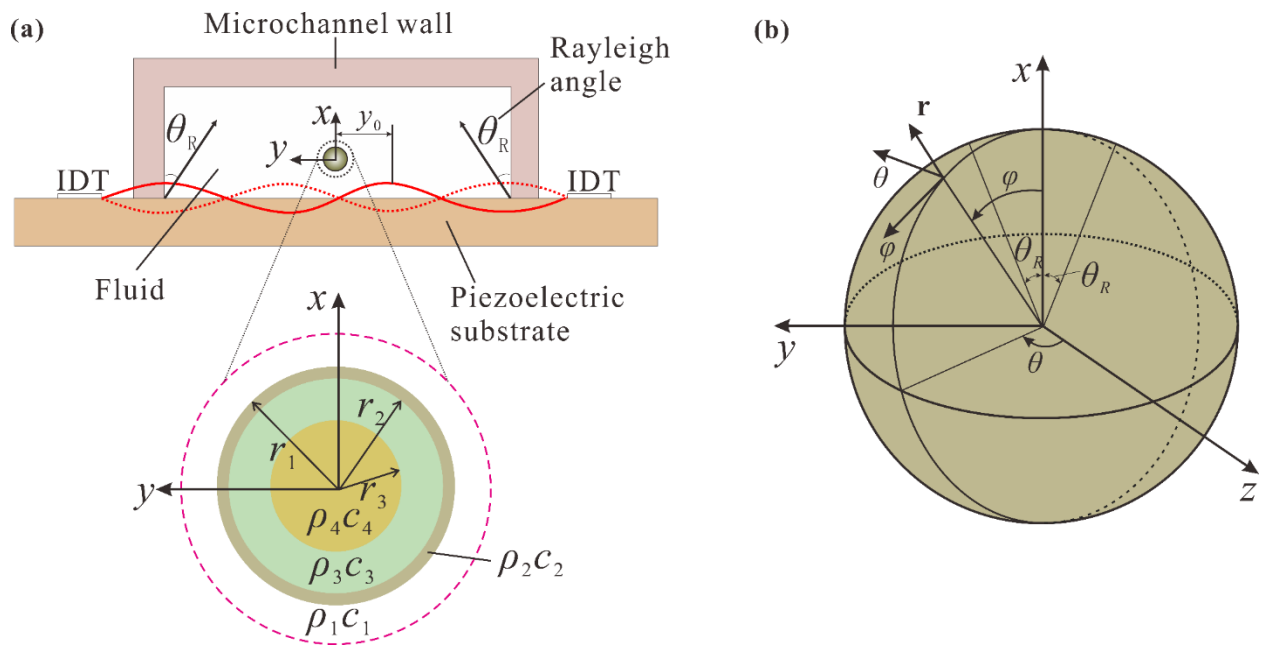


*FIG. 3.1. (a) Schematic of a SSAW incident upon a three-layered model of a eukaryotic cell. (b) The origin of the local spherical coordinate system  $(r, \theta, \varphi)$  resides at the instantaneous center of the eukaryotic cell.*

### 3.3 Theoretical model

SSAWs can be generated by two identical interdigital transducers (IDTs), fabricated on a piezoelectric substrate, that generate two progressive surface acoustic waves traveling towards one other with phase velocity  $c_s$  (Fig. 3.1a). When surface acoustic waves travel along the substrate-fluid boundary, part of the vibrational energy transports into the fluid medium, yielding two compressional waves. Each wave travels with velocity  $c_f$  at a Rayleigh angle  $\theta_R$ <sup>102-104</sup> with respect to the  $x$ -axis:

$$\theta_R = \arcsin(c_f/c_s) \quad (3.1)$$

Traveling surface acoustic waves deliver energy from the substrate to the fluid medium, causing wave energy to decay exponentially along the substrate-fluid interface. However, for practical applications based on SSAW, waves are generated in a microchannel sufficiently small relative to the decay length that this attenuation can be neglected in theoretical analysis<sup>103</sup>. Therefore, a SSAW can be regarded as two plane progressive waves having identical frequency, phase, and amplitude, and propagating along a certain angle  $\theta_R$  into the fluid medium.

In a spherical coordinate system  $(r, \theta, \varphi)$  with its origin at the instantaneous center of the eukaryotic cell (Fig. 3.1b), the velocity potential of the incident wave can be expressed as:

$$\begin{aligned}
\phi_c &= \phi_0 e^{-i\omega t} (e^{i\mathbf{k}_1 \cdot (\mathbf{y}_0 + \mathbf{r})} + e^{i\mathbf{k}_2 \cdot (\mathbf{y}_0 + \mathbf{r})}) \\
&= \phi_0 e^{-i\omega t} (e^{ik_f y_0 \sin \theta_R} e^{ik_f r \cos \gamma_1} + e^{-ik_f y_0 \sin \theta_R} e^{ik_f r \cos \gamma_2}) \\
&= \phi_0 e^{-i\omega t} \sum_{n=0}^{\infty} j_n(k_f r) X_n(\theta, \varphi; k_f y_0, \theta_R)
\end{aligned} \tag{3.2}$$

where  $k_f$  is the wavenumber of the two surface acoustic waves,  $\gamma_1$  and  $\gamma_2$  are the angles between the wave vectors (i.e.,  $\mathbf{k}_1$  and  $\mathbf{k}_2$ ) and the position vector  $\mathbf{r}$ , respectively,  $j_n(k_f r)$  is the  $n$ th order spherical Bessel function of the first kind, and the angular variation function  $X_n(\theta, \varphi; k_f y_0, \theta_R)$  is defined in the appendix. Similarly, the velocity potential of the scattered wave is expressed as:

$$\phi_s = \phi_0 e^{-i\omega t} \sum_{n=0}^{\infty} s_n h_n(k_f r) X_n(\theta, \varphi; k_f y_0, \theta_R) \tag{3.3}$$

where  $s_n$  is the scattering coefficient and  $h_n(k_f r)$  is the  $n$ th order spherical Hankel function of the first (outgoing) kind. The total wave field  $\phi_1$  in the surrounding fluid medium arises from the superposition of the incident and scattered waves, as:

$$\phi_1 = \phi_c + \phi_s \tag{3.4}$$

A eukaryotic cell suspended in a fluid medium is well approximated by a sphere<sup>105</sup>. To account for the inhomogeneity of eukaryotic cells, we consider a model of a cell having three layers with different mechanical properties, suspended within a medium of mass density  $\rho_1$  and acoustic velocity  $c_1$ . The outermost layer ( $r_2 \leq r \leq r_1$ , mass density  $\rho_2$ , acoustic velocity  $c_2$ ) represents a cortical layer that includes the plasma membrane, membrane surface proteins, and cortical actin filaments and contractile myosin motors<sup>106</sup>. This layer can range from nanometers for a mesenchymal cell to tens of micrometers for the zona pellucida surrounding an oocyte<sup>107</sup>. For suspended cells without such a layer, the effect of the nanoscale cortical layer on wave

propagation is negligible. The middle layer ( $r_3 \leq r \leq r_2$ , mass density  $\rho_3$ , acoustic velocity  $c_3$ ) contains the cellular cytoskeleton and a range of subcellular organelles, lumped into the term “cytoplasm,” which we treat as a homogeneous material. Within this is the inner layer ( $r \leq r_3$ , mass density  $\rho_4$ , acoustic velocity  $c_4$ ), a nucleus. The corresponding acoustic impedances and wave numbers are thence  $Z_i = \rho_i c_i (i = 1,2,3,4)$  and  $k_i = \omega/c_i (i = 1,2,3,4)$ , respectively,  $\omega$  being the circular frequency of incident wave. The velocity potentials  $\phi_i$  in the cortical layer, cytoplasm, and cell nucleus can be expressed directly, as detailed in the Appendix.

The three layers have shear resistance that is small compared to their resistance to dilatation, meaning that they can be approximated as a fluid acoustically<sup>108</sup>. The boundary conditions between the layers enforce continuity of normal velocity and normal stress (Fig. 3.1):

$$\begin{aligned} u^j \Big|_{r=r_j} &= u^{j+1} \Big|_{r=r_j} \\ \sigma_{rr}^j \Big|_{r=r_j} &= \sigma_{rr}^{j+1} \Big|_{r=r_j} \end{aligned} \tag{3.5}$$

where  $u^j$  and  $\sigma_{rr}^j (j = 1,2,3)$  are the normal velocities and normal stresses in the surrounding fluid medium and the suspended cell, respectively. These quantities can be obtained from the wave fields as:

$$\begin{aligned} u^j &= \frac{\partial \phi_j}{\partial r} \\ \sigma_{rr}^j &= -i\omega \rho_j \phi_j \end{aligned} \tag{3.6}$$

Incorporating Eq. (3.6) into Eq. (3.5) and using Eqs. (3.2)-(3.3) and (A1.1)-(A1.7), we can determine the scattering coefficients and then calculate the wave fields.



## 3.4 Results

### 3.4.1 ARF in the x direction

For a continuous SSAW travelling in an ideal fluid, the total ARF,  $\mathbf{F}$ , can be determined by integrating the excess of pressure  $(p - p_0)$  generated by the sound field over the instantaneous surface  $S(t)$  of the eukaryotic cell, as:

$$\mathbf{F} = - \int \int_{S(t)} (p - p_0) \mathbf{n} dS \quad (3.7)$$

where  $\mathbf{n}$  is the outward normal to  $S(t)$ . For proper evaluation of the ARF, the excess of pressure should be taken up to second-order terms in the velocity potential <sup>14</sup>. For a periodic wave, the ARF is defined as a time-averaged quantity over period  $T$  of the sound field. The time-averaged force acting on a sphere immersed in an infinite ideal fluid is given by:

$$\begin{aligned} \langle \mathbf{F} \rangle = & - \int \int_{S(t)} \langle (p - p_0) \rangle \mathbf{n} dS = - \left\langle \int \int_{S_0} \rho \langle (u_n \mathbf{n} + u_t \mathbf{t}) u_n \rangle \mathbf{n} dS \right\rangle \\ & + \int \int_{S_0} \left[ \frac{1}{2} \frac{\rho}{c^2} \left\langle \left( \text{Re} \left[ \frac{\partial \phi_1}{\partial t} \right] \right)^2 \right\rangle - \frac{1}{2} \rho \langle |\nabla \text{Re}[\phi_1]|^2 \rangle \right] \mathbf{n} dS \end{aligned} \quad (3.8)$$

where  $\langle \cdot \rangle$  is represents the time average,  $\mathbf{t}$  is the outward-pointing unit tangential vector of  $S$ ,  $S_0$  is the surface of the target at its equilibrium position,  $dS = r dr d\theta$ , and the parameters  $u_n \mathbf{n}$  and  $u_t \mathbf{t}$  are the radial and tangential components of the velocity at the surface, respectively.

The ARF generated by the SSAW can be decomposed into two forces pointing in the positive  $x$  and  $y$  directions. The force in the positive  $x$  direction,  $F_x$ , can be expressed as:

$$F_x = F_{xnn} + F_{xtt} + F_{xnt} + F_{xt} \quad (3.9)$$

where:

$$F_{xnn} = -\frac{1}{2}\rho_1 r_1^2 \int_0^\pi \int_0^{2\pi} \langle u_r^2 \rangle \Big|_{r=r_1} \sin^2 \theta \cos \varphi \, d\varphi d\theta \quad (3.10)$$

$$F_{xtt} = \frac{1}{2}\rho_1 r_1^2 \int_0^\pi \int_0^{2\pi} \langle u_\theta^2 + u_\varphi^2 \rangle \Big|_{r=r_1} \sin^2 \theta \cos \varphi \, d\varphi d\theta \quad (3.11)$$

$$F_{xnt} = -\rho_1 r_1^2 \int_0^\pi \int_0^{2\pi} (\langle u_r u_\theta \rangle \cos \theta \cos \varphi - \langle u_r u_\varphi \rangle \sin \varphi) \Big|_{r=r_1} \sin \theta \, d\varphi d\theta \quad (3.12)$$

$$F_{xt} = -\frac{\rho_1 r_1^2}{2c_1^2} \int_0^\pi \int_0^{2\pi} \left\langle \text{Re} \left[ \frac{\partial \phi_1}{\partial t} \right]^2 \right\rangle \Big|_{r=r_1} \sin^2 \theta \cos \varphi \, d\varphi d\theta \quad (3.13)$$

in which  $u_\theta$  and  $u_\varphi$  are the components of velocity in the surrounding fluid medium pointing towards the polar and azimuthal directions, respectively.

We define the dimensionless ARF in the positive  $x$  direction,  $Y_{px}$ , as:

$$Y_{px} = F_x / (S_c E) \quad (3.14)$$

where  $S_c = \pi r_1^2$  is the cross-sectional area of the entire cell and  $E = \frac{1}{2}\rho_1 k_1^2 \phi_0^2$  is the mean energy density of the incident sound wave. Incorporating Eq. (3.9) into Eq. (3.14) and using Eqs. (3.10)-(3.13), we can finally obtain the dimensionless ARF as:

$$Y_{px} = -\frac{16}{(k_1 r_1)^2} \sum_{n=0}^{\infty} (\alpha_n + \alpha_{n+1} + 2\alpha_n \alpha_{n+1} + 2\beta_n \beta_{n+1}) D_n(k_1 y_0, \theta_R) \quad (3.15)$$

where  $\alpha_n$  and  $\beta_n$  are the real and imaginary parts of the scattering coefficient  $s_n$ , respectively, and

$$D_n(k_1 y_0, \theta_R) = \sum_{m=0}^n \left[ \begin{array}{c} \frac{(n-m+1)!}{(n+m+1)!} P_n^{m+1}(0) P_{n+1}^m(0) \\ - \frac{(n-m)!}{(n+m)!} P_n^m(0) P_{n+1}^{m+1}(0) \end{array} \right] \quad (3.16)$$

$$\times \left[ \begin{array}{c} \cos^2(k_1 y_0 \sin \theta_R) \cos(m+1)\theta_R \cos m\theta_R \\ + \sin^2(k_1 y_0 \sin \theta_R) \sin(m+1)\theta_R \sin m\theta_R \end{array} \right]$$

In Eq. (3.15), each term is weighted by the factor  $D_n(k_1 y_0, \theta_R)$ , indicating that the dimensionless ARF is a function of the Rayleigh angle. When the Rayleigh angle is  $0^\circ$ , the wave fronts degenerate into a plane travelling wave in the  $x$  direction. In this case, there is no force in the  $y$  direction and the proposed theory reduces to the dimensionless ARF for a plane travelling wave. By contrast, when the Rayleigh angle is  $90^\circ$ , the generated wave degenerates into a plane standing wave in the  $y$  direction, with no force in the  $x$  direction, as can be verified by incorporating  $\theta_R = 90^\circ$  into Eq. (3.16).

The Rayleigh angle  $\theta_R$  is determined by the speeds of sound in the piezoelectric substrate and the surrounding fluid medium (Eq. 3.1). In practical applications, the Rayleigh angle varies over the range of  $1.6^\circ - 90^\circ$ <sup>103</sup>. When a SSAW is generated on the piezoelectric substrate, its wavelength  $\lambda_s$  and wavenumber  $k_s$  are determined by the IDTs. Correspondingly, the wavelength  $\lambda_f$  and wavenumber  $k_f$  in the surrounding fluid medium can be expressed as  $\lambda_f = \lambda_s \sin \theta_R$  and  $k_f = k_1 = k_s \sin \theta_R$ , respectively. In subsequent numerical calculations, the parameters as listed in Table 3.1 are used. The relative size of the nucleus varies dramatically amongst animal cells, with the nucleus taking the majority of cell volume in a resting lymphocyte, and a much smaller fraction of volume in a fat cell<sup>106</sup>. Further, the radii of cortical layer,  $r_1$ , cytoplasm,  $r_2$ , and cell nucleus,  $r_3$  are fixed at  $15 \mu\text{m}$ ,  $14 \mu\text{m}$ , and  $6 \mu\text{m}$ , respectively.

*Table 3.1. Acoustic parameters*<sup>100,108,109</sup>

<b>Material</b>	<b>Density</b> $\rho_i$ (kg/m <sup>3</sup> )	<b>Speed of sound</b> $c_i$ (m/s)	<b>Impedance</b> $Z_i$ (MRayl)
Cortical layer	970	1450	1.41
Cytoplasm	1139	1508	1.72
Nucleus	1430	1508.5	2.16
Water	1000	1500	1.50

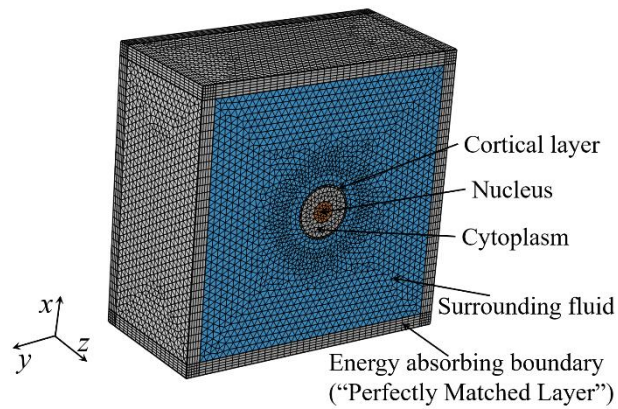


*FIG. 3.2. Representative finite element model for a eukaryotic cell in a fluid medium excited by a piezoelectric device that produces SSAWs.*

To validate the theoretical model, finite element simulations were conducted using COMSOL Multiphysics software (COMSOL, Inc., Burlington, MA, USA). Because the SSAW and the cell were both symmetric about the  $xy$  plane (Fig. 3.2), we modeled only half of the system and used symmetrical boundary conditions. The fluid medium was modeled as inviscid, enabling use of the “pressure acoustics” module in COMSOL to model wave propagation. Eq. (3.2) was used to

set the background sound field. Because microchannels are typically fabricated with sound absorptive materials, the outer boundary was modeled with a “perfectly matched layer” (PML) that absorbed all energy that entered. The cell and fluid were discretized as shown in Fig. 3.2, and convergence studies were performed by mesh refinement to ensure mesh independence for each simulation performed. The edge lengths of all elements were restricted to be smaller than one sixth of the wavelength of the fluid medium. The acoustic pressure field and the velocity fields inside the cell and the surrounding fluid were obtained directly by the finite element simulations, and the ARF was calculated from these numerical results using Eq. (3.7). A typical simulation reached convergence with 110000 elements (480000 degrees of freedom) and required 15 minutes on a laptop computer.

For illustration, with reference to Fig. 3.3(a), we consider the effect of the acoustic impedances of the cortical layer and cell nucleus while keeping the position parameter set to  $y_0 = \lambda_s/2$ , so that the cell is centered at the pressure antinodes; the Rayleigh angle was set to  $\theta_R = 20^\circ$ . The theoretical and the finite element predictions of the dimensionless ARF  $Y_{px}$  were within a few percent for all cases and for acoustic excitation frequencies studied. As the SSAW frequency increases, the curve describing the dimensionless ARF  $Y_{px}$  exhibits a series of prominent peaks and dips, due mainly to resonant vibrations of the cell, and the magnitude of the peaks decreases. The presence of either a nucleus or a cortical layer can significantly affect the ARF on the cell, with an especially strong effect of the nucleus. This is due to the strong mismatch in acoustic impedance of the nucleus relative to other components, which results in significantly effect on the scattering field. This is consistent with experiments on backscatter from cells<sup>88</sup>.

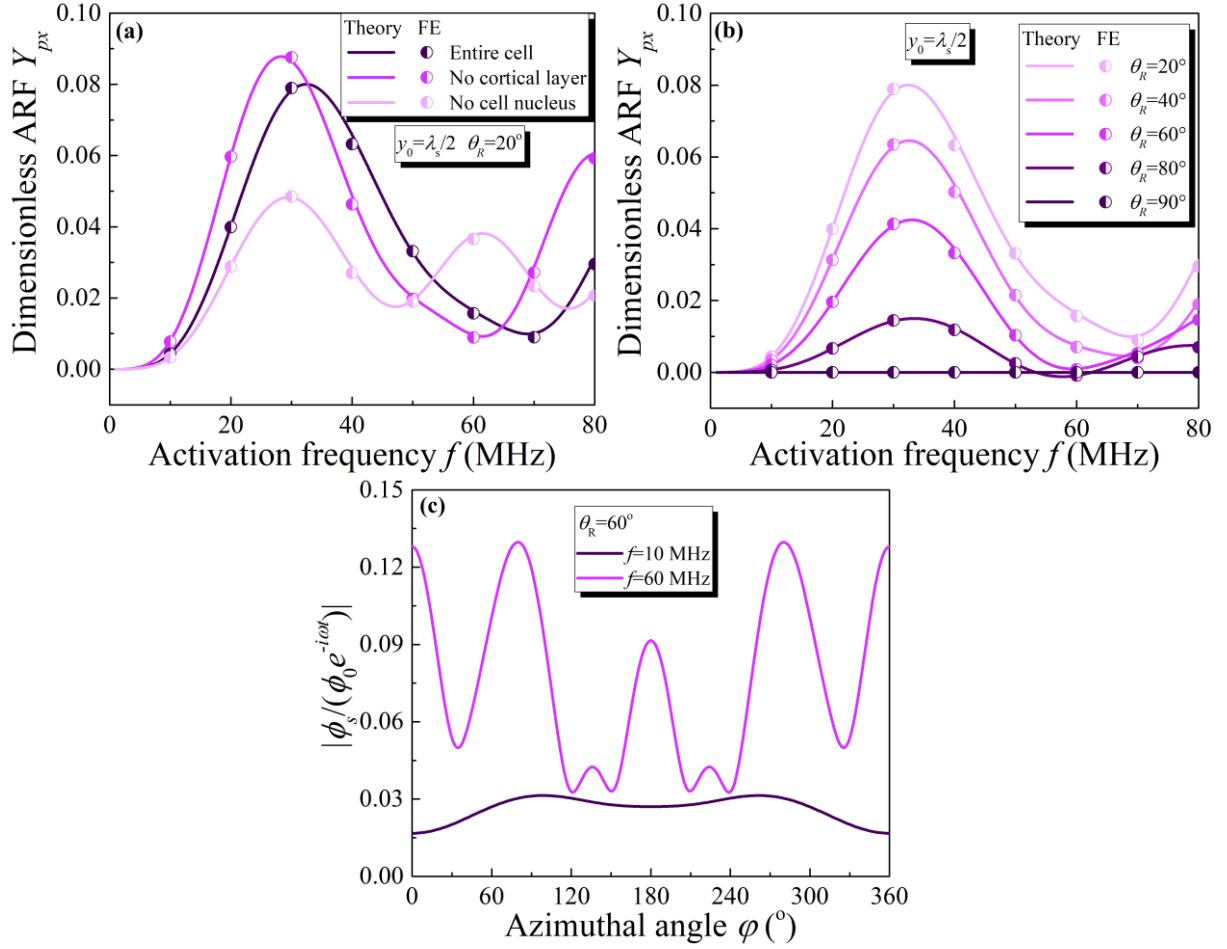


FIG. 3.3 (a) Dimensionless acoustic radiation force,  $Y_{px}$ , versus frequency for an entire cell, a cell lacking a cortical layer, and a cell lacking a nucleus. For the case shown, the cell position parameter is  $y_0 = \lambda_s/2$  so that the cell is centered at the pressure antinodes, and the Rayleigh angle is  $\theta_R = 20^\circ$ . (b) Dimensionless ARF,  $Y_{px}$ , versus frequency for an entire cell with several different Rayleigh angles. For the case shown, the position parameter is  $y_0 = \lambda_s/2$  so that the cell is centered at the pressure antinodes. For certain frequency ranges at higher Rayleigh angles, the cell is drawn back towards the substrate. (c) Normalized time-independent scattering potential for both the repulsive and attractive behavior are listed with the frequencies being 10

*MHz and 60 MHz, respectively. The Rayleigh angle is  $\theta_R = 60^\circ$ . Symbols: numerical (finite element, FE) simulations; curves: theoretical predictions.*

We next consider the effect of the Rayleigh angle (Fig. 3.3b), with the cell position again fixed at  $y_0 = \lambda_s/2$ . The dimensionless ARF  $Y_{px}$  is largest at around 32 MHz for all values of the Rayleigh angle below  $90^\circ$  with the magnitude of the peak at 32 MHz increasing with decreasing Rayleigh angle. This is expected because more energy will emerge in the  $x$ -direction with decreasing Rayleigh angle. This suggests a preferred frequency for manipulating eukaryotic cells when a large ARF is needed. Further inspection of Fig. 3.3b reveals that  $Y_{px}$  can become negative for certain frequencies at larger Rayleigh angles, indicating that the ARF in the  $x$ -direction points back towards the substrate.

This attractive force can be understood by considering the scattering potential amplitude,  $|\phi_s/(\phi_0 e^{-i\omega t})|$  and considering two excitation frequencies for the case of  $\theta_R = 60^\circ$  and  $y_0 = \lambda_s/2$  (Fig. 3.3c): the case of  $f = 10$  MHz, for which the force on the cell is repulsive, and the case of  $f = 60$  MHz, for which the force is attractive. Consider the polar angle  $\theta = 90^\circ$ . For the case of repulsion ( $f = 10$  MHz),  $|\phi_s/(\phi_0 e^{-i\omega t})|$  is higher in the hemisphere nearer the substrate ( $\varphi = 180^\circ$ ) than in the hemisphere further from the substrate ( $\varphi = 0^\circ$ ), so that the cell is pushed away from the substrate. However, when the opposite occurs, scattering is suppressed in the hemisphere pointing away from the substrate. This occurs at  $f = 60$  MHz, and an attractive force arises at this frequency, pushing the cell back towards the substrate. This phenomenon is analogous to effects that can arise on a sphere illuminated by a Bessel beam<sup>110</sup>, and is meaningful in that enables design of SSAW based acoustic tweezers that can push, trap, or pull back a eukaryotic cell toward the substrate.

The Rayleigh angle is a function of the acoustic wave phase velocity in both the fluid and on the surface of the piezoelectric substrate (cf. Equation 3.1). As such, it is a factor that can be controlled to a degree in the design of such an acoustic trapping or sorting system. Although the range of fluid phase velocity is limited somewhat by the need to grow cells in a nutritional medium, with a sound velocity on the order of  $c_f \approx 1500$  m/s, the range of piezoelectric substrata available enables substantial tunability. For example, the surface wave velocity of  $\text{Bi}_{12}\text{GeO}_{20}$  is  $c_s \approx 1680$  m/s<sup>111</sup>, for Rayleigh angle of  $\theta_R = 63.2^\circ$ , while that of  $\text{LiNbO}_3$  is  $c_s \approx 3960$  m/s<sup>112</sup>, for  $\theta_R = 22.3^\circ$ .

For cells with the parameters adopted here, a Rayleigh angle of  $22.3^\circ$  in a  $\text{LiNbO}_3$  substrate will result in a repulsive force on the cell in  $x$ -direction. By tuning this repulsive force with buoyancy and gravity, a cell can be levitated. For a  $\text{Bi}_{12}\text{GeO}_{20}$  substrate ( $\theta_R = 63.2^\circ$ ),  $Y_{px}$  is substantially smaller but still negative (Fig. 3.3b). Here, the attractive force works with gravity and against buoyancy, and can be used with denser nutrition medium to levitate cells. The range of available piezoelectric materials thus enables design of acoustic tweezer devices that can push, trap, or pull back a eukaryotic cell toward the substrate.

To assess the combinations of excitation frequency and Rayleigh angle that induce an attractive (negative) ARF,  $Y_{px}$  on an entire cell was calculated over a broad parameter space ( $40 \leq f \leq 80$  MHz and  $60^\circ \leq \theta_R \leq 90^\circ$ ). Plotting contour plots of negative values of  $Y_{px}$  for pressure antinodes ( $y_0 = \lambda_s/2$ , Fig. 3.4a) and pressure nodes ( $y_0 = \lambda_s/4$ , Fig. 4b) revealed that over the majority of parameter space (blank space, Fig. 3.4),  $Y_{px}$  is positive and the cell is predicted to be pushed away from the substrate. Comparing the two panels of Fig. 4 reveals no overlapping regions of attractive force for the two different values of  $y_0$  (colored regions, Fig. 3.4), meaning



that the excitation conditions must be tuned to provide steady attractive force, and that  $y_0$  may be varied to modulate attraction and repulsion by SSAW-based acoustic tweezers.

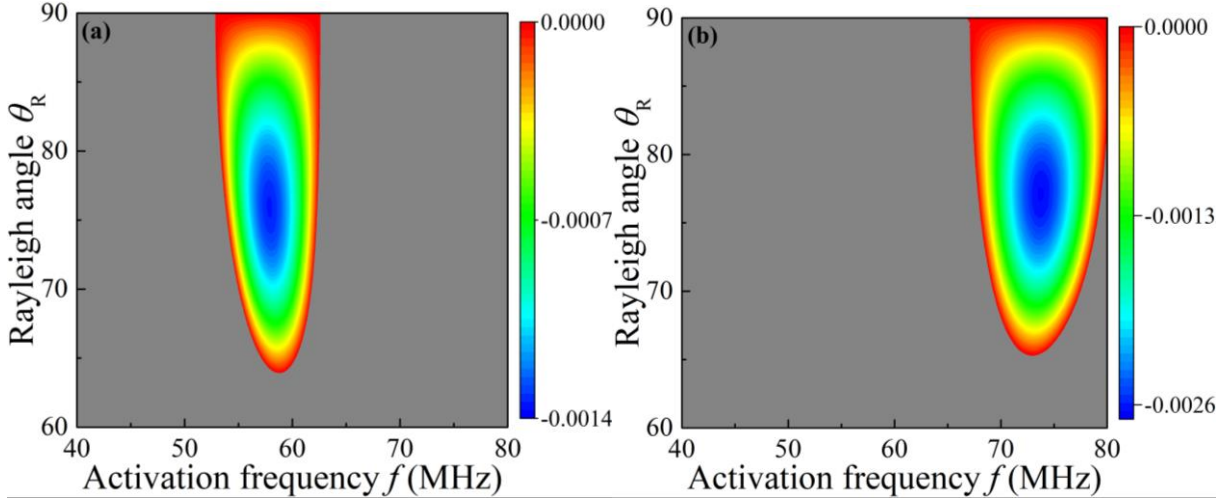


FIG. 3.4 Contour plots of negative values of the dimensionless ARF,  $Y_{px}$ , for (a) pressure antinodes ( $y_0 = \lambda_s/2$ ) and (b) pressure nodes ( $y_0 = \lambda_s/4$ ). Over the majority of parameter space (gray space),  $Y_{px}$  is positive and the cell is predicted to be pushed away from the substrate.

The variation of ARF with horizontal position  $y_0$  is examined by considering in detail the case of a single wavelength,  $\lambda_s = 100 \mu\text{m}$  (Fig. 3.5a).  $Y_{px}$  varies strongly with cell position  $y_0$ , showing a periodic dependence with a period of the wavelength ( $\lambda_s/2$ ). This periodicity, which is independent of the Rayleigh angle, arises from interference. The amplitude of the dependence increases by orders of magnitude with decreasing Rayleigh angle  $\theta_R$  (Fig. 3.5a). Inspection of the results shown in Fig. 3.5b provides further insight into the influence of  $\theta_R$  on the dimensionless ARF  $Y_{px}$ . For a three-layered cell located at the pressure antinodes ( $y_0 = \lambda_s/2$ ), there exists a threshold value of  $\theta_R$  that depends upon  $\lambda_s$ , beyond which  $Y_{px}$  drops monotonically due to the weighting factor  $D_n$  in Eq. (3.15). This threshold decreases with

increasing wavelength. This is because that changing the Rayleigh angle  $\theta_R$  here actually changes the frequency in the extracellular fluid. For  $\lambda_s = 120 \mu\text{m}$ , when the Rayleigh angle  $\theta_R$  ranges from  $30^\circ$  to  $90^\circ$ , the frequency in extracellular fluid ranges from 25 to 12.5 MHz. In this range, the dimensionless ARF  $Y_{px}$  will decrease monotonically, corresponding with Fig. 3.3b. When the Rayleigh angle  $\theta_R$  ranges from  $1.6^\circ$  to  $30^\circ$ , the frequency in extracellular fluid ranges from 448 to 25 MHz, respectively. Multiple natural frequencies of the eukaryotic cell will fall into this range and show multiple peaks and dips (Fig. 3.5b). However, due to the weighting factor  $D_n$  in Eq. (3.15), the dimensionless ARF  $Y_{px}$  will become smaller when the Rayleigh angle  $\theta_R$  increase.

The dimensionless position  $k_1 y_0$  determines the effect of Rayleigh angle on ARF (Fig. 3.5c, for  $y_0$  fixed at  $y_0 = 100 \mu\text{m}$ ). Although changing the Rayleigh angle will not change the extracellular frequency in the fluid, the sensitivity to Rayleigh angle increases with  $k_1 y_0$ . This is not due to resonance of the cell. Mathematically, larger  $k_1 y_0$  means a smaller circle for the trigonometric functions  $\cos^2(k_1 y_0 \sin \theta_R)$  and  $\sin^2(k_1 y_0 \sin \theta_R)$  in  $D_n(k_1 y_0, \theta_R)$ . Physically, changing the Rayleigh angle will change the wavelength of the travelling surface acoustic wave  $\lambda_s$  in this case. Since  $y_0 = 100 \mu\text{m}$  is held constant in Fig. 3.5c, the distance between the cell center to the antinode could be several times the period of the wavelength ( $\lambda_s/2$ ) as Fig. 3.5a shows, leading to multiple peaks and dips. The magnitude of the dimensionless ARF  $Y_{px}$  decreases with increasing Rayleigh angle as less energy propagates in the  $x$ -direction as the Rayleigh angle increases.

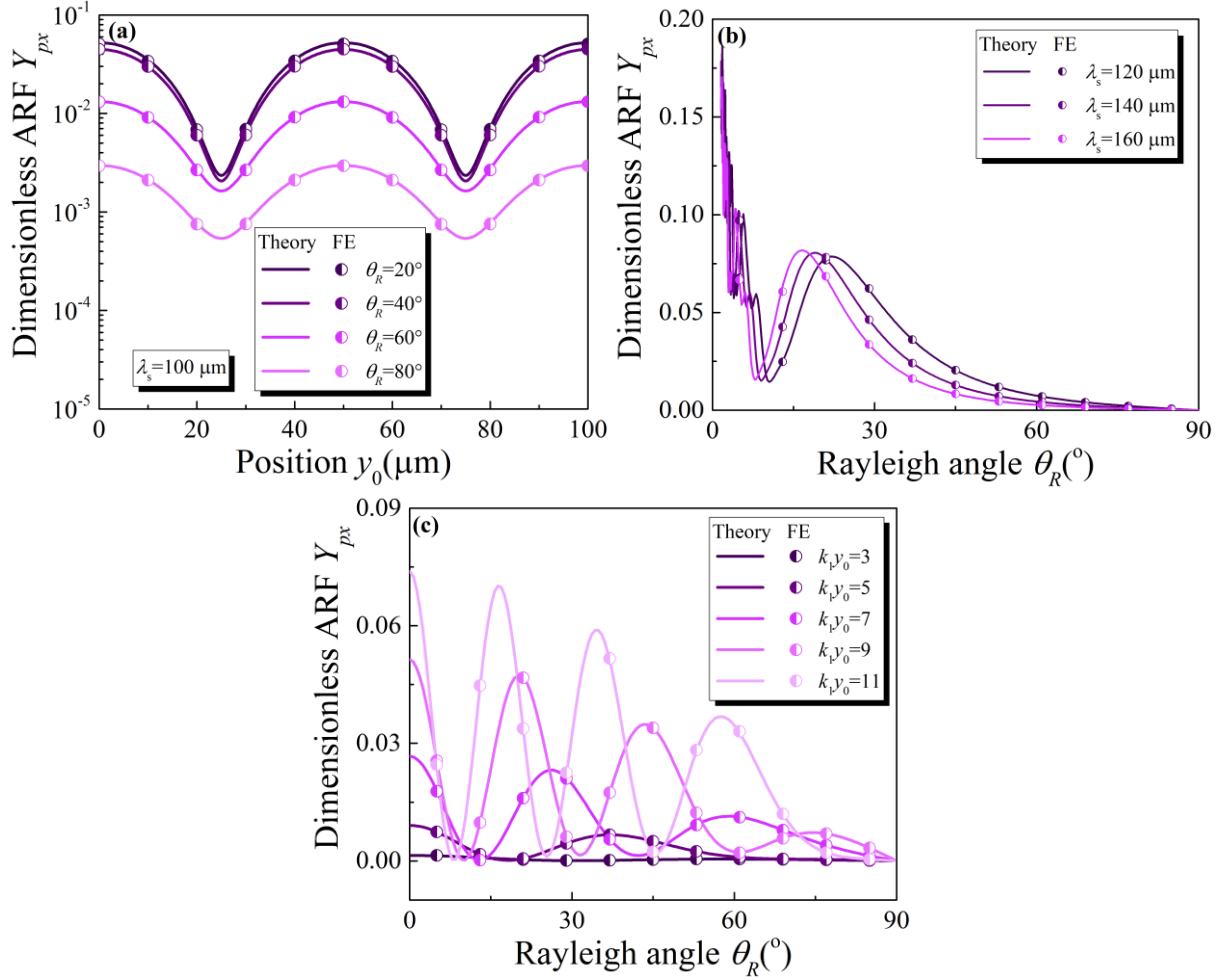


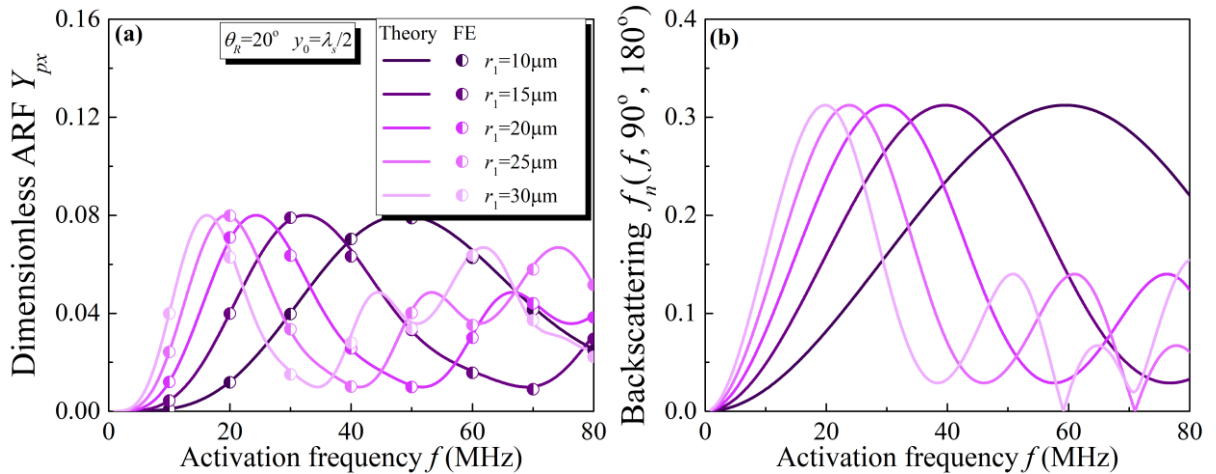
FIG. 3.5 (a) Dimensionless ARF  $Y_{px}$  plotted as a function of  $y_0$  for selected Rayleigh angles, with wavelength  $\lambda_s = 100 \mu\text{m}$ . (b) The dimensionless ARF,  $Y_{px}$ , is a strong function of the Rayleigh angle  $\theta_R$  and the wavenumber (and hence wavelength), as is evident from Eqs. (3.15)-(3.16). (c) Dimensionless ARF  $Y_{px}$  plotted as a function of Rayleigh angle  $\theta_R$  for selected  $k_1 y_0$ . Symbols: numerical (finite element, FE) simulations; curves: theoretical predictions.

For focused ultrasound, the contrast in acoustic impedance due to the nucleus of a cell has a strong effect on the ARF<sup>100</sup>. We therefore next asked two questions about the role of absolute and relative size of the nucleus. For self-similar cells of different size but with the same relative

cortical layer and nucleus sizes ( $r_2 = 14r_1/15$  and  $r_3 = 6r_1/15$ ), the ARF peak shifted to a higher frequency as cell size decreased, while the magnitude of this force peak remained constant (Fig. 3.6a, with  $\theta_R = 20^\circ$  and  $y_0 = 0$ ). For the cases studied, the resonant frequencies all shifted to lower values with increasing cell size. The effects of cell size could be further understood by considering the backscattering amplitude ( $\varphi = 180^\circ, \theta = 90^\circ$ ) of the scattered wave, which follows to form: <sup>113</sup>

$$f_n(f, \theta, \varphi)|_{\theta=90^\circ, \varphi=180^\circ} = \frac{2}{k_1 r_1} \sum_{n=0}^{\infty} i^{-n} S_n X_n(\theta = 90^\circ, \varphi = 180^\circ; k_f y_0, \theta_R) \quad (3.17)$$

Correspondingly, as the size of the cell increased, the peak of the backscattering amplitude  $f_n(f, 90^\circ, 180^\circ)$  shifted to a lower frequency without significant change in backscattering amplitude. As a result of this shift, more resonant frequencies and associated peaks appeared for larger cells over the frequency range studied (Fig. 3.6b). Based on these theoretical results, for smaller cells of radius 10-15  $\mu\text{m}$ , increasing the frequency or the sound pressure of the SSAW leads to larger ARF.



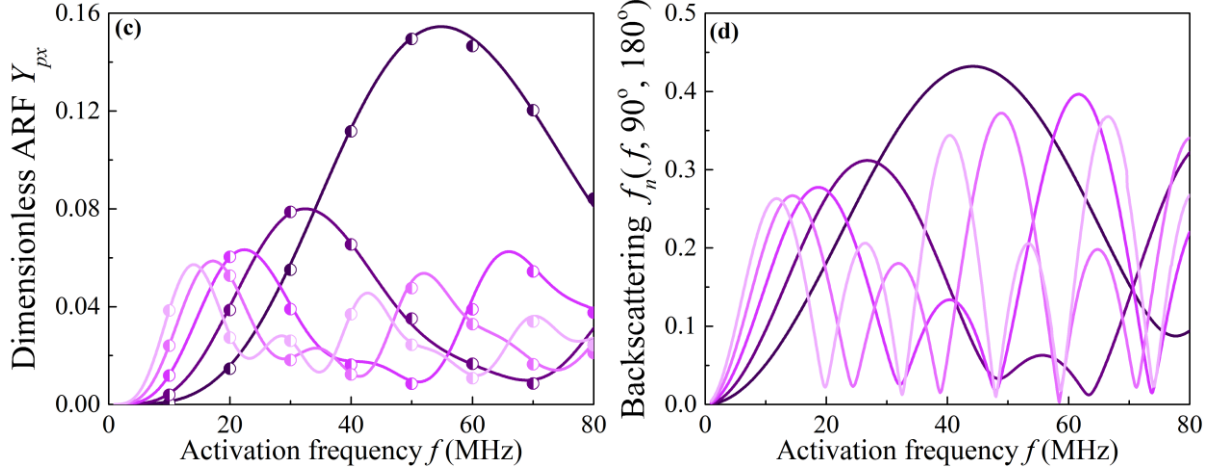


FIG. 3.6 (a) Dimensionless ARF  $Y_{px}$  and (b) backscattering amplitude as a function of frequency for selected values of cell radius (eukaryotic cell immersed in water); here, cells are self-similar, with layer sizes scaling with cell size ( $r_2 = 14r_1/15$  and  $r_3 = 6r_1/15$ ,  $\theta_R = 20^\circ$  and  $y_0 = \lambda_s/2$ ). (c) Dimensionless ARF  $Y_{px}$  and (d) backscattering amplitude for identical cells, but now with the nuclear and cortical layer sizes held constant to represent changes in volume associated with the cell cycle. Here, the thickness of the outer layer  $l = r_1 - r_2 = 1 \mu\text{m}$ , the nuclear radius is  $r_3 = 6 \mu\text{m}$ ,  $\theta_R = 20^\circ$  and  $y_0 = \lambda_s/2$ . Symbols: numerical (finite element, FE) simulations; curves: theoretical predictions.

The second question relates to how much the ARF changes over the cell cycle, in which the nuclear size stays similar but the cell volume can change substantially. Here, we held the cortical thickness and nuclear radius constant while increasing the cell volume. The ARF peak shifted to a lower frequency and the magnitude of force peaks decreased with increasing cell size (Fig. 3.6c), different from the self-similar cell case. To further understand the cell size effect, we could also check the backscattering wave with Eq. (3.17). Correspondingly, as the size of the cell increased, the peak of the backscattering amplitude  $f_n(f, 90^\circ, 180^\circ)$  shifted to a lower frequency and lower amplitude. Comparing the results in Fig. 3.6a and Fig. 3.6c, we observe that

for larger cells, the amplitude of the dimensionless ARF  $Y_{px}$  in Fig. 3.6a was larger than the counterpart in Fig. 3.6c, while for smaller cells, the converse was true as expected because of the larger nuclear size in Fig. 3.6a and the dominant role of the elevated acoustic impedance of the cell nucleus.

### 3.4.2 ARF in the y direction

Acoustic tweezers additionally require control in planes parallel to the actuator, denoted in our model as the y-direction. This force,  $F_y$  consists of four terms:

$$F_y = F_{ynn} + F_{ytt} + F_{ynt} + F_{yt} \quad (3.18)$$

where

$$F_{ynn} = -\frac{1}{2}\rho_1 r_1^2 \int_0^\pi \int_0^{2\pi} \langle u_r^2 \rangle \Big|_{r=r_1} \sin^2 \varphi \sin \theta \, d\theta d\varphi \quad (3.19)$$

$$F_{ytt} = \frac{1}{2}\rho_1 r_1^2 \int_0^\pi \int_0^{2\pi} \langle u_\theta^2 + u_\varphi^2 \rangle \Big|_{r=r_1} \sin^2 \varphi \sin \theta \, d\theta d\varphi \quad (3.20)$$

$$F_{ynt} = -\rho_1 r_1^2 \int_0^\pi \int_0^{2\pi} (\langle u_r u_\theta \rangle \cos \varphi \sin \theta + \langle u_r u_\varphi \rangle \cos \theta) \Big|_{r=r_1} \sin \varphi \, d\theta d\varphi \quad (3.21)$$

$$F_{yt} = -\frac{\rho_1 r_1^2}{2c_1^2} \int_0^\pi \int_0^{2\pi} \left\langle \text{Re} \left[ \frac{\partial \phi_1}{\partial t} \right]^2 \right\rangle \Big|_{r=r_1} \sin^2 \varphi \sin \theta \, d\theta d\varphi \quad (3.22)$$

Normalizing as above so that  $F_y = Y_{py} S_c E$ , the dimensionless radiation force  $Y_{py}$  is:

$$Y_{py} = \frac{8}{(k_1 r_1)^2} \sum_{n=0}^{\infty} (\beta_n - \beta_{n+1} - 2\alpha_n \beta_{n+1} + 2\beta_n \alpha_{n+1}) E_n(k_1 y_0, \theta_R) \quad (3.23)$$

where

$$\begin{aligned}
E_n(k_1 y_0, \theta_R) &= \sum_{m=0}^n \sin(2k_1 y_0 \sin \theta_R) \sin(2m + 1)\theta_R \\
&\times \left[ \begin{array}{l} \frac{(n-m)!}{(n+m)!} P_n^m(0) P_{n+1}^{m+1}(0) \\ - \frac{(n-m+1)!}{(n+m+1)!} P_n^{m+1}(0) P_{n+1}^m(0) \end{array} \right] \quad (3.24)
\end{aligned}$$

As above,  $Y_{py}$  is a function of  $\theta_R$  because of the function  $E_n(k_1 y_0, \theta_R)$ . When  $\theta_R = 0^\circ$ , the SSAW is a plane travelling wave in the  $x$ -direction that generates no force on the entire cell in the  $y$ -direction, as is evident from the fact that  $E_n(k_1 y_0, \theta_R)$  is zero for  $\theta_R = 0^\circ$ , and hence  $Y_{py}$  equals zero. When  $\theta_R = 90^\circ$ , the SSAW degenerates into a plane standing wave, and we recover the Hasegawa solution for a plane standing wave<sup>114</sup> upon substituting  $\theta_R = 90^\circ$  into Eq. (3.23). Cell structure affects  $Y_{py}$ , with the nucleus playing an especially important role (Fig. 3.7, with position  $y_0 = \lambda_s/8$  and Rayleigh angle  $\theta_R = 80^\circ$ ). The sign of the ARF (attractive versus repulsive) can be changed in this plane as well by adjusting the excitation frequency (Fig. 3.7a). Note the trend for  $Y_{py}$  is opposite that for  $Y_{px}$  in Fig. 3.3, with the magnitude of the first peak decreasing with decreasing  $\theta_R$  (Fig. 3.7b). This indicates that the in-plane ARF can be tuned by modulating  $\theta_R$ . Moreover, when  $Y_{py}$  is positive, the entire cell experiences a force directed to the pressure nodes; otherwise, the force is directed to the pressure antinodes, a result with clear implications for SSAW-based microfluidics.

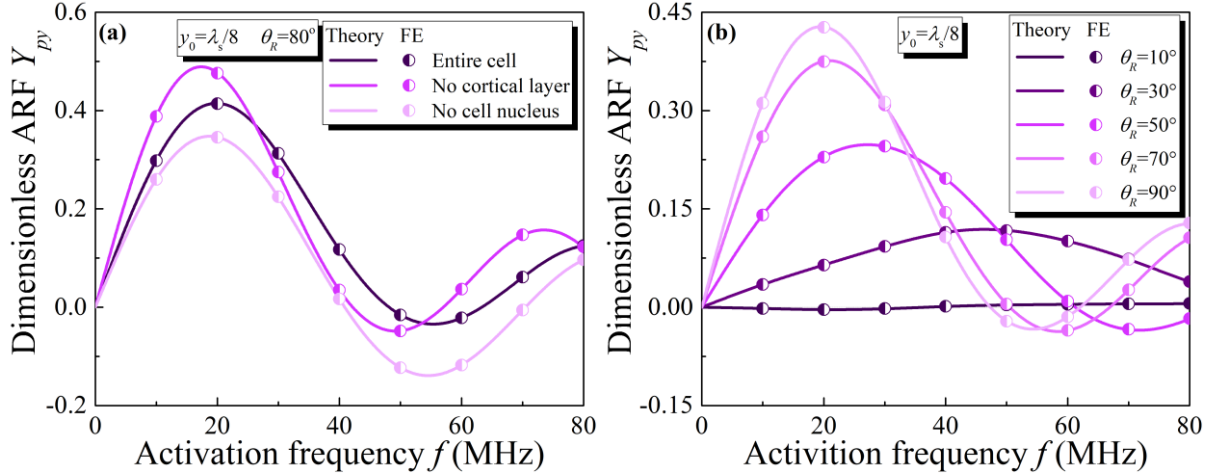


FIG. 3.7 Dimensionless in-plane ARF versus frequency of an entire cell, a cell lacking a cortical layer, and a cell lacking a nucleus. Position  $y_0 = \lambda_s/8$  and Rayleigh angle  $\theta_R = 80^\circ$ . (b) Dimensionless in-plane ARF,  $Y_{py}$ , versus frequency for an entire cell with several different Rayleigh angles. For the case shown, the position parameter is  $y_0 = \lambda_s/8$ . Symbols: numerical (finite element, FE) simulations; curves: theoretical predictions.

To establish how in-plane ARF can switch from attractive to repulsive, we plotted conditions and magnitudes for attractive (negative) ARF (Fig. 3.8, for the range  $1 \leq f \leq 80$  MHz and  $1^\circ \leq \theta_R \leq 90^\circ$ ). Equilibrium positions for a cell can be tuned by changing the frequency  $f$  or the Rayleigh angle  $\theta_R$ . This is further evident by plotting  $Y_{py}$  as a function of  $y_0$  (Fig. 3.9a, for  $\lambda_s = 100 \mu\text{m}$ ), which shows that  $Y_{py}$  is a periodic function of period  $\lambda_s/2$  due to the position-dependent term  $\sin(2k_f y_0 \sin \theta_R) = \sin(2k_s y_0)$  in  $E_n$ , with amplitude changing depending upon  $\theta_R$ . Plotting  $Y_{py}$  as a function of  $\theta_R$  (Fig. 3.9b) further highlights the influence of Rayleigh angle, and again shows that  $Y_{py}$  increases with  $\theta_R$ , which lead to more sound energy in  $y$ -direction. These results are meaningful in the design of microfluidics and highlight the critical role of Rayleigh angle in correctly predicting ARF. Again, we tested the



effect of the constant  $k_1 y_0$ . For simplicity, the distance between the cell center to the antinode  $y_0$  was fixed at  $y_0 = 100 \mu\text{m}$ . We could also find that periodic peaks and dips would emerge as the  $k_1 y_0$  increased. The reason is the same as the case for Fig. 3.5c.

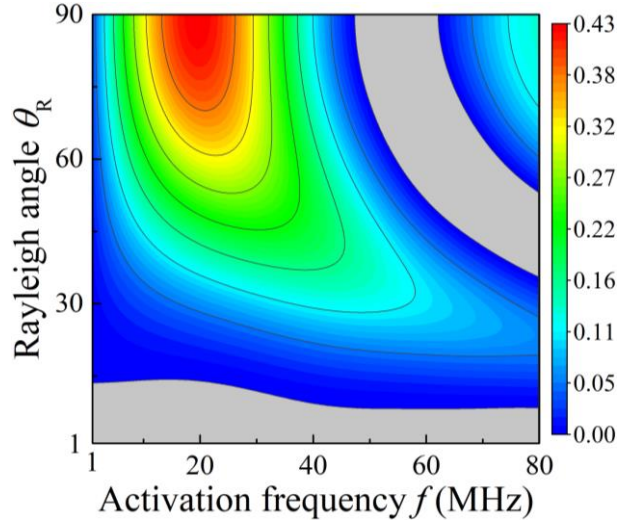
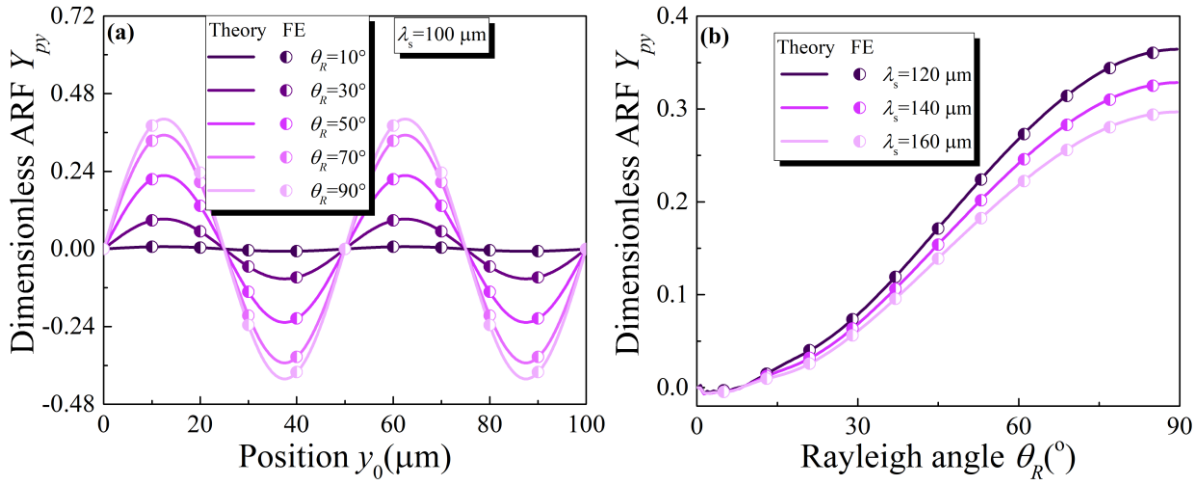


FIG. 3.8 Conditions for and magnitudes of in-plane, attractive values of the dimensionless ARF  $Y_{py}$  for a cell located at  $y_0 = \lambda_s/8$  for  $1 \leq f \leq 80$  MHz and  $1^\circ \leq \theta_R \leq 90^\circ$ .



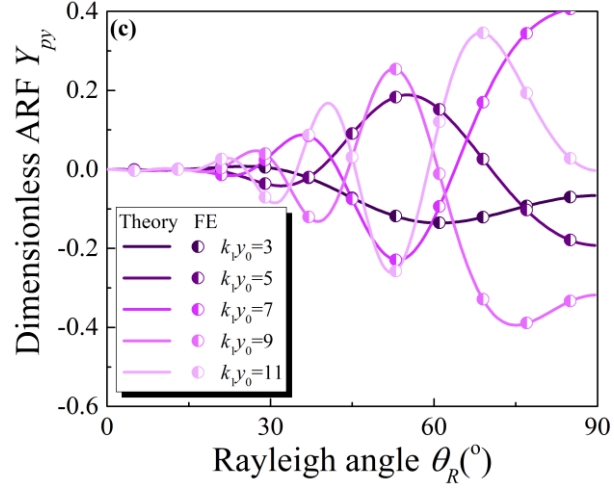


FIG. 3.9 (a) Dimensionless in-plane ARF  $Y_{py}$  plotted as a function of  $y_0$  for selected Rayleigh angles, with wavelength fixed at  $\lambda_s = 100 \mu\text{m}$ . (b) Dimensionless in-plane ARF  $Y_{py}$  plotted as a function of Rayleigh angle  $\theta_R$  for three different wavelengths, with  $y_0 = \lambda_s/8$ . (c) Dimensionless in-plane ARF  $Y_{py}$  plotted as a function of  $k_1 y_0$ . Symbols: numerical (finite element, FE) simulations; curves: theoretical predictions.

To assess the role of cell and nucleus size on in-plane forces, we again varied cell radius  $r_1$  while maintaining relative dimensions ( $r_2 = 14r_1/15$  and  $r_3 = 6r_1/15$ , with  $\theta_R = 80^\circ$  and  $y_0 = \lambda_s/8$ ). As cell size increased, the  $Y_{py}$  peak shifted to a lower frequency, while the magnitude of this force peak remained constant (Fig. 3.10a). Cell size can affect the sign of  $Y_{py}$  so that cells will gather to the pressure antinode or the pressure node based on the cell size, suggesting a mechanism for acoustic cell sorting using SSAW. When plotted with nuclear and cortical dimensions held constant while cell volume changed, the  $Y_{py}$  peak shifted to a lower frequency and the force amplitude decreased (Fig. 3.10b). This was again expected because the cell nucleus size was different for the two cases in the two figures. The results shown in Fig. 3.10b also suggest that we can design SSAW based acoustic tweezers that sorting cells based on

phase of the cell cycle.

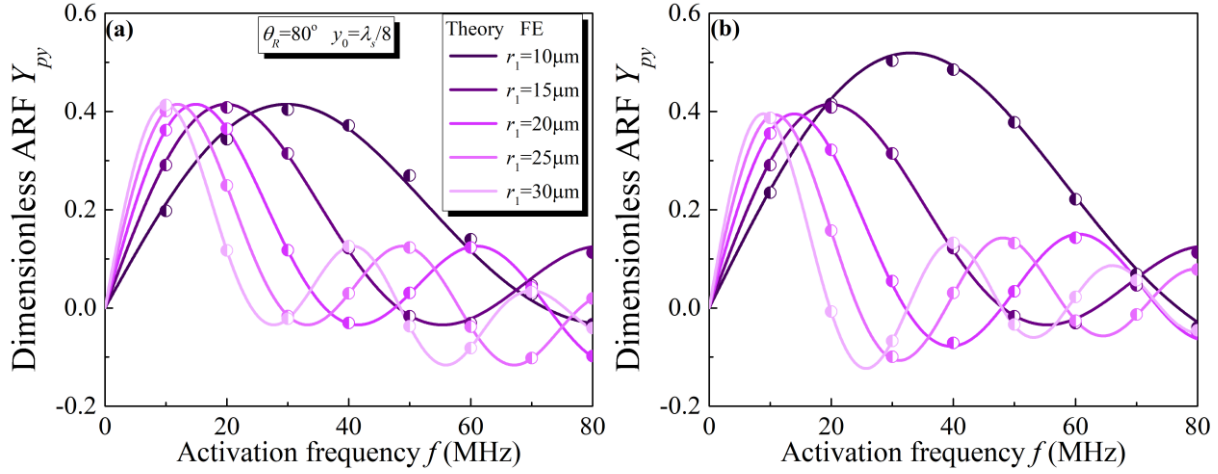


FIG. 3.10 (a) Dimensionless in-plane ARF  $Y_{py}$  plotted as a function of frequency for selected values of cell radius, with  $r_2 = 14r_1/15$ ,  $r_3 = 6r_1/15$ ,  $\theta_R = 80^\circ$ , and  $y_0 = \lambda_s/8$ . (b)

Dimensionless in-plane ARF  $Y_{py}$  plotted as a function of a cell circle, but now with the nuclear and cortical layer sizes held constant to represent changes in volume associated with the cell cycle. Here, the thickness of the outer layer  $l = r_1 - r_2 = 1 \mu\text{m}$ , the nuclear radius is  $r_3 = 6 \mu\text{m}$ ,  $\theta_R = 80^\circ$  and  $y_0 = \lambda_s/8$ . Symbols: numerical (finite element, FE) simulations; curves: theoretical predictions.

### 3.5. Conclusion

We have shown that the design of SSAW microfluidic devices to manipulate cells is strongly dependent upon the Rayleigh angle of the system and the heterogeneous mechanics of the cells, neither of which had previously been explored theoretically. Our results extend the state of the art analysis to include waves other than plane standing waves, and to assess the effects of the Rayleigh angle and of cell mechanics. The theoretical model we derived reduced to earlier, simpler solutions for planar standing and planar traveling waves. It provided exact solutions for

scattering coefficients, and a near-field approximation for the ARF.

These exact solutions have a number of limitations that bear mention. The first is that the mechanical properties of cells depend strongly upon the way that they are loaded<sup>115-118</sup>. The numbers used in the studies here are all derived from experiments that involve large perturbations of cells, but the application of ultrasound involves minimal deformation and relatively low stresses. The results presented may enable the estimation of mechanical properties at very low levels of cell deformation based upon motion in response to ARF. Second, the membrane of most cells is decorated with proteins that complicate the definition of a cortical layer thickness<sup>106</sup>. However, for most cells other than oocytes, the cortical layer is reduced in size in suspension and may not be a strong factor. Inside a tissue or a tissue construct, cells often surround themselves with a coating of extracellular matrix proteins that changes over time, even in cells that stay nominally round<sup>119-122</sup>. This layer is typically much larger than the lipid membrane, in which case variations of the latter pose less of a concern.

Results show that consideration of the Rayleigh angle and cell mechanics are critical, and that these factors offer new handles with which to control cell manipulation and cell sorting. In the direction normal to the piezoelectric substrate, our model reveals that there is a non-zero component of the ARF that can be used to push a cell away or pull it back towards the sound source; prior theories fail to predict this phenomenon. The acoustic impedance mismatch between the cell nucleus and other cell components affects the ARF, as does the Rayleigh angle, the latter being a factor that can be tuned to switch ARF from attractive to repulsive. Within planes parallel to the piezoelectric substrate, the Rayleigh angle can be tuned to manipulate cells and sort them based upon size, mechanical properties, and phase within the cell cycle. Our model and results provide a theoretical foundation for harnessing the mechanical properties of cells to

develop acoustic control for cell trapping, sorting, and manipulation.

# Chapter 4: Mechanical memory in ion channel function

## 4.1 Abstract

Ultrasound activation of mechanosensitive ion channels holds promise for therapies ranging from cardiac pacing to neuromodulation. However, the mechanisms by which ultrasound activates these channels are a source of debate, with fluid flow, membrane strain, membrane heating, and local cavitation all possibilities. Here, we show by direct observation of strain fields and transmembrane current that cumulative membrane creep associated with ultrasound activation controls transmembrane current in *Xenopus* oocytes containing TRAAK channels. Integrated experiments and modeling confirmed that membrane viscoelasticity enabled ion channels to remember previous mechanical loadings. Results show that membrane currents can be activated using sound pressure, and suggest potential pathways for using pulsed ultrasound to cumulatively increase membrane currents with a minimal heating of tissue.

## 4.2 Introduction

Although electrical stimulation techniques are effective in treatment of pathologies ranging from depression<sup>16</sup> to Parkinson's disease<sup>17</sup> to cardiovascular disease<sup>123</sup>, technologies for enabling the necessary control of ion channels in specific cells are either invasive<sup>18,20</sup> or require laboratory equipment<sup>19</sup>. Ultrasound can carry energy noninvasively through the bone to deep tissue<sup>21</sup>, and has been used for a century to modulate electrically excitable tissues including myocardium<sup>22</sup>, the central nervous system<sup>23,24,124</sup>, and retinal cells<sup>125</sup>. The possibility of applying these technologies for neuromodulation is supported by experiments both *ex vivo*<sup>25-27</sup> and *in vivo*<sup>29</sup>,

but the molecular basis by which this works remains unknown. A broad range of mechanisms has been proposed, including the opening of mechanosensitive ion channels by stresses from microbubble cavitation<sup>31</sup>; opening of thermosensitive TRPV1 channels by heating of tissue from ultrasound irradiation<sup>32,126</sup>; opening of shear stress sensitive Piezo1 channels from fluid flow arising from gradients in ultrasound pressure<sup>26</sup>; and direct activation of mechanosensitive MscL or I92L channels by ultrasound<sup>25</sup>. Although the mechanism for this latter effect is unknown, acoustic radiation force has been proposed to explain ultrasound neurostimulation of retinal cells<sup>33</sup>. However the mechanisms by which cells might transduce acoustic radiation force and the relationships between the electrophysiology and mechanobiology remain a source of debate<sup>34</sup>. We tested the hypothesis that mechanosensitive ion channels can be opened by tension in the cell membrane, and found that sound pressure from ultrasound and the viscoelasticity of the cell and membrane interact to control membrane channel opening.

## 4.3 Results

The model system we investigated was *Xenopus laevis* oocytes to which cRNA for a mechanosensitive ion channel was added (see Methods for details). *Xenopus* oocytes were chosen because they have no known competing mechanosensitive ion channels. Amongst the choices of mechanosensitive ion channels to study were K2P (TREK-1, TREK-2, TRAAK)<sup>30</sup>, Piezo 1<sup>26</sup>, and MscL channels<sup>25</sup>. The TRAAK channel, a two-pore K2P ion channel, was chosen because it can be activated with membrane stretch and has a low probability of opening in the absence of membrane tension<sup>127</sup>.

When these cells were subjected to ultrasound excitation of 1 MHz, well within the clinical

frequency range of 0.2-3 MHz, at a sound pressure of less than 0.3 MPa, transmembrane electric current could be observed from the readout of a two-voltage clamp, indicating ultrasound-induced activity of the TRAAK channel (Fig. 4.1a). In these experiments, the oocyte membrane voltage was first held at  $-80$  mV, then stepped to  $+40$  mV for 10 s, and finally returned to  $-80$  mV. In the absence of ultrasound, (black line in Fig. 4.1b), transmembrane current rose as expected to a plateau when the voltage was stepped to  $+40$  mV, then dropped when the voltage was returned to  $-80$  mV, in both cases with an expected overshoot due to membrane capacitance<sup>27</sup>. When this was done with subsequent application of ultrasound for 1 s (at  $t = 3$  s, red bar on the bottom of Fig. 4.1b), current increased with time at a rate that increased with increasing sound pressure. The current rose to a peak that also increased with increasing sound pressure, then decayed towards the baseline seen in the absence of ultrasound after the application of ultrasound ended at  $t = 4$  s.

All experiments were conducted in a sequence from a lower to a higher ultrasound pressure. As experiments progressed, an increasingly large gap formed between the (black) baseline current and the red treatment cases  $t = 1-3$  s. These effects were robust and repeatable. We hypothesized that this arose either due to ultrasound causing permanent changes to membrane currents, or due to an effect of cell viscoelasticity on channel activity. Because the experiments were repeatable after the cell was given a sufficient recovery interval (Fig. 4.1d), the first hypothesis was falsified.

To test the second hypothesis, we tested two predictions. First, the acoustic radiation pressure arising from ultrasound must be sufficient to cause appreciable mechanical deformation of the oocyte. Second, the effects of ultrasound pressure on membrane current, if applied repeatedly over intervals that were short compared to the viscoelastic recovery times, must show a



cumulative, creep-like increase.

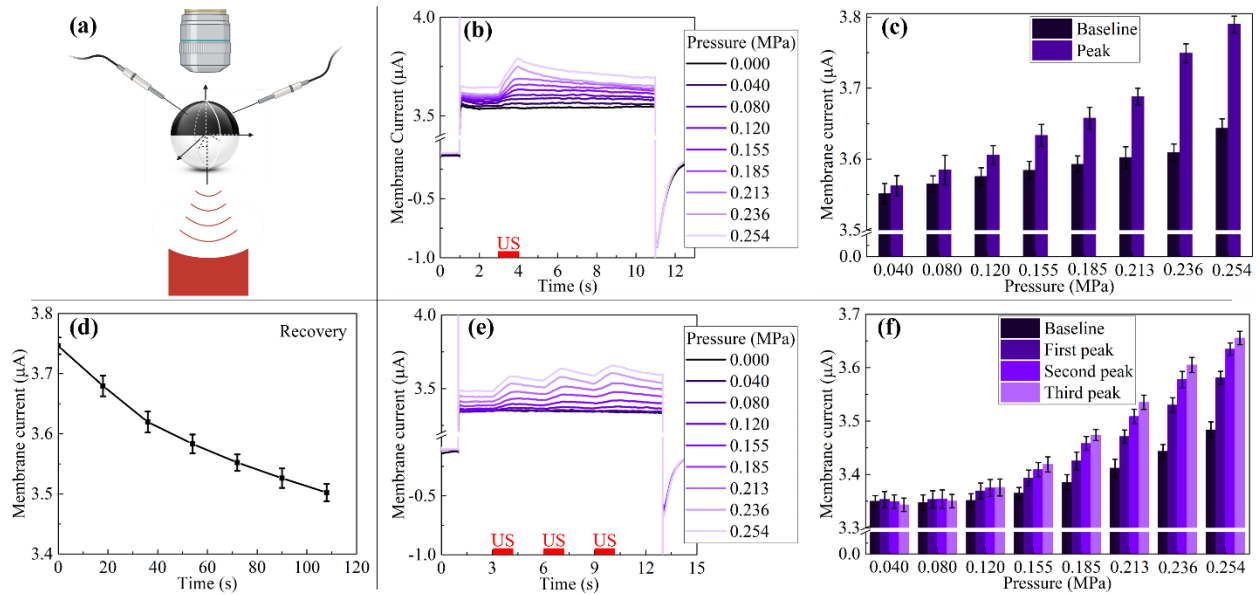


**FIG. 4.1** Functional expression of TRAAK channels in *Xenopus oocytes*. (a) Experimental set-up. A *Xenopus oocyte* expressing TRAAK channel is placed in the focus of the ultrasound field. The membrane current was recorded by using the two-electrode voltage clamp. (b) Effects of ultrasound on TRAAK channels. The membrane voltage was held at  $-80$  mV before stepping to  $40$  mV (time 3 s). After 10 s, the membrane voltage returned to  $-80$  mV. The black line shows the current without ultrasound activation. To test the effects of ultrasound, we turned on the ultrasound at time 3 s and lasted for 1 s. The sound pressure was increased gradually from 0.04 MPa to 0.254 MPa. 5 s period was held before next sequence. (c) The comparison between the membrane current before the ultrasound sound activation and the current at the end of the activation. (d) After the ultrasound activation, we turned off the ultrasound and ran more sequences. The current would decrease gradually. (e) Periodic loading. Membrane current showed cumulative, creep-like increase. (f) The comparison between the membrane current for baseline and the peak value of each ultrasound activation.

To test the first prediction, we explored whether measurable strain fields would be evident in the oocytes subjected to ultrasound. Strains can result from acoustic radiation pressure that arises as a nonlinear effect of an ultrasound pressure wave's momentum flux scattering when the wave impinges on the oocyte<sup>5,128</sup>, analogous to optical radiation force<sup>74</sup>. We used a noise-insensitive strain mapping technique<sup>129,130</sup> to estimate strain fields in from brightfield images taken in a focal plane that included a stiff and relatively immobile glass electrode; the stiff electrode minimized out-of-plane motion (Fig. 4.2a). Acoustic radiation pressure caused motion of the oocyte relative to the two electrodes, leading to local strain concentrations around the electrodes (Fig. 4.2a) that expanded with increasing exposure to ultrasound (Fig. 4.2a).

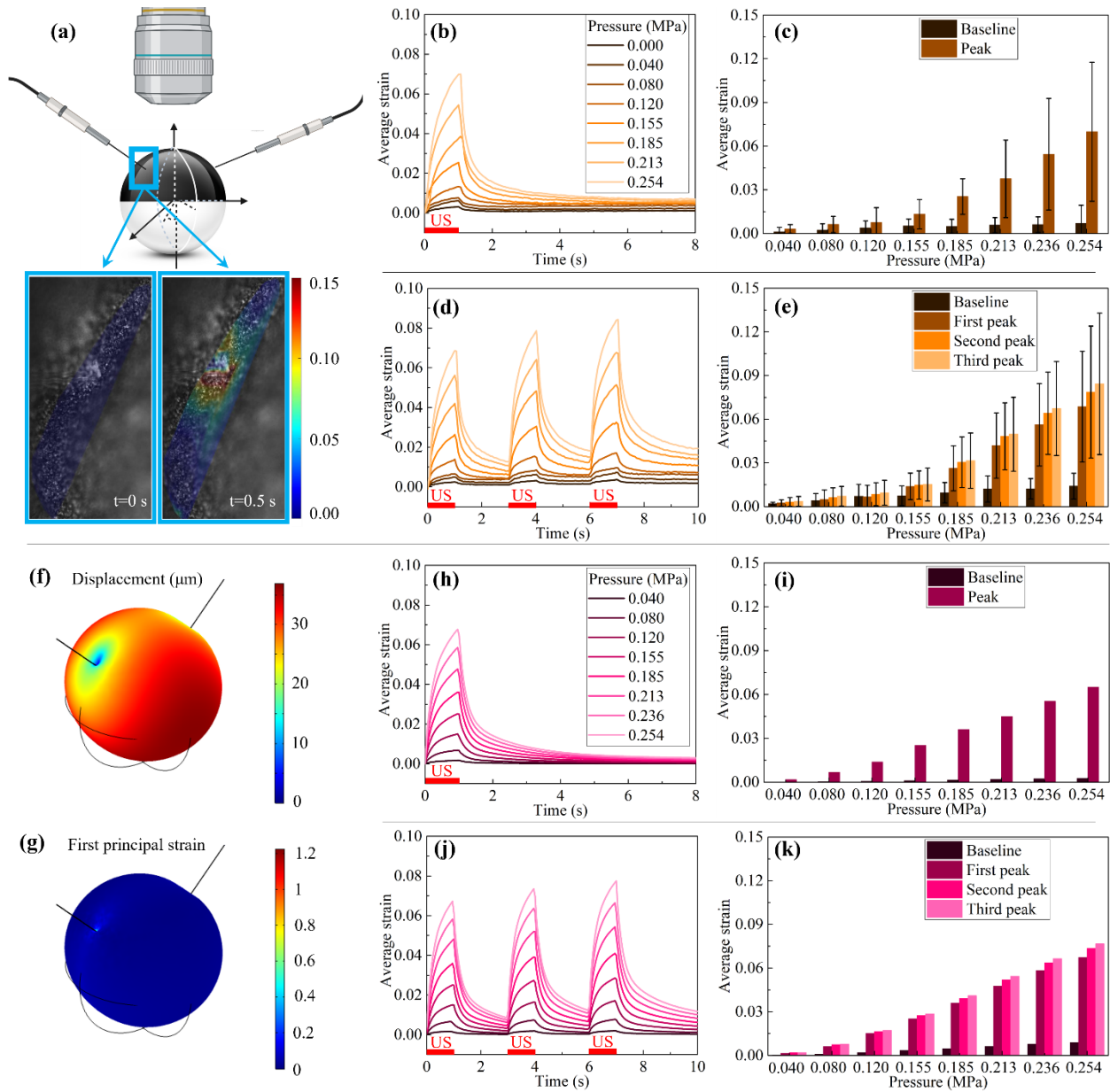


FIG. 4.2 (a) 'Direct Deformation Estimation' algorithm (DDE) was used to calculate the first principal strain  $t=0$  s, and  $t=0.5$  s. Averaged first principal strain versus time. The image before the moment we turned on the ultrasound was used as the reference image for the following warping to get the estimated deformation gradient. After that, a direct calculation of averaged first principal strain could be obtained for a (b) 1-second ultrasound activation and (c) comparison between the peak value and the strain before the ultrasound. (d) Periodic loading

*for the strain change. (e) The corresponding peak strains for each ultrasound activation. The color from dark to light means the sound pressure increase gradually. Simulated spatial profiles of cell mechanics. (f) Displacement and (g) First principal strain change for the oocyte under the activation of ultrasound. Averaged first principal strain versus time by FEM in COMSOL. (h) 1-second activation, (i) comparison between the peak average strain and the baseline value. (j) and (k) are the corresponding results to show the periodic loading. The color from dark to light means the sound pressure increase gradually.*

This behavior was consistent with the first prediction. To test the second prediction, we checked whether viscoelastic deformation would increase cyclically when the ultrasound was pulsed three times for 1 s (beginning at  $t = 3$  s), with 2 s of recovery between pulses (Fig. 4.2d). These experiments confirmed that the membrane exhibited viscoelastic creep.

To test the hypothesis that membrane currents were correlated with membrane viscoelasticity, we measured membrane currents in these cyclical tests and observed increases and decreases that paralleled the time course of the strain fields (Fig. 4.1e). The rise in current associated with each ultrasound loading was faster than the reduction in current associated with each cessation of ultrasound loading, causing the current to ratchet upwards over the course of the experiment in synchrony with the change in membrane strain (Fig. 4.2 d).

To establish the connection between mechanosensitive ion channel activity and membrane biomechanics, we quantified the viscoelastic responses of the cells using a generalized Kelvin model with multiple Voigt elements (springs in parallel with dashpots, Fig. A2.1). We fit this model to the viscoelastic creep observed in our experiments both from the application of ultrasound (modeled as a constant load  $\alpha p$ , where  $\alpha$  is a stress concentration factor and  $p$  is the ultrasound pressure) and the cessation of ultrasound, which according to the superposition

principle<sup>131,132</sup> was treated as the addition of an equal and opposite load  $-ap$ . Under a constant load  $ap$ , the creep function  $J(t)$  was expressed using a viscoelastic fading memory model as<sup>131</sup>:

$$J(t) = \frac{\varepsilon(t)}{ap} = \sum_{i=1}^n \frac{1}{E_i} (1 - e^{-t/\tau_i}) \quad (4.1)$$

where the viscoelastic creep time constants  $\tau_i$  and the elastic moduli  $E_i$  are the parameters to be fit for each of the  $n$  Voigt elements, the region  $S$  was defined to encompass the elevated strains in the membrane in the vicinity of the relatively rigid electrodes (Fig. 4.2a), and  $\varepsilon(t)$  is the averaged peak principal strain over  $S$ . We verified that the electrodes do not move measurable in response to the ultrasound loading. Using  $n=3$  time constants provided an excellent fitting to the data (Fig. A2.2), with the model capturing  $\varepsilon(t)$  for all ultrasound pressures (Fig. 4.2a), including the increases in strain during ultrasound loading ( $0 \leq t \leq 1$  s) dominated by  $\tau_1$ , the relaxation in strain following cessation of ultrasound loading, and the hysteresis across multiple loadings, dominated by  $\tau_3$  (Fig. 4.2d). As predicted, increasing the sound pressure increased the peak first principal strain, and cyclic loading resulted in cumulative creep of the membrane (Fig. 4.2d) analogous to that seen in membrane current.

The ratcheting upwards of strain magnitudes from one loading cycle to the next was explored further by performing a finite element simulation of a viscoelastic oocyte loaded by ultrasound while constrained by two rigid electrodes (see Methods for details). The oocyte mechanical properties were identified from experiments. Results (Fig. 4.2h-k) were consistent with experiments (Fig. 4.2b-e), and explained the ratcheting phenomenon in terms of the three Deborah numbers associated with the timescale of loading and the three viscoelastic timescales

(Fig. A2.3a and A2.3b). During the 1 s ultrasound loadings and the interval immediately following cessation of ultrasound loading, deformation arose predominantly from the first branch of the Kelvin model (with the lowest time constant). As this branch became fully relaxed, creep relaxation slowed to a rate dominated by the second and then the third branch (Fig. A2.3b). These latter two branches retained memory of the initial loading over the 2 s resting period between loadings, leading to the cumulative creep ratcheting phenomenon (Fig. A2.3b).

To test the hypothesis that the viscoelastic memory could explain our membrane current observation, we modeled the open probability  $P_o(t)$  of the TRAAK channels using a Boltzmann relationship:

$$P_o(t) = \frac{1}{1 + k(p) \cdot \exp[s(p)J(t)]^m} \quad (4.2)$$

where  $s(p)$  is a pressure-dependent sensitivity factor,  $k(p)$  accounts for the nonlinearity of the membrane, and  $m$  is a fitting constant. The acoustic radiation stress scales as  $p^2/(\rho c^2)$ , where  $\rho$  is the density of the culture medium and  $c$  is the speed of sound in the culture medium. The membrane current increment  $\Delta I$  could then be expressed as

$$\Delta I = \frac{p^2}{(\rho c^2)} P_o(t) t = \frac{p^2}{\rho c^2} \frac{1}{1 + k(p) \cdot \exp[s(p)J(t)]^m} t \quad (4.3)$$

The close fit of this model to experimental data ( $m=0.5$ , Fig. 4.3) supported the hypothesis that cell viscoelasticity is a determinant of mechanosensitive ion channel function.

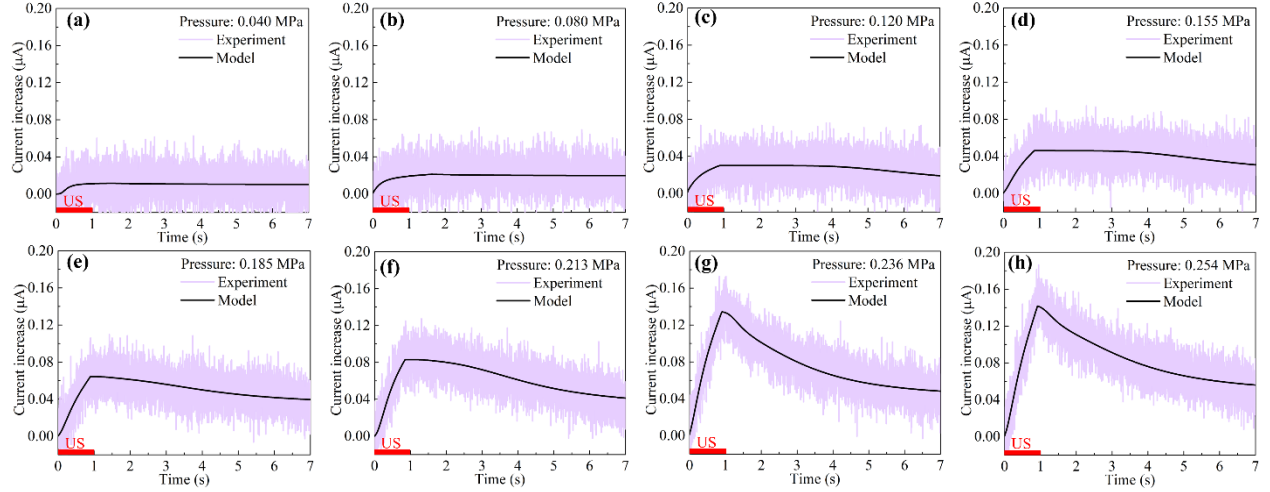


FIG. 4.3 The membrane current change is plotted versus time and fitted curve with Eq. (4.3).

## 4.4 Discussion

Although ultrasound excitation of electrical activity in excitable tissues has been known for many years<sup>22-24</sup>, evidence for ultrasound activation of ion channels and membrane current manipulation is more recent<sup>27</sup>. Since then, many groups designed lots of experiments to study the ultrasound activation on channel activity. Membrane current change has been found for low frequency<sup>34</sup> or high frequency<sup>26</sup> ultrasound, with<sup>31</sup> or without microbubble<sup>25</sup>. Recently, the mechanosensitive TRAAK ion channels activated by ultrasound and recorded by patch clamp showed similar trend with canonical mechanical activation through increased membrane tension<sup>30</sup>. However, the underlying mechanism is still unclear.

Here we reported ultrasound mechanical effect on mechanosensitive TRAAK ion channels activation. We quantitatively studied the oocyte membrane deformation by ultrasound mechanical effect with DDE method, which can map the strain. As far as we know, this has not been reported elsewhere. The membrane current was recorded with two voltage clamp. We found that both the strain and the membrane current showed time dependent process and, thus

predicted that the channel activity should also be affected by the cell mechanical properties. We then used the cyclic load, not only strain curve but also membrane current showed ratcheting phenomenon. We further fitted the current change with the Boltzmann relationship and further showed the relation between the sound pressure, cell mechanics, and channel activation.

The viscoelasticity has been reported to be a key point to affect the cellular behavior<sup>133</sup>. Studies have found that the mechanical factors like the viscoelasticity could affect the fundamental cellular process, including spreading, growth, proliferation, migration, and differentiation. The mechanical microenvironment has been a hot topic during the last several decades. Tissues are always viscoelastic, which means the cells live in such kind of environment. Even though experiments have found those effects, the underlying mechanism might be complicated. Our finding would also provide insights into cell-ECM interactions and bridge the gap between the biomechanics and electrophysiology.

As for the potential application for sonogenetics, it is a challenge to cause large acoustic radiation force inside the tissue or brain with low frequency and low intensity ultrasound since the sound impedance difference between the cell and the ECM is small. The sound impedance can significantly affect the wave propagation<sup>134</sup>, which finally influence the acoustic radiation force<sup>5,128</sup>. Long term activation with ultrasound will also lead to much heat, which might be harmful to the tissue. However, our study may provide new a approach, that is, making full use of the viscoelasticity of both the cell and the ECM and activate the tissue with cyclic loading like pulsed wave, which can avoid heating. Another method might be using some nanoparticles or microbubbles to amplify the acoustic radiation force.



## 4.5 Methods

**Oocyte expression of ion channel proteins.** Complementary RNA (cRNA) was made with the mMessage T7 polymerase kit (Applied Biosystems–Thermo Fisher Scientific). Stage V or VI oocytes were obtained from *Xenopus laevis* by laparotomy based on the protocol approved by Washington University Animal Studies Committee (protocol #20190030). Oocytes were digested by collagenase (0.5 mg/ml, Sigma-Aldrich, St. Louis, MO) and injected with channel cRNA (Drummond Nanoject, Broomall). Each oocyte was injected with K2P cRNA (42 nl). Injected oocytes were incubated in ND96 solution (in mM: 96 NaCl, 2 KCl, 1.8 CaCl<sub>2</sub>, 1 MgCl<sub>2</sub>, 5 HEPES, 2.5 CH<sub>3</sub>COCO<sub>2</sub>Na, 1:100 penicillin streptomycin, pH 7.6) at 18 °C for 2 or 3 days before recording.

**Ultrasound application.** A low frequency (1 MHz) focused ultrasound wave was generated by an immersion ultrasonic transducer focused at 10 mm. A 3D printed chamber was used to position the oocyte in the center of ultrasound focus. The bath of this chamber was filled with ND96, and the recording chamber was located atop a water container that housed the ultrasound transducer. The transducer was submerged in the deionized and degassed water, which can avoid energy dissipation by microbubbles and also matching the sound impedance with the chamber material to reduce wave reflection. The output pressures were measured with a calibrated hydrophone, which performed at the peak spatial pressure. The transducers were driven with a function generator connected to an amplifier. The timing of the ultrasound stimuli was controlled by HEKA Pulse software (HEKA, Germany).

**Two-electrode voltage clamp.** Microelectrodes were made with thin wall borosilicate glass (B150-117-10, Sutter Instrument, Novato, CA) by a micropipette puller (P-97 or P-1000, Sutter

Instrument, Novato, CA). The pipette resistance was 0.5-3 M $\Omega$  when filled with 3 M KCl solution and submerged in ND96 solution. Ionic currents were recorded with two-electrode voltage clamp (TEVC) in ND96 bath solutions at room temperature. Whole-cell currents were recorded with a CA-1B amplifier (Dagan, Minneapolis, MN) driven by Patchmaster (HEKA, Holliston, MA) software. The current recordings were sampled at 1 kHz and low-pass-filtered at 2 kHz.

**Video imaging.** The movie was acquired using Axio Zoom.V16 microscope with Axiocam503 mono at 16 frames per second with a 58 ms exposure time. To get a better video for strain mapping, the Cell Tracker Orange (Thermo Fisher, Waltham, MA) was used to stain the oocyte.

**Strain mapping.** To evaluate the mechanical effect of the ultrasound on the oocyte, we used a strain mapping method called direct deformation (DDE) to calculate the strain field in the membrane <sup>129</sup>. Even though the microscope can only focus on a specific region at the cell membrane, the motion around the electrode is negligible. Meanwhile, there are plenty dots around the black side of the oocyte, which are enough to work as the pattern for DDE method. At the focal plane, the image could be assumed as 2D field. Generally, the video is a set of images. For the DDE method, a warping function was estimated that mapped the images of the video. Briefly, the warping function was designed to provide an estimate of the deformation gradient tensor over defined, overlapping regions within the image volumes. Following Boyle et al., the warping function for each region was optimized with modified Lucas-Kanade algorithm. A video by Axio Zoom. V16 for the oocyte under excitation of ultrasound was used as input to MATLAB code of DDE. To evaluate the strain field at each time point, each frame in the video was utilized during each evaluation. After that, the Green-Lagrange strain tensor was calculated from the deformation gradient estimated for each region. By assembling all the all of the strain region

together, a map of the spatially and timely varying strain field in the cell membrane was obtained. By incorporating the calculation of deformation directly into the warping function, this is a powerful simplification and improves the accuracy of local strain estimates compared with standard cross-correlation techniques. However, this method has the resolution limitation by the feature size in the video that is tracked from image to image. Luckily, the accuracy can be increased by tracking overlapping regions that each include multiple trackable features.

**Finite element simulation.** Finite element simulation for acoustic radiation force and cell deformation in the chamber during our experiments were performed using COMSOL Multiphysics software (COMSOL, Inc., Burlington, MA, USA). For the acoustic radiation force calculation, Because the ultrasound wave field is axisymmetric, the calculation was simplified by taking advantage of axisymmetry. The “Pressure Acoustics” module of COMSOL as adopted to model wave propagation by solving the acoustic wave equation:

$$\nabla \cdot \left( -\frac{\nabla p}{\rho} \right) - \frac{k^2 p}{\rho} = 0 \quad (4.4)$$

where  $p$  is the acoustic pressure,  $\rho$  is the is the density, and  $k$  is the wavenumber defined as  $k = 2\pi f/c$ , with frequency  $f$ , speed of sound  $c$ .

For the ultrasound propagation with frequency of MHz scale, the cell behaves as a liquid like material acoustically since its bulk modulus is much larger than its shear modulus<sup>5,128</sup>. The ultrasound is scattered at the interface between the cell and the extracellular fluid accompanied with momentum flux transfer, which leads to a time-averaged static stress known as acoustic radiation stress:

$$\langle \mathbf{T} \rangle = \frac{1}{2} \text{Re} \left\{ \left[ \frac{p^* p}{2\rho c^2} - \frac{\rho(\mathbf{u}^* \cdot \mathbf{u})}{2} \right] \mathbf{I} + \rho(\mathbf{u}^* \otimes \mathbf{u}) \right\} \quad (4.5)$$

where  $\langle \mathbf{T} \rangle$  is the second-rank acoustic radiation stress tensor,  $\langle \cdot \rangle$  represents the time average,  $\text{Re}(\cdot)$  represents the real part operator,  $\mathbf{u}$  is the particle velocity,  $\mathbf{I}$  is the identity tensor and  $\otimes$  is the dyadic product. The acoustic radiation stress is a kind of field stress and position dependent. The traction stress is the summation of the inside stress and the outside stress as

$$\mathbf{f} = (\mathbf{T}_{\text{in}} - \mathbf{T}_{\text{out}}) \cdot \mathbf{n} \quad (4.6)$$

Where  $\mathbf{T}_{\text{in}}$  and  $\mathbf{T}_{\text{out}}$  are the inside and outside acoustic radiation stress at the interface between the cell and extracellular fluid,  $\mathbf{n}$  is the unit vector with positive value towards the outside on the surface of the cell.

For the cell mechanical simulation, the two electrodes of TEVC will cause a specific boundary condition on the oocyte, which is no longer axisymmetric problem. To this end, the traction stress calculated in cylindrical coordinate should be mapped to 3D Cartesian coordinate system. This was achieved with General Extrusion node in COMSOL. Meanwhile, there is no generalized Kelvin model in COMSOL, thus, we need to write the ordinary differential equations (ODEs) of the constitutive model with the Domain ODEs and DAEs Interface, in which the strains will be coupled into Solid Mechanics Interface. Time-Dependent Solver was used to solve the fully coupled problem.

# **Chapter 5: The mechanics of a sound wave impinging upon a long cylinder, and the prospect of acoustic signal transduction by tomato trichomes**

## **5.1 Abstract**

Acoustic transduction by plants has been proposed as a mechanism to enable just-in-time up-regulation of metabolically expensive defensive compounds. Although the mechanisms by which this “hearing” occurs are unknown, mechanosensation by elongated plant hair cells known as trichomes is suspected. To evaluate this possibility, we developed a theoretical model to evaluate the acoustic radiation force that an elongated cylinder can receive in response to sounds emitted by animals including insect herbivores, and applied it to the long, cylindrical stem trichomes of the tomato plant *Solanum lycopersicum*. Based on perturbation theory and validated by finite element simulations, the model quantifies the effects of viscosity and frequency on this acoustic radiation force. Results suggest that acoustic emissions from certain animals, including insect herbivores, may produce acoustic radiation force sufficient to trigger stretch-activated ion channels.

## **5.2 Introduction**

The evolutionary battle between plants and their insect herbivores has led to a diverse array of sensing abilities in both <sup>35,36,135,136</sup>. For a broad range of plants, hair cells known as trichomes are thought to be mediators of mechanosensing, including sensation of acoustic waves. Although

1950s claims of plants appreciating music were falsified by the 1960s <sup>46</sup>, more recent reports suggest that plants can exhibit transcriptomic, proteomic, and hormonal changes in response to sound <sup>47,48,50-52</sup>. Leaves of *Arabidopsis thaliana* have been reported to prime production of the insect deterrents anthocyanin and glucosinolate in response to recordings of caterpillars of the plant's primary insect herbivore <sup>44</sup>.

Although there is no consensus on how plants transduce sound <sup>53</sup>, mechanisms identified for mechanosensation at the cellular level in plants include stretch-activated ion channels and plasmodesmata-based interactions between the cytoskeleton, plasma membrane, and cell wall <sup>54,137</sup>. Trichomes can work as active mechanosensory switches, with mechanical stimulus eliciting  $\text{Ca}^{2+}$  oscillations of the trichome and pH shifts in surrounding cells <sup>42</sup>. Mechanical stimulation of trichomes is posited to induce secretion of defensive materials in *Solanum lycopersicum* <sup>138</sup>. We therefore explored the possibility that trichomes might also serve to convert the acoustic radiation force of an insect into strain.

Although the mechanics of interactions between the cell wall and the plasma membrane are not fully understood, evidence exists of proteins such as cellulose synthases that connect the plasma membrane to the cell wall over periods of time on the time scale of cell wall development <sup>139</sup>, which are long compared to typical acoustic emissions on the time scale of seconds. The membrane also adheres to the wall at cell-cell connections known as plasmodesmata <sup>140,141</sup>. The membrane does have a fluid character to it, with viscoelastic stress relaxation occurring over timescales on the order of seconds in vesicles and neutrophils <sup>142,143</sup> to minutes in mammalian outer hair cells <sup>144</sup>. Therefore, for acoustic emissions on the order of seconds, strain of the cell wall can likely be transmitted to the plasma membrane. The mechanical fields necessary to open

mechanosensitive ion channels in the plasma membrane are often thought of in terms of a stress per unit membrane length acting on a membrane with an area modulus per unit membrane length that varies only weakly with membrane thickness <sup>145</sup>. As described in our results, we estimate these strains to be sufficient to open stretch-activated ion channels under certain conditions.

Acoustic radiation force, the period-averaged force caused by a sound wave, is analogous to the radiation force generated by electromagnetic waves striking on electrically or magnetically responsive objects <sup>74</sup>. Acoustic radiation force can be used in engineering to manipulate small particles, droplets, cells, and organisms <sup>5,100,103,104</sup>. Although a large literature addresses the related problems of calculating the sonar cross-section of submerged shapes and of guessing a shape from backscattered sonar, the literature for acoustic radiation force estimation is more limited <sup>146,147</sup>. The first relevant solution <sup>95</sup> is an expression for the acoustic radiation force generated on a rigid spherical particle in an inviscid fluid, specialized to the case of particles having a radius much smaller than wavelength. The extension of this to the case of compressible spheres was first achieved using a near-field approach <sup>114</sup>, and then using a far-field approach by Mitri and Fellah <sup>148</sup>, who obtained a simpler mathematical form.

Our focus was computing the effect of acoustic radiation force on trichomes such as those of cultivated tomato plants, *Solanum lycopersicum*, and assessing whether these forces could strain trichomes sufficiently to activate mechanosensitive (or mechano-responsive) ion channels. The trichomes of *S. lycopersicum* present on the leaves and stems in six different phenotypes, both glandular and non-glandular, all of which are long, slender, and nominally cylindrical (<sup>149,150</sup>, and Fig. 5.1). Although the acoustic radiation force on a cylinder in an inviscid medium is known <sup>58</sup>, the inviscid solution is valid only for a viscous penetration depth,  $\delta_p$ , that is small compared to

the radius  $r \sim 20 \mu\text{m}$  of the trichome. This is not the case for a trichome in air: the viscous penetration depth scales as  $\delta_p = \sqrt{\mu_{air}/(\rho_{air}\pi f)}$ , where the kinematic viscosity ( $\mu_{air}/\rho_{air}$ ) is  $1.6 \text{ m}^2/\text{s}$  at standard temperature and pressure, and  $f$  is frequency in Hertz. Thus,  $\delta_p$  is on the order of  $700/\sqrt{f} \mu\text{m}$  in the air, with  $\delta_p$  significant compared to  $r$  throughout the human audible range, especially for lower frequencies (e.g.,  $\delta_p = 7 \mu\text{m}$  for  $f = 10000 \text{ Hz}$ ). Thus, the full viscous solution is required to analyze this problem.

To derive this solution, we applied a second-order perturbation theory to the continuity and Navier-Stokes equations for an acoustic field to calculate the scattering coefficients. We next computed the acoustic radiation force according to the far-field approach and introduced an acoustic radiation force function<sup>151,152</sup>. Finally, we examined the theoretical model predictions to predict the acoustic radiation force and peak stress that a cantilevered trichome would experience when subjected to acoustic stress from a range of animals.

## 5.3 Materials and methods

### 5.3.1 Imaging of tomato trichomes

Tomato plants of the species *Solanum lycopersicum* were grown at room temperature in a greenhouse for 50 days, watered daily. Plant stems were severed with a razor blade and imaged using an Axio Zoom.V16 microscope at 10x magnification within 5 minutes to reveal the structure and aspect ratios of stem trichomes (Fig. 5.1).



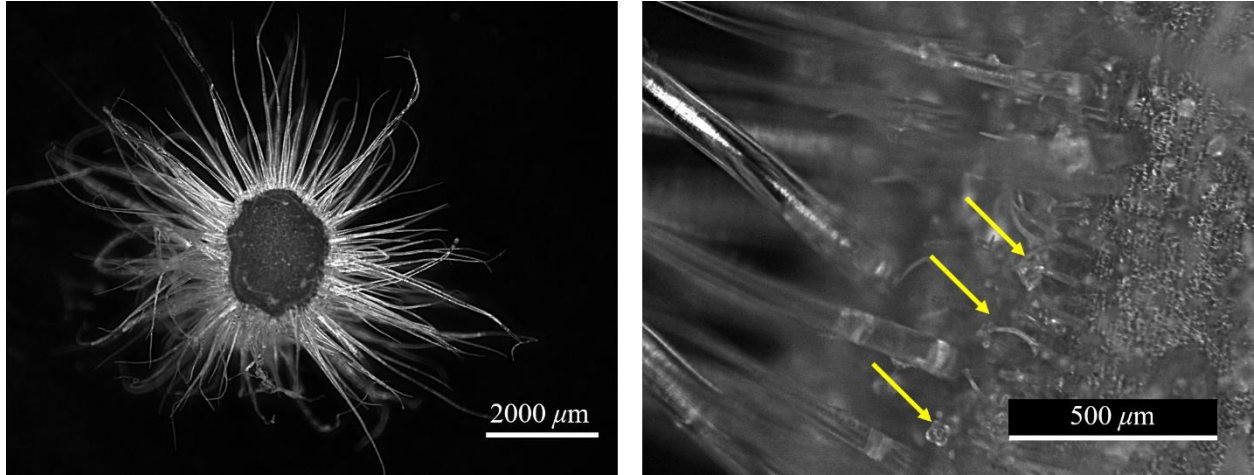


FIG. 5.1 (a) Trichomes on the stem of *S. lyopersicum*, showing non-glandular trichomes. (b) Much shorter glandular trichomes (e.g., as denoted by the arrow) were not considered in the analysis.

### 5.3.2 Mechanical and acoustical properties of trichomes

Parameters chosen for theoretical analysis and finite-element simulation are listed in Table 5.1.

For the cytosol and cell wall, reported properties vary and we therefore chose representative values as baseline values. The compressible liquid cytosol was assigned bulk modulus

$\kappa_{cyto} = 2.15$  GPa and density  $\rho_{cyto} = 1000$  kg/m<sup>3</sup> for a compressional wave velocity of

$c_{cyto} = \sqrt{\kappa_{cyto}/\rho_{cyto}} = 1470$  m/s. The sound impedance used for air was  $Z_{air} = \rho_{air}c_{air} =$

410 Rayl, far smaller than the sound impedance for the cytoplasm ( $Z_{cyto} = \rho_{cyto}c_{cyto} = 1.47 \times$

$10^6$  Rayl). As a result, the trichome can be treated as rigid bodies acoustically. Meanwhile, the

density of both the cell wall and cytosol are almost 1000 times that counterpart of air, and as a

consequence the trichome can not vibrate under the influence of sound wave and acts like an

immovable cylinder. Although solutions for the vibration of fluid-filled pipes and the effects of

elastic boundary conditions are well known<sup>153-157</sup>, these are not needed for the current analysis.

*Table 5.1 Mechanical properties ranges studied for model trichomes* <sup>45</sup>

<b>Symbol</b>	<b>Variable</b>	<b>Range of data</b>	<b>Baseline value</b>
$\rho_{wall}$	Density of cell wall	100-3000 kg/m <sup>3</sup> <sup>158</sup>	1000 kg/m <sup>3</sup>
$\rho_{cyto}$	Density of cytosol	1000 kg/m <sup>3</sup> <sup>45,158</sup>	1000 kg/m <sup>3</sup>
$E_{wall}$	Young's modulus of cell wall	0.3-3.28 MPa	0.3 MPa
$\nu$	Poisson's ratio of cell wall	0.3-0.49 <sup>159</sup>	0.33
$\kappa_{cyto}$	Bulk modulus of cytosol	2.15 GPa <sup>160</sup>	2.15 GPa
$K_a$	Elastic area compressibility modulus	179-560 mN/m <sup>161,162</sup>	500 mN/m

Table 5.2 Acoustic properties of air <sup>163</sup>

Symbol	Variable	Baseline value
$\rho_{air}$	Density of air	1.18 kg/m <sup>3</sup>
$c_{air}$	Speed of sound in air	346 m/s
$Z_{air}$	Impedance of air	410 Rayl
$\mu_{air}$	Shear viscosity	$1.79 \times 10^{-6}$ Pa

### 5.3.3 Theoretical model

To calculate the stress field inside the trichome, we first solved for the acoustic radiation force. Treating the trichome as a rigid cylinder acoustically, we studied an infinitely long rigid cylinder immersed in a viscous fluid. In the absence of an incident wave, the governing equations for the fluid are the continuity and the Navier-Stokes equations:

$$\frac{\partial \rho}{\partial t} + \nabla \cdot (\rho \mathbf{u}) = 0 \quad (5.1)$$

$$\rho \frac{\partial \mathbf{u}}{\partial t} = -\nabla p - \rho(\mathbf{u} \cdot \nabla) \mathbf{u} + \mu \nabla^2 \mathbf{u} + \left( \mu_b + \frac{1}{3} \mu \right) \nabla(\nabla \cdot \mathbf{u}) \quad (5.2)$$

where  $\rho$ ,  $\mathbf{u}$ ,  $p$ ,  $\mu$  and  $\mu_b$  are the density field, velocity field, pressure field, shear viscosity and bulk viscosity of the host fluid, respectively. Thermal effects are neglected because the thermal diffusion length in the fluid is much smaller than momentum diffusion length. The flow can thus be treated as adiabatic so that the pressure depends only on density:

$$p = p(\rho) \quad (5.3)$$

When an incident acoustic wave starts to travel in the fluid medium, the fluid will be perturbed, and the fluid properties may be expressed using perturbation theory as:

$$\begin{aligned} \rho &= \rho_0 + \rho_1 + \rho_2 + \dots \\ p &= p_0 + p_1 + p_2 + \dots \\ \mathbf{u} &= \mathbf{0} + \mathbf{u}_1 + \mathbf{u}_2 + \dots \end{aligned} \quad (5.4)$$

where the subscripts 0, 1 and 2 denote the base quantity, first-order and second-order perturbation quantities, respectively. The base quantities represent the undisturbed properties of the fluid. The incident wave is responsible for the first-order quantities, which, for density and pressure, are small compared to the undisturbed quantities. The incident acoustic wave is a first-order quantity, harmonic in time with angular frequency  $\omega$ , which generates a zero-net force over a period.

Interaction between the incoming and scattered waves generates the second-order quantities, which are responsible for the acoustic radiation force of concern. The second-order quantities will not zero out on time averaging. Consequently, the goal is to solve for the time-averaged second-order terms. Because the time-averaged second-order quantities can be written in terms of the first-order quantities under certain limiting conditions, it is necessary to solve the linearized Navier-Stokes equations. Substituting Eq. (5.4) into Eqs. (5.1) and (5.2) yields:

$$\frac{\partial \rho_1}{\partial t} + \rho_0 \nabla \cdot \mathbf{u}_1 = 0 \quad (5.5)$$

and

$$\rho_0 \frac{\partial \mathbf{u}_1}{\partial t} = -\nabla p_1 + \mu \nabla^2 \mathbf{u}_1 + \left( \mu_b + \frac{1}{3} \mu \right) \nabla (\nabla \cdot \mathbf{u}_1) \quad (5.6)$$

Under the assumption of adiabatic conditions, the equation of state is  $p(\rho) = p_0 + (\partial p / \partial \rho)_s \rho_1$ .

The derivative is related to the speed of sound by  $(\partial p / \partial \rho)_s = c_0^2$ . Therefore, we obtain the relation between the first-order pressure and the density as <sup>152,164</sup>:

$$p_1 = c_0^2 \rho_1 \quad (5.7)$$

For a viscous fluid, based on the Helmholtz decomposition theorem, the first-order field can be written as the summation of an acoustic component and a vortical component, as:

$$\langle w_1 \rangle = \langle w_{1A} \rangle + \langle w_{1V} \rangle \quad (5.8)$$

where  $w_1$  represents the first-order flow variable, and the subscripts  $A$  and  $V$  represent the acoustic and vortical parts, respectively, so that  $\nabla \times \mathbf{u}_{1A} = 0$  and  $\nabla \cdot \mathbf{u}_{1V} = 0$ . The angular brackets denote the quantity averaged over one oscillation period,  $T$ , defined as:

$$\langle g \rangle = \frac{1}{T} \int_0^T g(t) dt \quad (5.9)$$

We derive the second-order time-averaging equations in a similar fashion by incorporating Eq. (5.4) into Eqs. (5.1) and (5.2):

$$\frac{\partial \rho_2}{\partial t} + \rho_0 \nabla \cdot \mathbf{u}_2 + \nabla \cdot (\rho_1 \mathbf{u}_1) = 0 \quad (5.10)$$

$$\rho_0 \frac{\partial \mathbf{u}_2}{\partial t} + \rho_1 \frac{\partial \mathbf{u}_1}{\partial t} + \rho_0 (\mathbf{u}_1 \cdot \nabla) \mathbf{u}_1 = -\nabla p_2 + \mu \nabla^2 \mathbf{u}_2 + \left( \mu_b + \frac{1}{3} \mu \right) \nabla (\nabla \cdot \mathbf{u}_2) \quad (5.11)$$

By time-averaging both sides of Eqs. (5.10) and (5.11), the time-dependent second-order terms

on the left hand side disappear <sup>165</sup>. Rearranging the remaining terms leads to:

$$\rho_0 \nabla \cdot \langle \mathbf{u}_2 \rangle = -\nabla \cdot \langle \rho_1 \mathbf{u}_1 \rangle \quad (5.12)$$

$$-\nabla \langle p_2 \rangle + \mu \nabla^2 \langle \mathbf{u}_2 \rangle + \left( \mu_b + \frac{1}{3} \mu \right) \nabla (\nabla \cdot \langle \mathbf{u}_2 \rangle) = \left\langle \rho_1 \frac{\partial \mathbf{u}_1}{\partial t} \right\rangle + \rho_0 \langle (\mathbf{u}_1 \cdot \nabla) \mathbf{u}_1 \rangle \quad (5.13)$$

The second-order flow field can also be separated into acoustic and vortical parts. Linearity of the above equations yields:  $\mathbf{u}_2 = \mathbf{u}_{2a} + \mathbf{u}_{2v}$  and  $p_2 = p_{2a} + p_{2v}$ . Incorporating these into Eqs. (5.12) and (5.13) and collecting terms involving subscripts 1A and 2a, we arrive at:

$$\rho_0 \nabla \cdot \langle \mathbf{u}_{2a} \rangle = -\nabla \cdot \langle \rho_{1A} \mathbf{u}_{1A} \rangle \quad (5.14)$$

and

$$-\nabla \langle p_{2a} \rangle + \mu \nabla^2 \langle \mathbf{u}_{2a} \rangle + \left( \mu_b + \frac{1}{3} \mu \right) \nabla (\nabla \cdot \langle \mathbf{u}_{2a} \rangle) = \left\langle \rho_1 \frac{\partial \mathbf{u}_{1A}}{\partial t} \right\rangle + \rho_0 \langle \mathbf{u}_{1A} \cdot \nabla \mathbf{u}_{1A} \rangle \quad (5.15)$$

The acoustic radiation force is computed by integrating the stress tensor momentum equation over a surface located in the inviscid bulk, provided it encloses the scatter <sup>152</sup>. In the inviscid far field, the flow field is potential flow. We thus set  $\mu = \mu_b = 0$  in Eq. (5.15) to obtain:

$$-\nabla \langle p_{2A} \rangle = \left\langle \rho_1 \frac{\partial \mathbf{u}_{1A}}{\partial t} \right\rangle + \rho_0 \langle \mathbf{u}_{1A} \cdot \nabla \mathbf{u}_{1A} \rangle \quad (5.16)$$

As the second-order terms can be derived from Eqs. (5.14) and (5.16) expressed in terms of the first-order quantities, we next solve for the first-order perturbations.

Note that substituting Eqs. (5.12) and (5.13) into Eqs. (5.14) and (5.15) yields expressions for  $\langle p_{2v} \rangle$  and  $\langle \mathbf{u}_{2v} \rangle$ . These expressions involve vortical terms and hence will account for external

acoustic streaming, which is dependent upon boundary conditions. This will be dealt with below.

### 5.3.4 First-order equations of the acoustic wave field

For a rigid cylinder immersed in a viscous compressible fluid (Fig. 5.1 a), the first-order velocity with Helmholtz decompositions can be expressed in terms of a scalar potential  $\phi$  and a vector potential  $\psi$ , as <sup>166,167</sup>:

$$\mathbf{u}_1 = \nabla\phi + \nabla \times \psi \quad (5.17)$$

where  $\phi$  consists of an incident potential  $\phi_{in}$  and a scattering potential  $\phi_{sc}$ . We assume the axis of the cylinder to be perpendicular to the wave vector of incident plane wave. In addition, we assume the cylinder to be infinite to exclude end effects in theoretical derivation. A cylindrical coordinate system with unit vectors  $(\mathbf{e}_r, \mathbf{e}_\theta, \mathbf{e}_z)$  is built into the instantaneous axis of the cylinder (Fig. 5.1 b). The incident velocity potential can thence be expressed in a cylindrical partial-wave series with respect to the system, as:

$$\phi_{in} = \phi_0 \sum_{n=0}^{\infty} \varepsilon_n i^n J_n(k_c r) \cos n \theta e^{-i\omega t} \quad (5.18)$$

where  $\phi_0$  is the amplitude of velocity potential field,  $\varepsilon_n$  is the Neumann factor (defined as  $\varepsilon_0 = 1$  and  $\varepsilon_j = 2, j = 1, 2, \dots, n$ ),  $J_n(\cdot)$  is the  $n$ th Bessel function of the first kind, and  $k_c$  represents the wave number of the incident wave given by:

$$k_c = \frac{\omega}{c_0} \left[ 1 - \frac{i\omega}{\rho_0 c_0^2} \left( \mu_b + \frac{4}{3} \mu \right) \right]^{-1/2} \quad (5.19)$$

In the same manner, the scattered wave potential can be expressed as:

$$\phi_{sc} = \phi_0 \sum_{n=0}^{\infty} \varepsilon_n i^n B_n H_n(k_c r) \cos n \theta e^{-i\omega t} \quad (5.20)$$

where  $H_n(\cdot)$  is the Hankel function of the first kind of order  $n$ . Since we assume the cylinder is perpendicular to the wave vectors, the vector potential can be reduced to  $\boldsymbol{\Psi} = \psi \mathbf{e}_z$ , in which the scalar potential  $\psi$  satisfies:

$$\nabla^2 \psi + k_v^2 \psi = 0 \quad (5.21)$$

Here,  $k_v = (1 + i)/\delta$ ,  $\delta = \sqrt{2\nu/\omega}$ ,  $\nu = \mu/\rho_0$ ,  $\nu$  is the kinematic viscosity of fluid, and  $\delta$  is the momentum boundary layer thickness. The solution of Eq. (5.21) is given by:

$$\psi = \phi_0 \sum_{n=0}^{\infty} \varepsilon_n i^n C_n H_n(k_s r) \sin n \theta e^{-i\omega t} \quad (5.22)$$

where  $B_n$  and  $C_n$  are the scattering coefficients, to be determined using boundary conditions on the cylinder surface.

### 5.3.5 Calculation of scattering coefficients

The first-order velocity of the rigid cylinder is determined by the instantaneous force caused by hydrodynamic stress. To evaluate the first-order velocity, we integrated the stress on cylinder surface, as:

$$F = \int_0^{2\pi} (\sigma_{rr} \cos \theta - \sigma_{r\theta} \sin \theta)|_{r=R} R d\theta \quad (5.23)$$

where the hydrodynamic stress components of the fluid in cylindrical coordinates are:



$$\sigma_{rr} = i\omega\rho\phi - 2\mu k_c^2\phi - 2\mu\frac{\partial^2\phi}{\partial r^2} + 2\mu\frac{\partial}{\partial r}\left(\frac{1}{r}\frac{\partial\psi_s}{\partial\theta}\right) \quad (5.24)$$

$$\sigma_{r\theta} = \mu\left[-\frac{1}{r}\frac{\partial^2\phi}{\partial\theta\partial r} - \frac{\partial}{\partial r}\left(\frac{1}{r}\frac{\partial\phi}{\partial\theta}\right) + \frac{1}{r^2}\frac{\partial\phi}{\partial\theta} + \frac{1}{r^2}\frac{\partial\psi}{\partial\theta^2} - \frac{\partial^2\psi}{\partial r^2} + \frac{1}{r}\frac{\partial\psi}{\partial r}\right]$$

Substituting Eq. (5.24) into Eq. (5.23) yields:

$$F = \frac{2\pi\mu\phi_0 i}{r}[D(r) + B_1E(r) + C_1G(r)]A_1e^{-i\omega t} \quad (5.25)$$

where  $D(r) = [2(k_c r)^2 - (k_s r)^2/2]J_1(k_c r)$ ,  $E(r) = [2(k_c r)^2 - (k_s r)^2/2]H_1(k_c r)$ ,  $G(r) = (k_s r)^2/2H_1(k_s r)$ . Due to orthogonality, only the  $n = 1$  term survives in Eq. (5.25). In the presence of the instantaneous force, the acceleration of the cylinder can be obtained with Newton's second law:

$$F_1 = \rho_b V_b \frac{dU}{dt} \quad (5.26)$$

where  $\rho_b$  is the density of cylinder,  $V_b$  is volume of cylinder per unit length, and  $U$  is the first-order particle velocity along the axial direction. Upon substituting Eq. (5.25) into Eq. (5.26) and integrating the equation with respect to time, the velocity is obtained as:

$$U = -\frac{2\phi_0 i}{r^3 \rho' k_s} A_1 [D(r) + B_1 E(r) + C_1 G(r)] e^{-i\omega t} \quad (5.27)$$

where  $\rho' = \rho_b/\rho_0$  is the density ratio of the cylinder to the fluid.

From Eq. (5.17), the radial and circumferential velocity components of the surrounding fluid at  $r = R$  are then given by:

$$u_r = \frac{\varphi_0}{r} \sum_{n=0}^{\infty} \varepsilon_n i^n \cos n \theta [d_n(r) + e_n(r)B_n + g_n(r)C_n] A_n e^{-i\omega t} \quad (5.28)$$

$$u_\theta = \frac{\varphi_0}{r} \sum_{n=0}^{\infty} \varepsilon_n i^n \sin n \theta [k_n(r) + m_n(r)B_n + n_n(r)C_n] A_n e^{-i\omega t} \quad (5.29)$$

where  $d_n(r) = (k_c r)J_{n-1}(k_c r) - nJ_n(k_c r)$ ,  $e_n(r) = (k_c r)H_{n-1}(k_c r) - nH_n(k_c r)$ ,  $g_n(r) = nH_n(k_s r)$ ,  $k_n(r) = -nJ_n(k_c r)$ ,  $m_n(r) = -nH_n(k_c r)$  and  $n_n(r) = -k_s r H_{n-1}(k_s r) + nH_n(k_s r)$ . The scattering coefficients are calculated based on continuity boundary conditions at the cylinder-fluid interface:

$$u_r = U \cos \theta \quad (5.30)$$

$$u_\theta = -U \sin \theta \quad (5.31)$$

Substituting Eqs. (5.27)-(5.29) into Eqs. (5.30) and (5.31), we obtain the scattering coefficients ( $B_n, C_n$ ) for each value of  $n$ . The closed form expressions for these were entered into a Matlab script for evaluation. With these scattering coefficients determined, all first-order quantities in the fluid can be calculated directly.

### 5.3.6 Calculation of acoustic radiation force

The acoustic radiation force per unit length is calculated by integrating the time-averaged acoustic radiation stress tensor on the cylinder surface, as:

$$\langle \mathbf{F}_{rad} \rangle = \left\langle \int_{S_t} \boldsymbol{\sigma} \cdot \mathbf{n} dS \right\rangle \quad (5.32)$$

where  $S_t$  is the cylinder surface at time  $t$  and  $\mathbf{n}$  represents the unit vector normal to the surface  $S_0$  of the cylinder, pointing outward. It has been established that:

$$\langle \mathbf{F}_{rad} \rangle = \left\langle \int_{S_t} \boldsymbol{\sigma} \cdot \mathbf{n} dS \right\rangle = \left\langle \int_{S_{far-field}} (\boldsymbol{\sigma} - \rho_0 \mathbf{u} \otimes \mathbf{u}) \cdot \mathbf{n} dS \right\rangle \quad (5.33)$$

where  $S_{far-field}$  is any surface enclosing the cylinder. In an ideal fluid, the acoustic radiation force as given by Eq. (5.33) is the same as that calculated by Mitri. However, in the present study, the fluid is viscous and hence part of the momentum is spent in generating acoustic streaming flow near cylinder surface<sup>168</sup>. Following Settnes and Bruus<sup>169</sup>, we expressed the acoustic radiation force acting on the cylinder using the far-field approach:

$$\langle \mathbf{F}_{rad} \rangle = \int_{S_{far-field}} \left[ \frac{1}{2} \rho_0 \langle \mathbf{u}_{1A}^2 \rangle - \frac{1}{2 \rho_0 c_0^2} \langle p_{1A}^2 \rangle - \rho_0 \langle \mathbf{u}_{1A} \cdot \mathbf{u}_{1A} \rangle \right] d\mathbf{S}_{far-field} \quad (5.34)$$

Note that only first-order quantities appear in this expression. Although the force is integrated in the far field, the effect of fluid viscosity is built into the scattering coefficients  $B_n$  and  $C_n$ . In most practical applications, the imaginary part of the wavenumber  $k_c$  is tiny (*i.e.*,  $\omega \nu / c_0^2 \ll 1$ ), which means the decaying part of  $k_c$  is negligible. It suffices thence to assume that  $k_c \rightarrow k_0$ ,  $k_0$  being the real part of  $k_c$ . We proceed next with the far-field approach<sup>151</sup>. In the far-field region, the Hankel function reduces to exponential function, as:

$$i^n H_n(k_0 r) \rightarrow \sqrt{\frac{2}{\pi k_0 r}} e^{i(k_0 r - \pi/4)} \quad (5.35)$$

As a result, the scattered velocity potential can be expressed as:

$$\phi_{sc} = \frac{f(\theta)}{\sqrt{k_0 r}} e^{ik_0 r} e^{-i\omega t} \quad (5.36)$$

where

$$f(\theta) = \sqrt{\frac{2}{\pi}} e^{-i\pi/4} \sum_{n=0}^{\infty} A_n \varepsilon_n \cos(n\theta) \quad (5.37)$$

Incorporating this new definition of the scattered and incident wave potentials into Eq. (5.34), the force per unit length acting on the cylinder along the direction of wave propagation is obtained following straightforward manipulations as:

$$\begin{aligned} \langle F_{rad} \rangle = & -\frac{\rho_0 k_0}{2} \int_0^{2\pi} f(\theta) f^*(\theta) \cos \theta \, d\theta - \frac{\rho_0 r k_0^2}{2} \int_0^{2\pi} \operatorname{Re} \left( \tilde{\phi}_i^* \frac{f(\theta) e^{ik_0 r}}{\sqrt{k_0 r}} \right) \cos \theta \, d\theta \\ & + \frac{\rho_0 r k_0}{2} \int_0^{2\pi} \operatorname{Im} \left( \frac{\partial \tilde{\phi}_i^*}{\partial z} \frac{f(\theta) e^{ik_0 r}}{\sqrt{k_0 r}} \right) d\theta \end{aligned} \quad (5.38)$$

where  $\tilde{\phi}_i = \phi_i e^{i\omega t}$ ,  $\operatorname{Re}$  and  $\operatorname{Im}$  represent the real and imaginary parts, respectively, and the superscript “\*” represents the complex conjugate. Equation (5.38) can be used to evaluate the acoustic radiation force for any incoming wave.

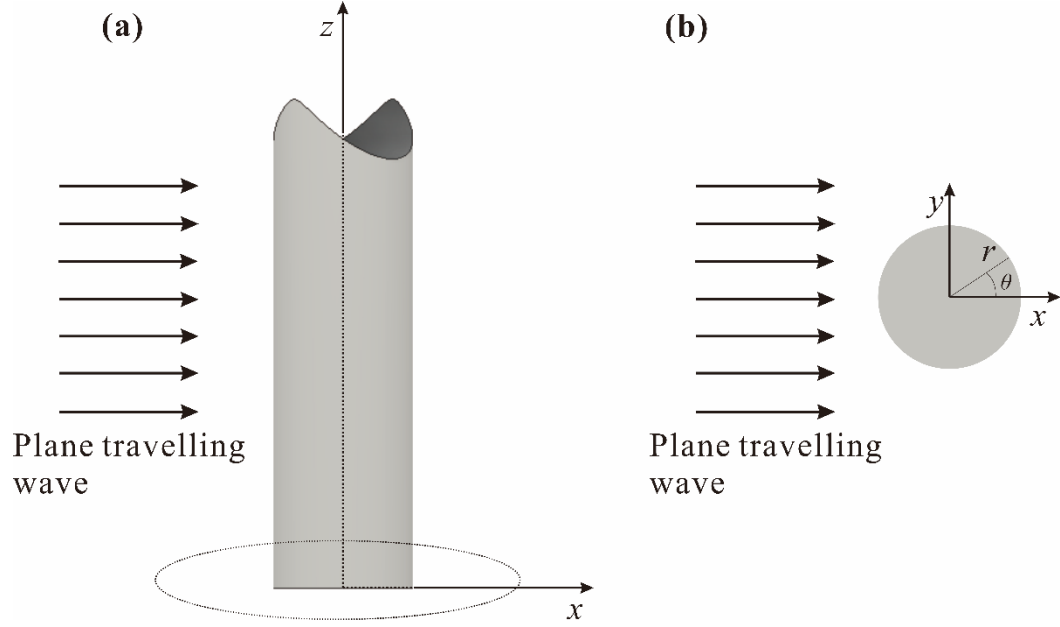


FIG. 5.2. Side view (a) and top view (b) of schematic of a circular and infinitely long rigid cylinder, which is immersed in viscous fluid and impinged by plane travelling waves.

For the case of a plane travelling incident wave, substituting (18) and (37) into (38) using the following relations:

$$\int_0^{2\pi} \cos(n\theta) \cos(m\theta) \cos \theta d\theta = \begin{cases} \pi & (n + m = 1) \\ \frac{\pi}{2} & (n - m = \pm 1, n \neq 0, m \neq 0) \\ 0 & (\text{otherwise}) \end{cases} \quad (5.39)$$

$$\int_0^{2\pi} \cos(n\theta) \cos \theta d\theta = \begin{cases} \pi & (n = 1) \\ 0 & (\text{otherwise}) \end{cases} \quad (5.40)$$

we obtain the radiation force per unit length of cylinder as:

$$\langle F_{rad} \rangle_{tr} = Y_{tr} S_c \langle E_p \rangle \quad (5.41)$$

Here, the subscript  $tr$  represents traveling wave,  $\langle E_p \rangle = \frac{1}{2} \rho_0 k_0^2 |\varphi_0|^2 = p_0^2 / (2\rho_0 c_0^2)$  is the time-averaged energy density,  $S_c = 2R$  is the cross-sectional width of the unit length cylinder, and  $Y_{tr}$  is the “radiation force function,” given by:

$$Y_{tr} = -\frac{2}{kR} \sum_{n=0}^{\infty} [\varepsilon_n \alpha_n + 2(\alpha_n \alpha_{n+1} + \beta_n \beta_{n+1})] \quad (5.42)$$

in which  $\alpha_n$  and  $\beta_n$  are the real and imaginary parts of  $B_n$ , respectively.

### 5.3.7 Normal stresses in a trichome

The trichomes of interest are slender, with length tens or hundreds times the radius. Therefore, the trichome can be treated as a cantilevered Euler-Bernoulli beam, and the largest normal stress in the cell wall is:

$$\sigma_{max} = \frac{M_{max} R}{I_{rr}} \quad (5.43)$$

where the  $M_{max}$  is the moment generated by the acoustic radiation force and  $I_{rr} = \pi[R^4 - (R - t_{wall})^4]/4$  is the second moment of the cross-sectional area about the neutral axis with  $R$  being the radius of the trichome and  $t_{wall}$  being the thickness of the wall of the trichome. For the case studied, the acoustic radiation force is uniformly distributed along the trichome so that the largest moment occurs at the base and:

$$\sigma_{max} = \frac{2(RL)^4}{\pi[R^4 - (R - t_{wall})^4]} \frac{p^2}{\rho_{air} c_{air}^2} Y_{tr} \quad (5.44)$$

From this, the tension in the cell membrane could be estimated by considering a cell membrane and cell wall in parallel <sup>170</sup>:

$$T_{max} = \frac{K_a(1 - \nu)}{E_{wall}} \frac{2(RL)^4}{\pi[R^4 - (R - t_{wall})^4]} \frac{p^2}{\rho_{air}c_{air}^2} Y_{tr} \quad (5.45)$$

where  $K_a$  is the elastic area compressibility modulus of the membrane, and the fact that  $E_{wall}t_{wall} \gg K_a$  has been invoked.

### 5.3.8 Finite element simulations

To validate the analytical results, two-dimensional finite element (FE) simulations were carried out with COMSOL Multiphysics (COMSOL AB, Stockholm, Sweden). The geometry used had an axis of symmetry on its left-hand boundary (Figure 5.3). The rigid cylinder was represented by a semi-circular domain, and the surrounding fluid medium by a larger semi-circular domain. A “perfect matched layer” (PML) that absorbs the majority of the acoustic energy incident upon the boundary from the cylinder was applied on the outer boundary of the domain.

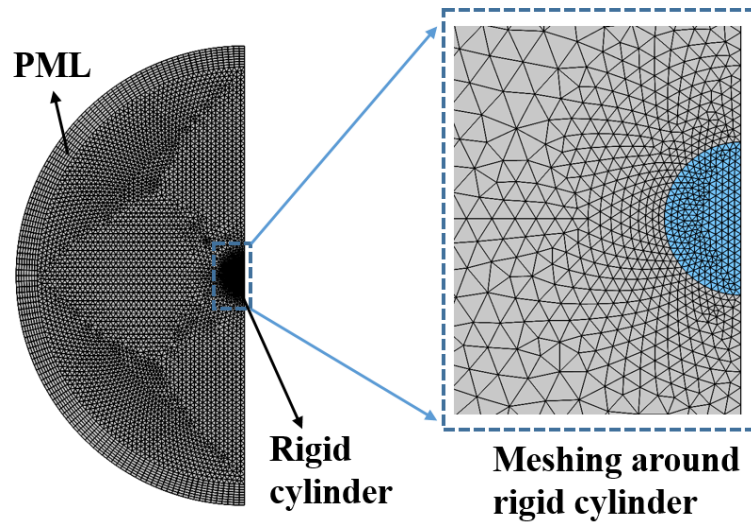


*FIG. 5.3. Finite element model for validating acoustic radiation force on a rigid cylinder in viscous fluid. Perfect matched layer is marked as PML.*

To begin with, an inviscid model is developed to solve the ideal fluid medium problem, for two purposes. First, relative to the viscous case, the inviscid case requires less calculation time<sup>151</sup>. Second, results calculated with the inviscid model can be used to validate subsequent simulations carried out to quantify the viscous effects.

In the inviscid case, the acoustic radiation stress and the total force acting on the rigid cylinder are associated only with the first-order acoustic fields. Similar to the far field, which is considered inviscid, the acoustic radiation force acting on the cylinder is expressed as:

$$\langle \mathbf{F}_{rad} \rangle = \int_{S_0} \left[ \frac{1}{2} \rho_0 \langle \mathbf{u}_{1A}^2 \rangle - \frac{1}{2\rho_0 c_0^2} \langle \mathbf{p}_{1A}^2 \rangle - \rho_0 \langle \mathbf{u}_{1A} \cdot \mathbf{u}_{1A} \rangle \right] d\mathbf{S}_0 \quad (5.46)$$

where  $S_0$  is the cylinder surface at rest. The COMSOL “Acoustic-Solid Interaction” physics module is employed to obtain the first-order acoustic fields. To model the cylinder-fluid interaction, a predefined “acoustic-structure boundary” is applied on the surface of the cylinder. The incident wave is modeled with a “background field” function.

Next, we study viscosity effects in the range of interest. With the harmonic acoustic part in Eq. (5.33) discarded, the total force is:

$$\langle \mathbf{F}_{rad} \rangle = \int_{S_0} \langle \boldsymbol{\sigma}_2 - \rho_0 \mathbf{u}_1 \otimes \mathbf{u}_1 \rangle \cdot \mathbf{n} dS_0 \quad (5.47)$$

with



$$\boldsymbol{\sigma}_2 = -p_2 \mathbf{I} + \mu(\nabla \mathbf{u}_2 + (\nabla \mathbf{u}_2)^T) + \left(\mu_b - \frac{2}{3}\mu\right)(\nabla \cdot \mathbf{u}_2) \quad (5.48)$$

In an inviscid fluid, the second-order stress  $\langle \boldsymbol{\sigma}_2 \rangle$  is expressed only in terms of the first-order acoustic fields. In a viscous fluid, however, this is not true due to the appearance of acoustic streaming. To find  $\langle \boldsymbol{\sigma}_2 \rangle$  in a viscous fluid, the second-order equations (5.12) and (5.13) must be solved. To this end, the sequential procedures detailed below are adopted:

- (1) To calculate the first-order acoustic wave fields of the cylinder-fluid system, the “Thermoviscous Acoustic-Solid” module of COMSOL is employed, with the Thermoviscous Acoustic-Solid Boundary applied on the surface of the rigid cylinder. Similar to the inviscid case, the incident wave is modeled with a background field.
- (2) The second-order flow field is calculated by using the modified “Laminar Flow” module. The mass source on the right-hand side of Eq. (5.12) is added onto a “Weak Contribution” node having the weak expression of  $-0.5\nabla \cdot (\rho_1 \mathbf{u}_1) \cdot \tilde{p}_2$  ( $\tilde{p}_2$  being the pressure test function), while the body force term on the right-hand side of Eq. (5.13) is added onto a “Volume Force” node. On the surface of the cylinder, the so-called Lagrangian mean velocity, defined as  $\mathbf{u}^L = \langle \mathbf{u}_2 \rangle + \left\langle \frac{1}{(i\omega)} \mathbf{u}_1 \cdot \nabla \mathbf{u}_1 \right\rangle$ , is set to be zero<sup>171</sup>. To truncate the simulation domain, a “Wall Node” with a no slip boundary condition is applied on the outer boundary of the fluid domain. Following Muller and Bruus<sup>172</sup>, a zero spatial average of the second pressure is enforced by a Lagrange multiplier to ensure convergence of the second-order flow fields.

## 5.4 Results and discussion

### 5.4.1 Imaging of trichomes

Trichomes of the tomato stem were, as reported elsewhere<sup>173,174</sup>, heterogeneous, long and slender (Fig. 5.1a). Trichomes were arranged in a radial pattern. Outer diameters were  $41 \pm 11$   $\mu\text{m}$ , with axial lengths of  $2930 \pm 609$   $\mu\text{m}$  ( $n = 40$  trichomes). Trichome wall thicknesses were  $1$   $\mu\text{m}$ <sup>45</sup>.

### 5.4.2 Validation of the model

To validate the model, we began by investigating the acoustic radiation force associated with a plane *travelling* wave (Fig. 5.2). Because the acoustic radiation force function is expressed as an infinite series ((Eq. (5.42)), we first tested convergence and truncation error. Because the normalized frequency was such that  $R/\lambda \leq 0.12$ , the limitation  $\delta \ll \lambda$  held true. In this particular case, the viscous effects are incorporated by setting  $\delta/R = 0.1$  and density ratio  $\rho' = 1000$ . Even for small values of  $R/\lambda$ , retaining only the  $n = 0$  term is insufficient to capture the acoustic radiation force on a rigid cylinder (Fig. 5.4), and higher-order terms improve the accuracy of the acoustic radiation force prediction. However, when  $n = 20$ , the acoustic radiation force curve differs negligibly with its counterpart obtained with  $n = 2$ . Therefore, all of the results presented below are calculated with  $n = 20$  in order to ensure the convergence of the series.

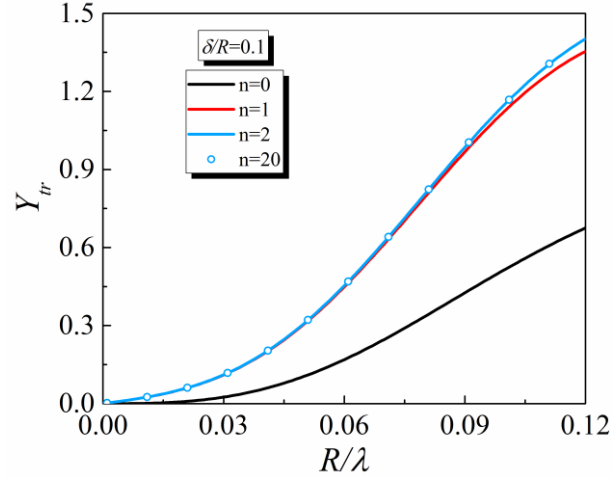


*FIG. 5.4. Convergence of the infinite series. Progressively higher order terms improved the estimation of acoustic radiation force for a rigid cylinder in plane travelling wave for  $\delta/R = 0.1$ ,  $\mu' = 0$  and  $\rho' = 1000$ . Beyond  $n = 2$ , the increase in accuracy associated with including additional terms was negligible. However, to ensure convergence in all simulations,  $n = 20$  terms were used.*

To validate the theoretical predictions of the acoustic radiation force, they are compared to FE predictions for a plane travelling wave (Figure 5.5). As can be seen from Fig. 5.5(a), the theoretical predictions agree well with the FE simulation results, except for the high viscosity case ( $\delta = 0.2R$ ) at relatively large radius ( $R/\lambda = 0.12$ ). These small discrepancies are caused by neglecting the vortical terms in Eq. (5.33). Generally, viscosity tends to increase the acoustic radiation force on a finite-sized rigid cylinder. As  $R/\lambda$  increases, the difference between the viscous and inviscid cases increases. The bulk viscosity has no effect on the acoustic radiation force, mainly because it has negligible effect on wave propagation (Fig. 5.5b). The bulk viscosity affects only the wavenumber  $k_c$  of the incident wave in Eq. (5.19). In the present study, only the case of small viscosity is considered, and relatively low frequency of the incident wave is

assumed. Therefore, the decaying part of  $k_c$  is negligible for  $\omega\mu/(\rho_0c_0^2) \ll 1$  and  $\omega\mu_b/(\rho_0c_0^2) \ll 1$ , and no difference is found for cases of different bulk viscosities. In sharp contrast, the dynamic viscosity  $\mu$  can affect the scattered shear wave by influencing the wavenumber  $k_v (= (1+i)\sqrt{\omega\rho_0/(2\mu)})$  in Eq. (5.21). A small change in  $\mu$  will significantly affect  $k_v$  and, as a consequence, the scattered wave field. Therefore, the influence of dynamic viscosity on acoustic radiation force is non-negligible.

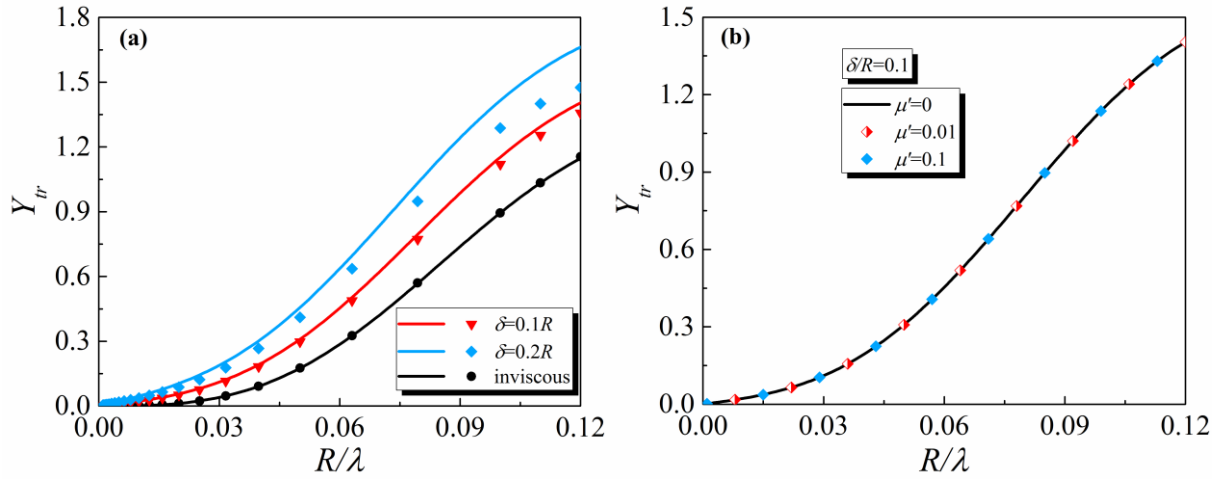


FIG. 5.5. (a) Comparison of theoretical model predictions and numerical simulations for the acoustic radiation force function  $Y_{tr}$  (Eq. 5.42) on a rigid cylinder for a plane travelling wave. Shown are results for  $\rho' = 1000$  and  $\mu' = 0$ . (b) Effect of bulk viscosity on acoustic radiation force in a plane travelling wave for  $\delta/R = 0.1$  and  $\rho' = 1000$ .

### 5.4.3 A tomato trichome is both acoustically and mechanically rigid compared to air

The acoustic radiation force increases with the rigid cylinder radius and with the density ratio  $\rho'$  (Fig. 5.6). However, when the density ratio  $\rho'$  reaches 100, the acoustic radiation force tends to

saturate because at high density ratio the acoustically rigid cylinder's vibrations are attenuated and the cylinder becomes mechanically rigid. Because the acoustic impedance of a tomato trichome is far larger than that of air, the tomato trichome can be treated as long, acoustically rigid cylinder. Meanwhile, the density ratio between the trichome and the air can be as large as 800. Based on the results shown in Fig. 5.6, at a density ratio of 800, the rigid cylinder acts like an immovable cylinder of diameters  $41 \pm 11 \mu\text{m}$ , and axial lengths of  $2930 \pm 609 \mu\text{m}$  so that the model applies to the case of a trichome constrained at one end.

### 5.4.3 Effects of animal sound emissions on tomato trichomes

The sound pressure associated with acoustic emissions decreases with distance according to<sup>166,167</sup>:

$$p_B = p_A \frac{r_A}{r_B} \quad (5.49)$$

in which  $p_A$  is the pressure at distance  $r_A$  from the source and  $p_B$  is the pressure at distance  $r_B$ . This pressure relates to the commonly used metric “sound pressure level” (SPL) for characterizing loudness as<sup>166,167</sup>

$$p = p_{ref} \cdot 10^{\frac{SPL}{20}} \quad (5.50)$$

where  $p_{ref} = 20 \mu\text{Pa}$  is the reference sound pressure.

The ranges of sound pressure and frequency emitted by several animals of relevance, including insect herbivores, are listed in Table 5.3. Based on these parameters, we calculate the largest normal stress at the base of a tomato trichome (Fig. 5.7). Note that we studied sounds that

originate 100-500  $\mu\text{m}$  away from the trichome for noises arising from insects, 1-10 mm away for noises arising from birds, and 10-100 mm away for noises arising from mammals. The range of sound pressures and frequencies varies by species (Fig. 5.7). Over the frequency ranges emitted by animals, flexural stress increased with frequency and amplitude of acoustic emissions. This is expected from Eq. (5.44), in which stress scales with sound pressure as  $\frac{p^2}{\rho_{\text{air}}c_{\text{air}}^2}$ . For frequencies over the range of 1-200 kHz (normalized frequency  $5.7 \times 10^{-5} \leq R/\lambda \leq 1.1 \times 10^{-2}$  in Fig. 5.5) the acoustic radiation forces and hence peak normal stress on the trichome increases monotonically with frequency.

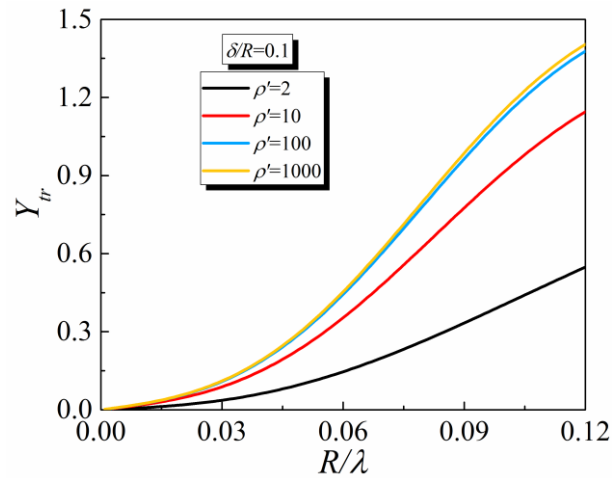
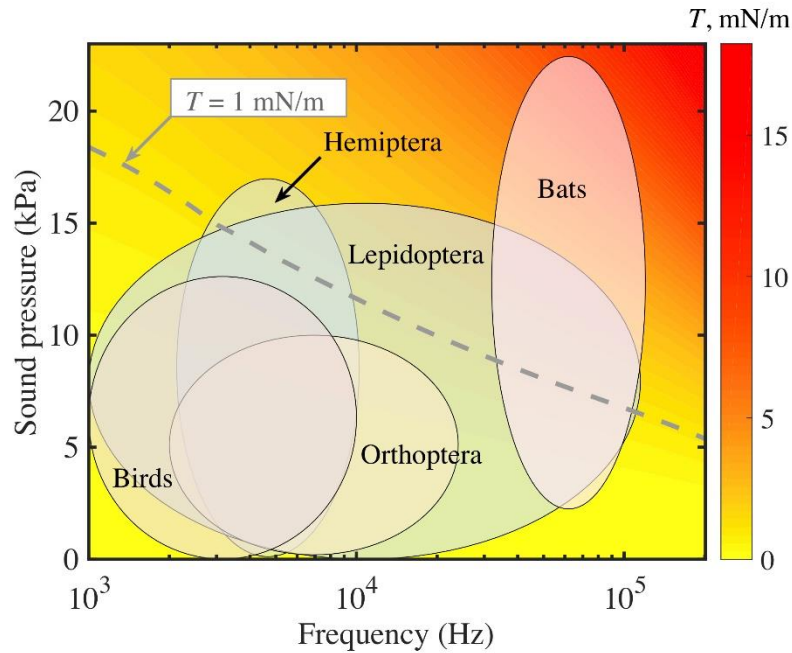


FIG. 5.6. Effect of density ratio on the acoustic radiation force on an acoustically rigid cylinder subjected to a plane travelling wave for  $\delta/R = 0.1$  and  $\mu' = 0$ .



*Fig. 5.7. Estimates of the membrane tension,  $T$ , that would arise in the membrane of a tomato trichome in response to acoustic excitation from a range of species that emit different combinations of frequency and pressure.*

Two types of stress matter for acoustic mechanosensation: pressure associated with loudness, and stresses that can arise as these pressures bend the trichome. Because the impedance of air is so much smaller than that of a trichome, vibration of the trichome is negligible, and the pressure acts quasi-statically<sup>166,167</sup>. The effect of flexure on the trichome is sufficient to cause strains of several percent at the base of the trichome. If these strains were transmitted to the plasma membrane, they could affect the opening probabilities of mechanosensitive ion channels that in turn mediate influx of  $\text{Ca}^{2+}$ <sup>42,175</sup>. Influxes of  $\text{Ca}^{2+}$  have been speculated to enable trichomes to function as mechanoelectrical switches<sup>42,45</sup>. These signals can be used by the plant to time the

production of metabolically expensive compounds, as occurs in flowers of *Oenothera drummondii* which, when exposed to the flight sounds of the bees that are their pollinators, produce sweeter nectar within minutes<sup>176</sup>. Inactivation and desensitization may be possible due to interplay between the periodicity of insect sounds and the dynamics of ion channel opening and closing. For example, for low frequency wind loading of entire *A. thaliana* plants, this interplay limits the range of wind mechanosensing via MSL ion channels to frequencies in the 0.3-3 Hz range<sup>177</sup>.

Higher frequency and higher pressure acoustic signals could stimulate trichomes in a way that stretches the membrane sufficiently to open stretch-activated ion channels (Fig. 5.7). To predict this, we estimated the peak stresses arising in the membrane using our estimates of pressure and  $Y_{tr}$  in Eq. (5.45). Note that we have followed the usual convention of reporting membrane stresses as a force per unit length, calculated as the product the membrane stress (a real stress with units of force per unit area) and membrane thickness. This convention is used because of observations that the opening of stress-activated ion channels relates to the force per unit length in the membrane. Membrane stresses on the order of 1 mN/m are adequate to open Piezo channels<sup>178</sup>, and stresses on the order of 2 mN/m are adequate to open MscS channels in *E. coli*.<sup>179,180</sup> The right panel of Fig. 5.7 shows the membrane tension produced by these acoustic stresses when the membrane and cell wall are considered to undergo affine deformation as in equation (5.45).

Although echolocators such as bats and moths make loud and high frequency sounds potentially sufficient to activate ion channels (Fig. 5.7), they are not herbivores of *S. lyopersicum*, and transduction of their sounds would thus not likely be useful. Circadian cycles exist in many



plants that could enable them to ignore vibrations at night, when these echolocators are active, by down-regulating the signal transduction pathway from vibration to defense response. For example jasmonate-mediated defenses in *A. thaliana* vary on a circadian basis <sup>181</sup>. Bird sounds are less likely to be transduced by trichomes due to the relatively lower flexural stresses that they might exert upon trichomes. Hemiptera may produce acoustic signals sufficient to affect Piezo channels. Although these stresses are low compared to those associated with a strong wind, their frequency and repetitive nature might combine with the dynamics of ion channels to promote sound transduction.

*Table 5.3. Range of sound frequency and sound pressure for different species*

Species	Frequency (Hz)	SPL (dB)	Sound pressure (Pa)
<i>Okanagana rimosa</i> <sup>182</sup>	7.00-10.0 kHz	87.0-90.0 dB (15 cm)	134-949 Pa
Cicadas <sup>43</sup>	2.13-10.2 kHz	75.3-105 dB (50 cm)	116 Pa-17.0 kPa
Moths <sup>183</sup>	32.0-115 kHz	76.0-125 dB (1 cm)	2.52 Pa-3.56 kPa
Hawkmoths <sup>184</sup>	1.00-100 kHz	114-118 dB (10 cm)	2.00 kPa-15.9 kPa
Katydids <sup>185</sup>	23.0 kHz	94.0 dB (10 cm)	200 Pa-1.00 kPa
Crickets <sup>186</sup>	2.00-8.00 kHz	88.0-100 dB (50 cm)	502 Pa-10.0 kPa
White bellbirds <sup>187</sup>	1.80-2.40 kHz	106-116 dB (1 m)	399 Pa-12.6 kPa <sup>1</sup>
Winter wren <sup>188</sup>	4.00-8.00 kHz	90.0 dB (1 m)	63.2 Pa-633 Pa <sup>1</sup>
17 songbird species <sup>188</sup>	0.50-10.0 kHz	74.0-100 dB (1 m)	10.0 Pa-2.00 kPa <sup>1</sup>

Bats <sup>189</sup>	32.0-120 kHz	121-137 dB (5-10 m)	2.24 kPa-22.4 kPa <sup>2</sup>
---------------------	--------------	---------------------	--------------------------------

<sup>1</sup>The distance between the sound source and the trichome ranges from 1 mm to 10 mm for birds.

<sup>2</sup>The distance between the sound source and the trichome ranges from 10 mm to 100 mm for bats. For insects, the distance ranges from 100  $\mu\text{m}$  to 500  $\mu\text{m}$ .

Our models involved treatment of a trichome as a rigid cylinder due to its many orders of magnitude difference in acoustic impedance with that of air. Such a cylinder may be subjected to additional forces due to external acoustic streaming arising from viscous effects associated with external boundary conditions (*i.e.*, the obstacle and barrier). Danilov and Mironov <sup>152,168</sup> report an increase in the acoustic radiation force with viscosity for small particles, with viscous effects dominating at length scales relevant to the diameters of the cylinders of interest in our problem. When checking this assumption, we found that when the density of the cylinder was far larger than that of the surrounding medium, the cylinder would be immovable, and the acoustic radiation force saturated. For the tomato trichome, the density was almost 800 times larger than the air. Under acoustic excitation, the tomato trichome behaved like a cantilever, with stresses that could be estimated using elasticity theory.

Our results add to a growing body of literature suggesting that mechanoperception and bioacoustics are harnessed by a range of plants to improve defenses against insect herbivores <sup>190-193</sup>. Light brushing of *Arabidopsis thaliana* trichomes causes oscillations of cytoplasmic  $\text{Ca}^{2+}$  in the skirt cells associated with tension at the base of the trichome <sup>42</sup>. Our results suggest that, similar to such brushing, sound waves may exert radiation force and bend the trichome, and motivate future experimental studies of mechanotransduction by tomato trichomes.

## 5.5 Conclusions

An analytical expression was derived for the acoustic radiation force exerted by a sound field on a finite-sized rigid cylinder suspended in a low viscosity fluid. Three length scales affected its response: the radius,  $R$ , of the rigid cylinder, the wavelength,  $\lambda$ , of the incident wave and the viscous penetration depth,  $\delta$ , with  $\delta$  assumed small compared to  $\lambda$ . Using perturbation theory approximations for the first- and second-order wave fields and a far-field approach to calculate the acoustic radiation force, a solution was found that matched numerical simulations. For plane travelling waves, viscous effects increased acoustic radiation forces. Acoustic radiation force increased monotonically with  $\delta/R$ ,  $R/\lambda$ , and density contrast; the contrast in bulk viscosity had negligible influence. When applied to acoustic emissions from insects impinging upon trichomes of *S. lycopersicum*, the solution predicted stresses tens of kPa in trichome wall, sufficient to bend trichomes and possibly affect mechanosensitive ion channels.

# **Chapter 6: Conclusions and future perspectives**

## **6.1 Conclusion**

In this dissertation, the acoustic radiation force arising from focused Gaussian ultrasound and standing surface acoustic waves were calculated for eukaryotic cells in ideal fluids. Theoretical and numerical results showed that cell mechanics could significantly affect the acoustic radiation force. We finally concluded that the sound impedance (acoustic impedance) is the main factor that governs ultrasound-based acoustic scattering and thus is the key determinant, and key factor for tuning, of acoustic radiation force. For focused Gaussian ultrasound, the beam waist could also affect the scattering, but only the magnitude of the scattering and not its direction. Thus, modifying the waist of a focused Gaussian ultrasound beam will affect the magnitude of the acoustic radiation force, but not the direction. Cell shape and mechanics are also factors, a useful result that enables cell sorting via ultrasound. For spheroidal cells, the curvature significantly affects scattering and changes the radiation force. As for standing surface acoustic waves, we showed that due to the wave form conversion, the surface wave could exert a bulk wave inside the fluid, leading to a 3D acoustic radiation force field. Furthermore, we evaluated several key factors that affect the acoustic radiation force to help us further understand the mechanics.

With this in mind, we adopted the acoustic radiation force to manipulate mechanosensitive ion channels. For simplicity, we studied the two-pore potassium channel, the TRAAK channel. We observed that the membrane current would increase gradually once we turn on the ultrasound. Cyclic loading would also cause cumulative increase of the membrane current. Those

phenomena were much like the viscoelastic properties we studied later. Our simulations showed that deformation of the oocyte we used was substantial around the electrodes that we used in our experiments, and highlighted the central role of boundary conditions in determining stress distributions. Similarly, plant cells respond to mechanical force, and we showed that in trichomes, which can serve as electromechanical switches and possibly as “ears” of a plant, the structure can amplify certain frequency ranges so that very small acoustic radiation forces from insects might possibly be amplified to induce strains that activate ion channels.

## **6.2 Perspective**

Sound waves deliver messages in daily communication, and in medical research can deliver messages in forms that are useful for clinical diagnosis. Energy based mechanical waves can also cause a nonlinear effect that leads to a static force, the acoustic radiation force. This has long been used to design and fabricate acoustic tweezers for manipulating small samples like cells. Further understanding of acoustic radiation force on eukaryotic cells is important for improving acoustic tweezers and cell sorting applications. We studied the two common ultrasound forms: focused Gaussian ultrasound and standing surface acoustic waves. The theoretical and numerical results showed that not only the ultrasound itself but also cell mechanics affect the radiation force field. Our work paves the way for better acoustic tweezers design. This work is only a beginning, however, and more detailed consideration of membrane mechanics, poroelasticity, osmotic factors, and cytoskeletal and organelle structures may lead to improved targeting of cells via ultrasound, and to important refinement of the models proposed.

Ultrasound has long been studied for treating neuronal and heart tissues. Although the basic mechanisms of ion channel opening via ultrasound is not clear, mechanical effects have been

suspected by many. Our work is the first to demonstrate definitively that ultrasound can cause membrane stretch that leads to stretch activation of ion channels. This work involved a simplified model cell and, as detailed in the first chapters of this dissertation, the cell mechanical properties, shape, and composition of more complicated cells could also affect these channels and the stresses that they receive. This is an important area for future study because acoustic radiation force, which is small inside of a tissue, will likely require amplification for clinical application. One intriguing possibility that arises from the work in this dissertation is the therapeutic application of cyclic loading, such as pulsed waves, to cause cumulative membrane current increase via the viscoelastic effects we discovered and thereby ultimately use ultrasound to control mechanosensitive ion channels in neurons. Clinical trials of this type of approach are an important next step.

Our further work on tomato trichomes also elucidated potential mechanisms for plant to sense sound. The work identified specific ranges of frequency and amplitude that are capable of inducing opening of ion channels at the base of a tomato trichome, and therefore define conditions in which further experimentation may someday be performed. The results raise intriguing possibilities about how plants behave in response to changes and their environment.

More broadly, the dissertation adds a set of models and tools for relating ultrasound parameters to quantitative estimates of acoustic radiation force on a broad range of cells, and for predicting how this force relates to opening of mechanosensitive ion channels and induction of membrane currents. We hope that the straightforward and integrated solutions, experimental approaches, and modeling frameworks will form part of the quantitative foundation for future development of acoustic technologies that control both plant and animal cells.



# References

- 1 Magde, D., Elson, E. L. & Webb, W. W. Fluorescence correlation spectroscopy. II. An experimental realization. *Biopolymers* **13**, 29-61, doi:<https://doi.org/10.1002/bip.1974.360130103> (1974).
- 2 Axelrod, D., Koppel, D. E., Schlessinger, J., Elson, E. & Webb, W. W. Mobility measurement by analysis of fluorescence photobleaching recovery kinetics. *Biophys J* **16**, 1055-1069, doi:[10.1016/s0006-3495\(76\)85755-4](https://doi.org/10.1016/s0006-3495(76)85755-4) (1976).
- 3 Daily, B., Elson, E. L. & Zahalak, G. I. Cell poking. Determination of the elastic area compressibility modulus of the erythrocyte membrane. *Biophys J* **45**, 671-682, doi:[10.1016/s0006-3495\(84\)84209-5](https://doi.org/10.1016/s0006-3495(84)84209-5) (1984).
- 4 Perkins, T. T. Optical traps for single molecule biophysics: a primer. *Laser & Photonics Reviews* **3**, 203-220, doi:<https://doi.org/10.1002/lpor.200810014> (2009).
- 5 Peng, X., He, W., Xin, F., Genin, G. M. & Lu, T. J. Standing surface acoustic waves, and the mechanics of acoustic tweezer manipulation of eukaryotic cells. *Journal of the Mechanics and Physics of Solids* **145**, 104134, doi:<https://doi.org/10.1016/j.jmps.2020.104134> (2020).
- 6 Ericsson, M., Hanstorp, D., Hagberg, P., Enger, J. & Nyström, T. Sorting Out Bacterial Viability with Optical Tweezers. *Journal of Bacteriology* **182**, 5551-5555, doi:[doi:10.1128/JB.182.19.5551-5555.2000](https://doi.org/10.1128/JB.182.19.5551-5555.2000) (2000).
- 7 Khandurina, J. & Guttman, A. Bioanalysis in microfluidic devices. *Journal of chromatography. A* **943**, 159-183, doi:[10.1016/s0021-9673\(01\)01451-0](https://doi.org/10.1016/s0021-9673(01)01451-0) (2002).
- 8 Ashkin, A., Dziedzic, J. M., Bjorkholm, J. E. & Chu, S. Observation of a single-beam gradient force optical trap for dielectric particles. *Opt. Lett.* **11**, 288-290, doi:[10.1364/OL.11.000288](https://doi.org/10.1364/OL.11.000288) (1986).
- 9 Ozcelik, A. *et al.* Acoustic tweezers for the life sciences. *Nature Methods* **15**, 1021-1028, doi:[10.1038/s41592-018-0222-9](https://doi.org/10.1038/s41592-018-0222-9) (2018).
- 10 Carovac, A., Smajlovic, F. & Junuzovic, D. Application of ultrasound in medicine. *Acta Informatica Medica* **19**, 168 (2011).
- 11 Rayleigh, L. XXXIV. on the pressure of vibrations. *The London, Edinburgh, and Dublin Philosophical Magazine and Journal of Science* **3**, 338-346 (1902).
- 12 King, L. V. On the acoustic radiation pressure on spheres. *Proceedings of the Royal Society of London. Series A - Mathematical and Physical Sciences* **147**, 212-240, doi:[doi:10.1098/rspa.1934.0215](https://doi.org/10.1098/rspa.1934.0215) (1934).
- 13 Yosioka, K. & Kawasima, Y. Acoustic radiation pressure on a compressible sphere. *Acta Acustica united with Acustica* **5**, 167-173 (1955).
- 14 Hasegawa, T. & Yosioka, K. Acoustic-radiation force on a solid elastic sphere. *The Journal of the Acoustical Society of America* **46**, 1139-1143 (1969).
- 15 Wu, J. Acoustical tweezers. *The Journal of the Acoustical Society of America* **89**, 2140-2143, doi:[10.1121/1.400907](https://doi.org/10.1121/1.400907) (1991).
- 16 Mayberg, H. S. *et al.* Deep brain stimulation for treatment-resistant depression. *Neuron* **45**, 651-660 (2005).
- 17 Bronstein, J. M. *et al.* Deep brain stimulation for Parkinson disease: an expert consensus and review of key issues. *Archives of neurology* **68**, 165-165 (2011).



- 18 Otto, K. J. & Schmidt, C. E. Neuron-targeted electrical modulation. *Science* **367**,  
1303-1304 (2020).
- 19 Modolo, J., Thomas, A. W., Stodilka, R. Z., Prato, F. S. & Legros, A. in *2010 IEEE Fifth  
International Conference on Bio-Inspired Computing: Theories and Applications  
(BIC-TA)*. 1356-1364 (IEEE).
- 20 Montgomery, K. L., Iyer, S. M., Christensen, A. J., Deisseroth, K. & Delp, S. L. Beyond  
the brain: Optogenetic control in the spinal cord and peripheral nervous system. *Science  
Translational Medicine* **8**, 337rv335-337rv335, doi:10.1126/scitranslmed.aad7577  
(2016).
- 21 Legon, W. *et al.* Transcranial focused ultrasound modulates the activity of primary  
somatosensory cortex in humans. *Nature neuroscience* **17**, 322-329 (2014).
- 22 Harvey, E. N. The effect of high frequency sound waves on heart muscle and other  
irritable tissues. *American Journal of Physiology-Legacy Content* **91**, 284-290 (1929).
- 23 FRY, F. J., ADES, H. W. & FRY, W. J. Production of Reversible Changes in the Central  
Nervous System by Ultrasound. *Science* **127**, 83-84, doi:10.1126/science.127.3289.83  
(1958).
- 24 Gavrilov, L. R., Tsurulnikov, E. M. & Davies, I. a. I. Application of focused ultrasound  
for the stimulation of neural structures. *Ultrasound in Medicine & Biology* **22**, 179-192,  
doi:https://doi.org/10.1016/0301-5629(96)83782-3 (1996).
- 25 Ye, J. *et al.* Ultrasonic Control of Neural Activity through Activation of the  
Mechanosensitive Channel MscL. *Nano Letters* **18**, 4148-4155,  
doi:10.1021/acs.nanolett.8b00935 (2018).
- 26 Prieto, M. L., Firouzi, K., Khuri-Yakub, B. T. & Maduke, M. Activation of Piezo1 but  
Not NaV1.2 Channels by Ultrasound at 43 MHz. *Ultrasound in Medicine & Biology* **44**,  
1217-1232, doi:https://doi.org/10.1016/j.ultrasmedbio.2017.12.020 (2018).
- 27 Kubanek, J. *et al.* Ultrasound modulates ion channel currents. *Scientific Reports* **6**,  
doi:10.1038/srep24170 (2016).
- 28 Kubanek, J. *et al.* Ultrasound modulates ion channel currents. *Scientific reports* **6**, 1-14  
(2016).
- 29 Yoon, K. *et al.* Effects of sonication parameters on transcranial focused ultrasound brain  
stimulation in an ovine model. *PloS one* **14**, e0224311 (2019).
- 30 Sorum, B., Rietmeijer, R. A., Gopakumar, K., Adesnik, H. & Brohawn, S. G. Ultrasound  
activates mechanosensitive TRAAK K<sup>+</sup> channels through the lipid  
membrane. *Proceedings of the National Academy of Sciences* **118**, e2006980118,  
doi:10.1073/pnas.2006980118 (2021).
- 31 Ibsen, S., Tong, A., Schutt, C., Esener, S. & Chalasani, S. H. Sonogenetics is a  
non-invasive approach to activating neurons in *Caenorhabditis elegans*. *Nat Commun* **6**,  
8264, doi:10.1038/ncomms9264 (2015).
- 32 Yang, Y. *et al.* Sonogenetics for noninvasive and cellular-level neuromodulation in  
rodent brain. *bioRxiv*, 2020.2001.2028.919910, doi:10.1101/2020.01.28.919910 (2020).
- 33 Menz, M. D. *et al.* Radiation force as a physical mechanism for ultrasonic  
neurostimulation of the ex vivo retina. *The Journal of Neuroscience*, 2394-2318,  
doi:10.1523/jneurosci.2394-18.2019 (2019).
- 34 Yoo, S., Mittelstein, D. R., Hurt, R., Lacroix, J. & Shapiro, M. G. Focused ultrasound  
excites neurons via mechanosensitive calcium accumulation and ion channel  
amplification. *bioRxiv*, 2020.2005.2019.101196, doi:10.1101/2020.05.19.101196 (2020).

- 35 Frost, C. J., Mescher, M. C., Carlson, J. E. & De Moraes, C. M. Plant Defense Priming against Herbivores: Getting Ready for a Different Battle. *Plant Physiology* **146**, 818-824, doi:10.1104/pp.107.113027 (2008).
- 36 Williams, S. E. Comparative Sensory Physiology of the Droseraceae-The Evolution of a Plant Sensory System. *Proceedings of the American Philosophical Society* **120**, 187-204 (1976).
- 37 Sultan, S. E. *Organism and Environment: Ecological Development, Niche Construction, and Adaptation*. (Oxford University Press, 2015).
- 38 Agrawal, A. A., Hastings, A. P., Johnson, M. T. J., Maron, J. L. & Salminen, J.-P. Insect Herbivores Drive Real-Time Ecological and Evolutionary Change in Plant Populations. *Science* **338**, 113-116, doi:10.1126/science.1225977 (2012).
- 39 Nayidu, N. K. *et al.* Brassica villosa, a system for studying non-glandular trichomes and genes in the Brassicas. *Plant Molecular Biology* **85**, 519-539, doi:10.1007/s11103-014-0201-1 (2014).
- 40 Hanley, M. E., Lamont, B. B., Fairbanks, M. M. & Rafferty, C. M. Plant structural traits and their role in anti-herbivore defence. *Perspectives in Plant Ecology Evolution and Systematics* **8**, 157-178, doi:10.1016/j.ppees.2007.01.001 (2007).
- 41 Suo, B. X., Seifert, S. & Kirik, V. Arabidopsis GLASSY HAIR genes promote trichome papillae development. *Journal of Experimental Botany* **64**, 4981-4991, doi:10.1093/jxb/ert287 (2013).
- 42 Zhou, L. H. *et al.* The Arabidopsis trichome is an active mechanosensory switch. *Plant Cell and Environment* **40**, 611-621, doi:10.1111/pce.12728 (2017).
- 43 Sanborn, A. F. & Phillips, P. K. Scaling of Sound Pressure Level and Body Size in Cicadas (Homoptera: Cicadidae; Tibicinidae). *Annals of the Entomological Society of America*, 4 (1995).
- 44 Appel, H. M. & Cocroft, R. B. Plants respond to leaf vibrations caused by insect herbivore chewing. *Oecologia* **175**, 1257-1266, doi:10.1007/s00442-014-2995-6 (2014).
- 45 Liu, S. *et al.* Arabidopsis Leaf Trichomes as Acoustic Antennae. *Biophysical Journal* **113**, 2068-2076, doi:10.1016/j.bpj.2017.07.035 (2017).
- 46 Klein, R. M. & Edsall, P. C. On the Reported Effects of Sound on the Growth of Plants\*. *BioScience* **15**, 125-126, doi:10.2307/1293353 (1965).
- 47 Hassanién, R. H. E., Hou, T.-z., Li, Y.-f. & Li, B.-m. Advances in Effects of Sound Waves on Plants. *Journal of Integrative Agriculture* **13**, 335-348, doi:https://doi.org/10.1016/S2095-3119(13)60492-X (2014).
- 48 Jeong, M.-J. *et al.* Plant gene responses to frequency-specific sound signals. *Molecular Breeding* **21**, 217-226, doi:10.1007/s11032-007-9122-x (2008).
- 49 Ghosh, R. *et al.* Expression Analysis of Sound Vibration-Regulated Genes by Touch Treatment in Arabidopsis. *Frontiers in Plant Science* **8**, doi:10.3389/fpls.2017.00100 (2017).
- 50 Choi, B. *et al.* Positive regulatory role of sound vibration treatment in Arabidopsis thaliana against Botrytis cinerea infection. *Scientific Reports* **7**, 2527, doi:10.1038/s41598-017-02556-9 (2017).
- 51 Schöner, M. G., Simon, R. & Schöner, C. R. Acoustic communication in plant-animal interactions. *Current Opinion in Plant Biology* **32**, 88-95, doi:https://doi.org/10.1016/j.pbi.2016.06.011 (2016).

52 Ghosh, R. *et al.* Expression Analysis of Sound Vibration-Regulated Genes by Touch Treatment in Arabidopsis. *Frontiers in Plant Science* **8**, 100 (2017).  
<<http://europepmc.org/abstract/MED/28197168>

<https://doi.org/10.3389/fpls.2017.00100>

<https://europepmc.org/articles/PMC5281610>

<https://europepmc.org/articles/PMC5281610?pdf=render>>.

53 Mishra, R. C., Ghosh, R. & Bae, H. Plant acoustics: in the search of a sound mechanism for sound signaling in plants. *Journal of Experimental Botany* **67**, 4483-4494, doi:10.1093/jxb/erw235 (2016).

54 Telewski, F. W. A unified hypothesis of mechanoperception in plants. *American Journal of Botany* **93**, 1466-1476, doi:10.3732/ajb.93.10.1466 (2006).

55 Zhang, H. *et al.* Acoustic Streaming and Microparticle Enrichment within a Microliter Droplet Using a Lamb-Wave Resonator Array. *Physical Review Applied* **9**, 064011- (2018).

56 Ding, X. *et al.* On-chip manipulation of single microparticles, cells, and organisms using surface acoustic waves. *Proceedings of the National Academy of Sciences of the United States of America* **109**, 11105-11109 (2012).

57 Xie, W. J., Cao, C. D., Lü, Y. J., Hong, Z. Y. & Wei, B. Acoustic method for levitation of small living animals. *Applied Physics Letters* **89**, 214102, doi:10.1063/1.2396893 (2006).

58 Liang, S. & Chaohui, W. Revised model for the radiation force exerted by standing surface acoustic waves on a rigid cylinder. *Physical Review E* **97**, 033103, doi:10.1103/PhysRevE.97.033103 (2018).

59 Schmitt, F. O. Ultrasonic micromanipulation. *Protoplasma* **7**, 332-340, doi:10.1007/BF01612815 (1929).

60 Harvey, E. N., Harvey, E. B. & Loomis, A. L. Further observations on the effect of high frequency sound waves on living matter. *The Biological Bulletin* **55**, 459-469 (1928).

61 Guo, F. *et al.* Three-dimensional manipulation of single cells using surface acoustic waves. *Proceedings of the National Academy of Sciences* **113**, 1522-1527 (2016).

62 Bao, G. & Suresh, S. Cell and molecular mechanics of biological materials. *Nature materials* **2**, 715-725 (2003).

63 Ding, X. *et al.* Surface acoustic wave microfluidics. *Lab on a Chip* **13**, 3626-3649 (2013).

64 Kim, M. G. *et al.* Label-free analysis of the characteristics of a single cell trapped by acoustic tweezers. *Scientific reports* **7**, 1-9 (2017).

65 Lee, J. *et al.* Transverse acoustic trapping using a Gaussian focused ultrasound. *Ultrasound in medicine & biology* **36**, 350-355 (2010).

66 Mitri, F. Acoustic radiation force on a sphere in standing and quasi-standing zero-order Bessel beam tweezers. *Annals of physics* **323**, 1604-1620 (2008).

67 Li, P. *et al.* Acoustic separation of circulating tumor cells. *Proceedings of the National Academy of Sciences* **112**, 4970-4975 (2015).

68 Marston, P. L. Axial radiation force of a Bessel beam on a sphere and direction reversal of the force. *The Journal of the Acoustical Society of America* **120**, 3518-3524 (2006).

69 Liu, J., Lewis, T. N. & Prausnitz, M. R. Non-invasive assessment and control of ultrasound-mediated membrane permeabilization. *Pharmaceutical research* **15**, 918-924 (1998).

- 70 Tachibana, K., Uchida, T., Ogawa, K., Yamashita, N. & Tamura, K. Induction of  
cell-membrane porosity by ultrasound. *The Lancet* **353**, 1409 (1999).
- 71 Sundaram, J., Mellein, B. R. & Mitragotri, S. An experimental and theoretical analysis of  
ultrasound-induced permeabilization of cell membranes. *Biophysical journal* **84**,  
3087-3101 (2003).
- 72 Juffermans, L., Dijkmans, P. A., Musters, R., Visser, C. A. & Kamp, O. Transient  
permeabilization of cell membranes by ultrasound-exposed microbubbles is related to  
formation of hydrogen peroxide. *American Journal of Physiology-Heart and Circulatory  
Physiology* **291**, H1595-H1601 (2006).
- 73 Van Wamel, A. *et al.* Vibrating microbubbles poking individual cells: drug transfer into  
cells via sonoporation. *Journal of controlled release* **112**, 149-155 (2006).
- 74 Peng, X., He, W., Liu, Y., Xin, F. & Lu, T. J. Optomechanical soft metamaterials. *Acta  
Mechanica Sinica* **33**, 575-584 (2017).
- 75 Rajabi, M. & Behzad, M. An exploration in acoustic radiation force experienced by  
cylindrical shells via resonance scattering theory. *Ultrasonics* **54**, 971-980 (2014).
- 76 King, L. V. On the acoustic radiation pressure on spheres. *Proceedings of the Royal  
Society of London. Series A-Mathematical and Physical Sciences* **147**, 212-240 (1934).
- 77 Jiang, C., Liu, X., Liu, J., Mao, Y. & Marston, P. L. Acoustic radiation force on a sphere  
in a progressive and standing zero-order quasi-Bessel-Gauss beam. *Ultrasonics* **76**, 1-9  
(2017).
- 78 Hasegawa, T. Acoustic radiation force on a sphere in a quasistationary wave  
field—theory. *The Journal of the Acoustical Society of America* **65**, 32-40 (1979).
- 79 Baresch, D., Thomas, J.-L. & Marchiano, R. Three-dimensional acoustic radiation force  
on an arbitrarily located elastic sphere. *The Journal of the Acoustical Society of America*  
**133**, 25-36 (2013).
- 80 Wu, R. *et al.* Acoustic radiation force on a double-layer microsphere by a Gaussian  
focused beam. *Journal of Applied Physics* **116**, 144903 (2014).
- 81 Azarpeyvand, M. Acoustic radiation force of a Bessel beam on a porous sphere. *The  
Journal of the Acoustical Society of America* **131**, 4337-4348 (2012).
- 82 Zhang, X. & Zhang, G. Acoustic radiation force of a Gaussian beam incident on spherical  
particles in water. *Ultrasound in medicine & biology* **38**, 2007-2017 (2012).
- 83 Hwang, J. Y. *et al.* Cell deformation by single-beam acoustic trapping: a promising tool  
for measurements of cell mechanics. *Scientific reports* **6**, 1-8 (2016).
- 84 Ford, L. Estimate of the vibrational frequencies of spherical virus particles. *Physical  
Review E* **67**, 051924 (2003).
- 85 Zhang, X. & Zhang, G. Acoustic radiation force of a Gaussian beam incident on spherical  
particles in water. *Ultrasound Med. Bio* **38**, 2007-2017,  
doi:10.1016/j.ultrasmedbio.2012.06.014 (2012).
- 86 Baddour, R. E., Sherar, M. D., Hunt, J. W., Czarnota, G. J. & Kolios, M. C.  
High-frequency ultrasound scattering from microspheres and single cells. *Journal of the  
Acoustical Society of America* **117**, 934-943, doi:10.1121/1.1830668 (2005).
- 87 Han, A., Abuhabsah, R., Miller, R. J., Sarwate, S. & O'Brien, W. D., Jr. The  
measurement of ultrasound backscattering from cell pellet biophantoms and tumors ex  
vivo. *J. Acous. Soc. Am.* **134**, 686-693, doi:10.1121/1.4807576 (2013).

- 88 Baddour, R. E. & Kolios, M. C. The fluid and elastic nature of nucleated cells: Implications from the cellular backscatter response. *Journal Of the Acoustical Society Of America* **121**, EL16-EL22, doi:10.1121/1.2401224 (2007).
- 89 Wang, Y. Y., Yao, J., Wu, X. W., Wu, D. J. & Liu, X. J. Influences of the geometry and acoustic parameter on acoustic radiation forces on three-layered nucleate cells. *Journal of Applied Physics* **122**, doi:10.1063/1.4996253 (2017).
- 90 Faran, J. J. SOUND SCATTERING BY SOLID CYLINDERS AND SPHERES. *Journal Of the Acoustical Society Of America* **23**, 405-418, doi:10.1121/1.1906780 (1951).
- 91 Wiklund, M. Acoustofluidics 12: Biocompatibility and cell viability in microfluidic acoustic resonators. *Lab on a Chip* **12**, 2018-2028, doi:10.1039/C2LC40201G (2012).
- 92 Ding, X. *et al.* Surface acoustic wave microfluidics. *Lab on a Chip* **13**, 3626-3649, doi:10.1039/C3LC50361E (2013).
- 93 Guo, F. *et al.* Controlling cell-cell interactions using surface acoustic waves. *Proceedings of the National Academy of Sciences* **112**, 43-48 (2015).
- 94 Rayleigh, L. On the pressure of vibrations. *Philosophical Magazine* **3** (1902).
- 95 King, L. V. On the Acoustic Radiation Pressure on Spheres. *Proceedings of the Royal Society of London* **147**, 212-240 (1934).
- 96 Yosioka, K. & Kawasima, Y. Acoustic Radiation Pressure on a Compressible Sphere. *Acta Acustica United with Acustica* **5**, 167-173(167) (1955).
- 97 Hasegawa, T. & Watanabe, Y. Acoustic radiation pressure on an absorbing sphere. *The Journal of the Acoustical Society of America* **63**, 1733-1737 (1978).
- 98 Azarpeyvand, M. & Azarpeyvand, M. Application of Acoustic Bessel Beams for Handling of Hollow Porous Spheres. *Ultrasound in Medicine & Biology* **40**, 422-433 (2014).
- 99 Xu, S., Qiu, C. & Liu, Z. Transversally stable acoustic pulling force produced by two crossed plane waves. *EPL (Europhysics Letters)* **99**, 44003 (2012).
- 100 Peng, X., He, W., Xin, F., Genin, G. M. & Lu, T. J. The acoustic radiation force of a focused ultrasound beam on a suspended eukaryotic cell. *Ultrasonics* **108**, 106205, doi:https://doi.org/10.1016/j.ultras.2020.106205 (2020).
- 101 Kim, M. *et al.* Acoustic trap-and-release for rapid assessment of cell motility. *Soft Matter* **15**, 4266-4275, doi:10.1039/C9SM00184K (2019).
- 102 Dung Luong, T. & Trung Nguyen, N. Surface acoustic wave driven microfluidics-a review. *Micro and Nanosystems* **2**, 217-225 (2010).
- 103 Liang, S., Chaohui, W. & Qiao, H. Force on a compressible sphere and the resonance of a bubble in standing surface acoustic waves. *Physical Review E* **98**, 043108 (2018).
- 104 Liang, S., Chaohui, W. & Qiao, H. The radiation force on a rigid sphere in standing surface acoustic waves. *Journal of Applied Physics* **124**, 104503 (2018).
- 105 Helgason, C. D. & Miller, C. L. *Basic cell culture protocols*. (Totowa, NJ.: Humana Press, 2005).
- 106 Phillips, R., Kondev, J., Theriot, J. & Garcia, H. *Physical biology of the cell*. (Garland Science, 2012).
- 107 Zhang, G. & Cui, J. Patch-clamp and perfusion techniques to study ion channels expressed in *Xenopus* oocytes. *Cold Spring Harbor Protocols* **2018**, pdb. prot099051 (2018).

- 108 Baddour, R. E., Sherar, M., Hunt, J., Czarnota, G. & Kolios, M. C. High-frequency  
ultrasound scattering from microspheres and single cells. *The Journal of the Acoustical  
Society of America* **117**, 934-943 (2005).
- 109 Mishra, P., Hill, M. & Glynne-Jones, P. Deformation of red blood cells using acoustic  
radiation forces. *Biomicrofluidics* **8**, 034109 (2014).
- 110 Marston, P. L. Axial radiation force of a Bessel beam on a sphere and direction reversal  
of the force. *Journal of the Acoustical Society of America* **120**, 3518-3524 (2006).
- 111 Pratt, R. G., Simpson, G. & Crossley, W. A. Acoustic-surface-wave properties of  
Bi<sub>12</sub>GeO<sub>20</sub>. *Electronics Letters* **8**, 127-128, doi:10.1049/el:19720091 (1972).
- 112 Holm, A., Stürzer, Q., Xu, Y. & Weigel, R. Investigation of surface acoustic waves on  
LiNbO<sub>3</sub>, quartz, and LiTaO<sub>3</sub> by laser probing. *Microelectronic Engineering* **31**, 123-127,  
doi:https://doi.org/10.1016/0167-9317(95)00334-7 (1996).
- 113 Faran Jr, J. J. Sound scattering by solid cylinders and spheres. *The Journal of the  
acoustical society of America* **23**, 405-418 (1951).
- 114 Hasegawa, T. Acoustic radiation force on a sphere in a quasistationary wave  
field—theory. *Journal of the Acoustical Society of America* **65**, 32-40 (1979).
- 115 Marquez, J. P., Genin, G. M., Zahalak, G. I. & Elson, E. L. The Relationship between  
Cell and Tissue Strain in Three-Dimensional Bio-Artificial Tissues. *Biophysical Journal*  
**88**, 778-789, doi:10.1529/biophysj.104.041947 (2005).
- 116 Marquez, J. P., Genin, G. M., Zahalak, G. I. & Elson, E. L. Thin Bio-Artificial Tissues in  
Plane Stress: The Relationship between Cell and Tissue Strain, and an Improved  
Constitutive Model. *Biophysical Journal* **88**, 765-777,  
doi:https://doi.org/10.1529/biophysj.104.040808 (2005).
- 117 Elson, E. & Genin, G. The role of mechanics in actin stress fiber kinetics. *Experimental  
cell research* **319**, 2490-2500 (2013).
- 118 Rodriguez, M. L., McGarry, P. J. & Sniadecki, N. J. Review on cell mechanics:  
experimental and modeling approaches. *Applied Mechanics Reviews* **65** (2013).
- 119 Shakiba, D. *et al.* The Balance between Actomyosin Contractility and Microtubule  
Polymerization Regulates Hierarchical Protrusions That Govern Efficient  
Fibroblast-Collagen Interactions. *ACS nano* (2020).
- 120 Babaei, B., Davarian, A., Pryse, K. M., Elson, E. L. & Genin, G. M. Efficient and  
optimized identification of generalized Maxwell viscoelastic relaxation spectra. *Journal  
of the mechanical behavior of biomedical materials* **55**, 32-41 (2016).
- 121 Babaei, B. *et al.* Remodeling by fibroblasts alters the rate-dependent mechanical  
properties of collagen. *Acta biomaterialia* **37**, 28-37 (2016).
- 122 Guilak, F., Nims, R. J., Dicks, A., Wu, C.-L. & Meulenbelt, I. Osteoarthritis as a disease  
of the cartilage pericellular matrix. *Matrix Biology* **71**, 40-50 (2018).
- 123 Tandon, N. *et al.* Optimization of electrical stimulation parameters for cardiac tissue  
engineering. *Journal of tissue engineering and regenerative medicine* **5**, e115-e125  
(2011).
- 124 Lee, W. *et al.* Image-guided transcranial focused ultrasound stimulates human primary  
somatosensory cortex. *Scientific reports* **5**, 1-10 (2015).
- 125 Menz, M. D., Oralkan, Ö., Khuri-Yakub, P. T. & Baccus, S. A. Precise Neural  
Stimulation in the Retina Using Focused Ultrasound. *The Journal of Neuroscience* **33**,  
4550-4560, doi:10.1523/jneurosci.3521-12.2013 (2013).

- 126 Yang, Y. *et al.* Sonothermogenetics for noninvasive and cell-type specific deep brain neuromodulation. *Brain Stimulation*, doi:<https://doi.org/10.1016/j.brs.2021.04.021> (2021).
- 127 Brohawn, S. G., Su, Z. & MacKinnon, R. Mechanosensitivity is mediated directly by the lipid membrane in TRAAK and TREK1 K<sup>+</sup> channels. *Proceedings of the National Academy of Sciences* **111**, 3614-3619, doi:10.1073/pnas.1320768111 (2014).
- 128 Peng, X., He, W., Xin, F., Genin, G. M. & Jian Lu, T. The acoustic radiation force of a focused ultrasound beam on a suspended eukaryotic cell. *Ultrasonics*, 106205, doi:<https://doi.org/10.1016/j.ultras.2020.106205> (2020).
- 129 Boyle, J. J. *et al.* Simple and accurate methods for quantifying deformation, disruption, and development in biological tissues. *Journal of the Royal Society Interface* **11**, 20140685 (2014).
- 130 Boyle, J. J. *et al.* Regularization-Free Strain Mapping in Three Dimensions, With Application to Cardiac Ultrasound. *Journal of biomechanical engineering* **141**, 0110101-01101011, doi:10.1115/1.4041576 (2019).
- 131 Findley, W. N., Lai, J. S., Onaran, K. & Christensen, R. Creep and relaxation of nonlinear viscoelastic materials with an introduction to linear viscoelasticity. (1977).
- 132 Fung, Y.-c. *Biomechanics: mechanical properties of living tissues*. (Springer Science & Business Media, 2013).
- 133 Chaudhuri, O., Cooper-White, J., Janmey, P. A., Mooney, D. J. & Shenoy, V. B. Effects of extracellular matrix viscoelasticity on cellular behaviour. *Nature* **584**, 535-546, doi:10.1038/s41586-020-2612-2 (2020).
- 134 Peng, X., He, W., Xin, F., Genin, G. M. & Lu, T. J. Effects of coating on dynamic stress concentration in fiber reinforced composites. *International Journal of Solids and Structures* **222**, 111029 (2021).
- 135 Sultan, S. E. *Organism and environment: ecological development, niche construction, and adaptation*. (Oxford University Press, USA, 2015).
- 136 Agrawal, A. A., Hastings, A. P., Johnson, M. T., Maron, J. L. & Salminen, J.-P. Insect herbivores drive real-time ecological and evolutionary change in plant populations. *Science* **338**, 113-116 (2012).
- 137 Park, K., Knoblauch, J., Oparka, K. & Jensen, K. H. Controlling intercellular flow through mechanosensitive plasmodesmata nanopores. *Nature Communications* **10**, 3564, doi:10.1038/s41467-019-11201-0 (2019).
- 138 Chehab, E. W., Wang, Y. & Braam, J. in *Mechanical Integration of Plant Cells and Plants* (ed Przemyslaw Wojtaszek) 173-194 (Springer Berlin Heidelberg, 2011).
- 139 Chen, S., Ehrhardt, D. W. & Somerville, C. R. Mutations of cellulose synthase (CESA1) phosphorylation sites modulate anisotropic cell expansion and bidirectional mobility of cellulose synthase. *Proc Natl Acad Sci U S A* **107**, 17188-17193, doi:10.1073/pnas.1012348107 (2010).
- 140 Tilsner, J., Amari, K. & Torrance, L. Plasmodesmata viewed as specialised membrane adhesion sites. *Protoplasma* **248**, 39-60, doi:10.1007/s00709-010-0217-6 (2011).
- 141 Brault, M. L. *et al.* Multiple C2 domains and transmembrane region proteins (MCTP s) tether membranes at plasmodesmata. *EMBO reports* **20**, e47182 (2019).
- 142 Xu, G. & Shao, J.-Y. Human neutrophil surface protrusion under a point load: location independence and viscoelasticity. *American Journal of Physiology-Cell Physiology* **295**, C1434-C1444 (2008).

- 143 Wu, S.-H. *et al.* Viscoelastic deformation of lipid bilayer vesicles. *Soft Matter* **11**,  
7385-7391 (2015).
- 144 Murdock, D. R., Ermilov, S. A., Qian, F., Brownell, W. E. & Anvari, B. in  
*Nanobiophotonics and Biomedical Applications*. 118-125 (International Society for  
Optics and Photonics).
- 145 Boal, D. *Mechanics of the Cell* Cambridge University Press. *New York, Cambridge, UK*  
(2002).
- 146 Jensen, F. B., Kuperman, W. A., Porter, M. B. & Schmidt, H. *Computational Ocean*  
*Acoustics*. (Springer Publishing Company, Incorporated, 2011).
- 147 Bowman, J. J., Senior, T. B. A. & Uslenghi, P. L. E. *Electromagnetic and acoustic*  
*scattering by simple shapes (Revised edition)*. (1987).
- 148 Mitri, F. G. & Fella, Z. E. A. New expressions for the radiation force function of  
spherical targets in stationary and quasi-stationary waves. *Archive Of Applied Mechanics*  
**77**, 1-9, doi:10.1007/s00419-006-0073-1 (2007).
- 149 Tian, D., Tooker, J., Peiffer, M., Chung, S. H. & Felton, G. W. Role of trichomes in  
defense against herbivores: comparison of herbivore response to woolly and hairless  
trichome mutants in tomato (*Solanum lycopersicum*). *Planta* **236**, 1053-1066,  
doi:10.1007/s00425-012-1651-9 (2012).
- 150 Wilkens, R. T., Shea, G. O., Halbreich, S. & Stamp, N. E. Resource availability and the  
trichome defenses of tomato plants. *Oecologia* **106**, 181-191, doi:10.1007/BF00328597  
(1996).
- 151 Mitri, F. G. Theoretical and experimental determination of the acoustic radiation force  
acting on an elastic cylinder in a plane progressive wave—far-field derivation approach.  
*New Journal of Physics* **8**, 138 (2006).
- 152 Annamalai, S., Balachandar, S. & Parmar, M. K. Mean force on a finite-sized spherical  
particle due to an acoustic field in a viscous compressible medium. *Physical Review E*  
*Statistical Nonlinear & Soft Matter Physics* **89**, 053008.
- 153 Radwan, H. R. & Genin, J. Nonlinear Vibrations of Thin Cylinders. *Journal of Applied*  
*Mechanics* **43**, 370-372, doi:10.1115/1.3423849 (1976).
- 154 Ting, E. C. & Hosseinipour, A. A numerical approach for flow-induced vibration of pipe  
structures. *Journal of Sound and Vibration* **88**, 289-298,  
doi:https://doi.org/10.1016/0022-460X(83)90689-2 (1983).
- 155 Lesmez, M. W., Wiggert, D. C. & Hatfield, F. J. Modal Analysis of Vibrations in  
Liquid-Filled Piping Systems. *Journal of Fluids Engineering* **112**, 311-318,  
doi:10.1115/1.2909406 (1990).
- 156 MacBain, J. C. & Genin, J. Effect of support flexibility on the fundamental frequency of  
vibrating beams. *Journal of the Franklin Institute* **296**, 259-273,  
doi:https://doi.org/10.1016/0016-0032(73)90797-7 (1973).
- 157 MacBain, J. C. & Genin, J. Natural frequencies of a beam considering support  
characteristics. *Journal of Sound and Vibration* **27**, 197-206,  
doi:https://doi.org/10.1016/0022-460X(73)90061-8 (1973).
- 158 Wayne, R. & Staves, M. P. THE DENSITY OF THE CELL SAP AND ENDOPLASM  
OF NITELLOPSIS AND CHARA. *Plant and Cell Physiology* **32**, 1137-1144 (1991).
- 159 Chanliaud, E., Burrows, K. M., Jeronimidis, G. & Gidley, M. J. Mechanical properties of  
primary plant cell wall analogues. *Planta* **215**, 989-996, doi:10.1007/s00425-002-0783-8  
(2002).



- 160 Liu, Y. X. *et al.* Modelling the mechanics of partially mineralized collagen fibrils, fibres  
and tissue. *Journal of the Royal Society Interface* **11**, doi:10.1098/rsif.2013.0835 (2014).
- 161 Tan, Y., Sun, D. & Huang, W. Mechanical modeling of red blood cells during optical  
stretching. *Journal of biomechanical engineering* **132** (2010).
- 162 Daily, B., Elson, E. L. & Zahalak, G. I. Cell poking. Determination of the elastic area  
compressibility modulus of the erythrocyte membrane. *Biophysical journal* **45**, 671-682  
(1984).
- 163 Foresti, D., Nabavi, M. & Poulikakos, D. On the acoustic levitation stability behaviour of  
spherical and ellipsoidal particles. *Journal of Fluid Mechanics* **709**, 581-592,  
doi:10.1017/jfm.2012.350 (2012).
- 164 Andrade, M. A. B., Perez, N. & Adamowski, J. C. Review of Progress in Acoustic  
Levitation. *Brazilian Journal of Physics* **48**, 190-213, doi:10.1007/s13538-017-0552-6  
(2018).
- 165 Guo, F. *et al.* Three-dimensional manipulation of single cells using surface acoustic  
waves. *Proceedings of the National Academy of Sciences of the United States of America*  
**113**, 1522-1527, doi:10.1073/pnas.1524813113 (2016).
- 166 Ginsberg, J. H. *Acoustics-a textbook for engineers and physicists: volume i:  
fundamentals.* (2017).
- 167 Ginsberg, J. H. *Acoustics-A Textbook for Engineers and Physicists: Volume II:  
Applications.* (2018).
- 168 Danilov, S. D. & Mironov, M. A. Mean force on a small sphere in a sound field in a  
viscous fluid. *The Journal of the Acoustical Society of America* (2000).
- 169 Settnes, M. & Bruus, H. Forces acting on a small particle in an acoustical field in a  
viscous fluid. *Physical Review E* **85**, 016327, doi:10.1103/PhysRevE.85.016327 (2012).
- 170 Milton, G. W. & Sawicki, A. Theory of composites. Cambridge monographs on applied  
and computational mathematics. *Appl. Mech. Rev.* **56**, B27-B28 (2003).
- 171 Hahn, P., Leibacher, I., Baasch, T. & Dual, J. Numerical simulation of acoustofluidic  
manipulation by radiation forces and acoustic streaming for complex particles. *Lab on A  
Chip* **15**, 4302-4313 (2015).
- 172 Muller, P. B. & Bruus, H. Theoretical study of time-dependent, ultrasound-induced  
acoustic streaming in microchannels. *Phys Rev E Stat Nonlin Soft Matter Phys* **92**,  
063018 (2015).
- 173 Kang, J.-H., Shi, F., Jones, A. D., Marks, M. D. & Howe, G. A. Distortion of trichome  
morphology by the hairless mutation of tomato affects leaf surface chemistry. *Journal of  
experimental botany* **61**, 1053-1064 (2010).
- 174 Balcke, G. U. *et al.* Multi-omics of tomato glandular trichomes reveals distinct features  
of central carbon metabolism supporting high productivity of specialized metabolites.  
*The Plant Cell* **29**, 960-983 (2017).
- 175 Basu, D. & Haswell, E. S. Plant mechanosensitive ion channels: an ocean of possibilities.  
*Current Opinion in Plant Biology* **40**, 43-48 (2017).
- 176 Veits, M. *et al.* Flowers respond to pollinator sound within minutes by increasing nectar  
sugar concentration. *Ecology letters* **22**, 1483-1492 (2019).
- 177 Tran, D. *et al.* Cellular transduction of mechanical oscillations in plants by the  
plasma-membrane mechanosensitive channel MSL10. *Proceedings of the National  
Academy of Sciences* **118**, e1919402118, doi:10.1073/pnas.1919402118 (2021).

- 178 Lewis, A. H. & Grandl, J. Mechanical sensitivity of Piezo1 ion channels can be tuned by  
cellular membrane tension. *Elife* **4**, e12088 (2015).
- 179 Moe, P. & Blount, P. Assessment of potential stimuli for mechano-dependent gating of  
MscL: effects of pressure, tension, and lipid headgroups. *Biochemistry* **44**, 12239-12244  
(2005).
- 180 Sukharev, S. Purification of the small mechanosensitive channel of escherichia coli  
(mscS): the subunit structure, conduction, and gating characteristics in liposomes.  
*Biophysical journal* **83**, 290-298 (2002).
- 181 Goodspeed, D., Chehab, E. W., Min-Venditti, A., Braam, J. & Covington, M. F.  
Arabidopsis synchronizes jasmonate-mediated defense with insect circadian behavior.  
*Proceedings of the National Academy of Sciences* **109**, 4674-4677 (2012).
- 182 Stölting, H., Moore, T. E. & Lakes-Harlan, R. Substrate vibrations during acoustic  
signalling in the cicada *Okanagana rimosa*. *Journal of Insect Science* **2**.
- 183 Nakano, R. *et al.* Moths are not silent, but whisper ultrasonic courtship songs. *The  
Journal of Experimental Biology* **212**, 4072-4078, doi:10.1242/jeb.032466 (2009).
- 184 Barber, J. R. & Kawahara, A. Y. Hawkmoths produce anti-bat ultrasound. *Biology  
Letters* **9**, doi:10.1098/rsbl.2013.0161 (2013).
- 185 Montealegre, F. & Robert, D. Biomechanics of hearing in katydid. *Journal of  
Comparative Physiology a-Neuroethology Sensory Neural and Behavioral Physiology*  
**201**, 5-18, doi:10.1007/s00359-014-0976-1 (2015).
- 186 Robillard, T., Montealegre-Z, F., Desutter-Grandcolas, L., Grandcolas, P. & Robert, D.  
Mechanisms of high-frequency song generation in brachypterous crickets and the role of  
ghost frequencies. *Journal of Experimental Biology* **216**, 2001-2011,  
doi:10.1242/jeb.083964 (2013).
- 187 Podos, J. & Cohn-Haft, M. Extremely loud mating songs at close range in white  
bellbirds. *Current Biology* **29**, R1068-R1069, doi:10.1016/j.cub.2019.09.028 (2019).
- 188 Nottebohm, F. Nature's music: The science of birdsong. *Nature* **435**, 146-146,  
doi:10.1038/435146a (2005).
- 189 Surlykke, A. & Kalko, E. K. V. Echolocating Bats Cry Out Loud to Detect Their Prey.  
*Plos One* **3**, doi:10.1371/journal.pone.0002036 (2008).
- 190 Jayaraman, D., Gilroy, S. & Ané, J. M. Staying in touch: mechanical signals in  
plant-microbe interactions. *Curr Opin Plant Biol* **20**, 104-109,  
doi:10.1016/j.pbi.2014.05.003 (2014).
- 191 Hamant, O. & Haswell, E. S. Life behind the wall: sensing mechanical cues in plants.  
*BMC Biol* **15**, 59, doi:10.1186/s12915-017-0403-5 (2017).
- 192 Frongia, F., Forti, L. & Arru, L. Sound perception and its effects in plants and algae.  
*Plant signaling & behavior* **15**, 1828674, doi:10.1080/15592324.2020.1828674 (2020).
- 193 Khait, I., Obolski, U., Yovel, Y. & Hadany, L. Sound perception in plants. *Seminars in  
cell & developmental biology* **92**, 134-138, doi:10.1016/j.semcd.2019.03.006 (2019).

# Appendix A1. Standing surface acoustic waves, and the mechanics of acoustic tweezer manipulation of eukaryotic cells

The wave fields in cortical layer, cytoplasm, and cell nucleus can be explicitly expressed as a function of  $X_n(\theta, \varphi; k_f y_0, \theta_R)$ :

$$\begin{aligned}
 X_n(\theta, \varphi; k_f y_0, \theta_R) &= 2i^n(2n+1)(P_n(0)P_n(\cos\theta)\cos(k_f y_0 \sin\theta_R) \\
 &+ 2 \sum_{m=1}^n \frac{(n-m)!}{(n+m)!} P_n^m(0)P_n^m(\cos\theta) (\cos(k_f y_0 \sin\theta_R) \cos m\varphi \cos m\theta_R \\
 &\quad + i \sin(k_f y_0 \sin\theta_R) \sin m\varphi \sin m\theta_R)) \\
 \phi_2 &= \phi_0 e^{-i\omega t} \sum_{n=0}^{\infty} A_n j_n(k_2 r) X_n(\theta, \varphi; k_f y_0, \theta_R) \tag{A1.1}
 \end{aligned}$$

$$\phi_3 = \phi_0 e^{-i\omega t} \sum_{n=0}^{\infty} B_n j_n(k_3 r) X_n(\theta, \varphi; k_f y_0, \theta_R) \tag{A1.2}$$

$$\phi_4 = \phi_0 e^{-i\omega t} \sum_{n=0}^{\infty} C_n j_n(k_4 r) X_n(\theta, \varphi; k_f y_0, \theta_R) \tag{A1.3}$$

where  $A_n$ ,  $B_n$ , and  $C_n$  are three different unknown coefficients describing the longitudinal wave, and  $P_n^m(\cos\theta)$  denotes the associated Legendre polynomial. The remaining details of this derivation follow Liang<sup>103</sup>.

In the derivations of Eqs. (15) and (23), the following equations are adopted:

$$\int_0^{2\pi} \cos n\theta \cos m\theta \cos\theta d\theta = \begin{cases} \pi & (n+m=1) \\ \frac{\pi}{2} & (n-m=\pm 1) \\ 0 & (n \neq 0, m \neq 0) \\ 0 & \text{otherwise} \end{cases} \tag{A1.4}$$

$$\int_0^{2\pi} \sin n\theta \sin m\theta \cos\theta d\theta = \begin{cases} \frac{\pi}{2} & (n-m=\pm 1) \\ 0 & (n \neq 0, m \neq 0) \\ 0 & \text{otherwise} \end{cases} \tag{A1.5}$$

$$\int_0^{2\pi} \cos n \theta \sin m \theta \cos \theta d\theta = \begin{cases} 0 & (n = 1, m = 0) \\ \pi & (n = 0, m = 1) \\ -\frac{\pi}{2} & (n - m = 1, m \neq 0) \\ \frac{\pi}{2} & (m - n = 1, n \neq 0) \\ 0 & \text{otherwise} \end{cases} \quad (\text{A1.6})$$

$$\int_0^{2\pi} \cos n \theta \cos m \theta \sin \theta d\theta = 0 \quad (\text{A1.7})$$

## Appendix A2. Mechanical memory in ion channel function

Table A2.1. Values of material properties used in finite element simulations.

	ND96	Oocyte
Density, kg/m <sup>3</sup>	1000	1139
Sound speed, m/s	1500	1680
1 <sup>st</sup> elastic modulus, Pa	Not applicable	27.3
2 <sup>nd</sup> elastic modulus, Pa	Not applicable	25.9
3 <sup>rd</sup> elastic modulus, Pa	Not applicable	12.5
1 <sup>st</sup> time constant, s	Not applicable	0.18
2 <sup>nd</sup> time constant, s	Not applicable	1.4
3 <sup>rd</sup> time constant, s	Not applicable	20.9

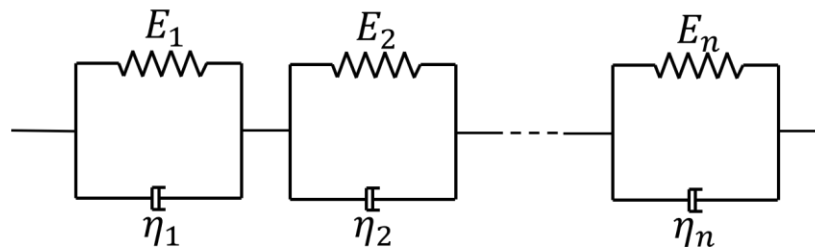


FIG. A2.1 A generalized Kelvin viscoelastic model ( $n$  Voigt elements in serial)

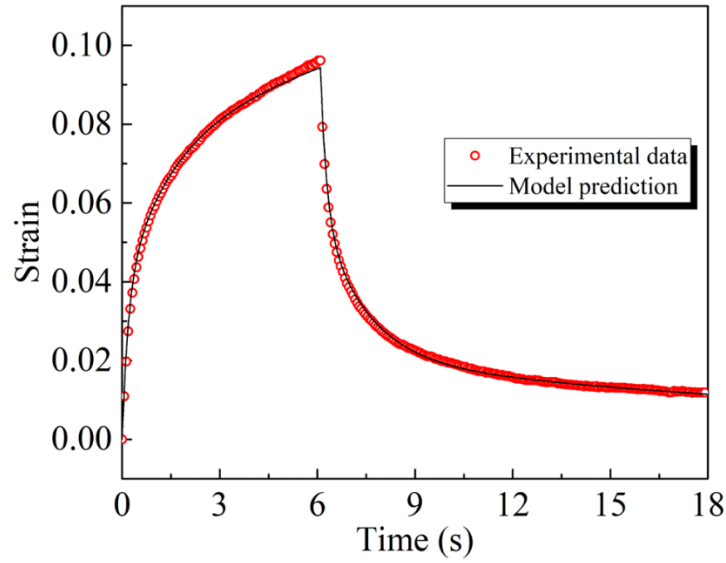


FIG. A2.2 A representative fitting for the averaged first principal strain by generalized Kelvin model. Three time constants ( $\tau_1 = 0.18$  s,  $\tau_2 = 1.38$  s,  $\tau_3 = 21$  s) can be enough to obtain a great fitting.

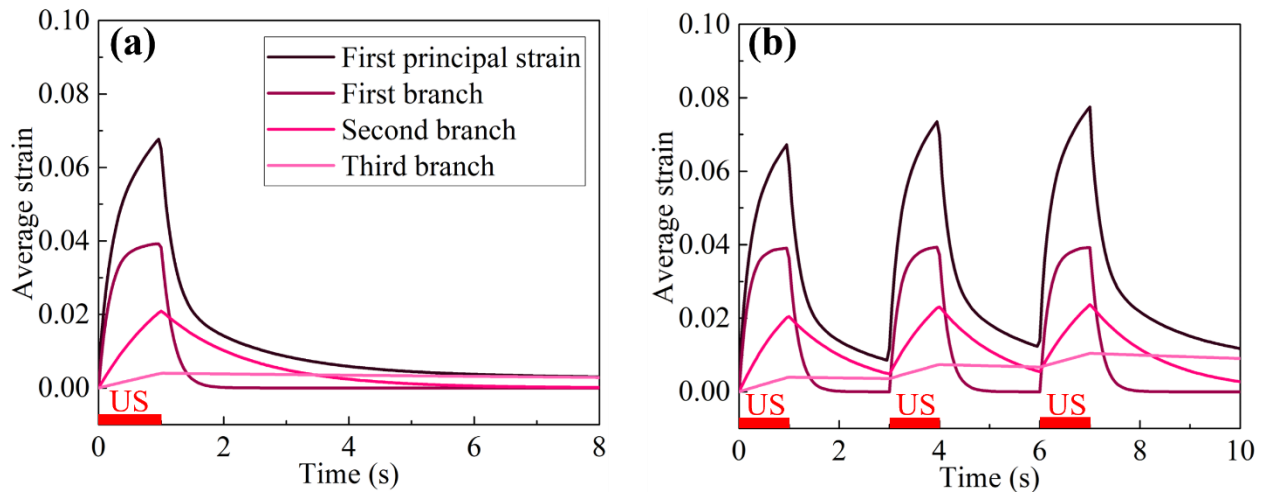


FIG. A2.3 (a) and (b) are the three branches' contribution on the first principal strain.

# Curriculum Vitae

**Xiangjun Peng**

St. Louis, MO; [xiangjunpeng@wustl.edu](mailto:xiangjunpeng@wustl.edu)

Curriculum Vitae

## Education

---

**Ph.D.**, Department of Biomedical Engineering

09/2019-Present

Washington University, St. Louis, Missouri

**Doctor of Philosophy**, Solid Mechanics

09/2016-present

Xi'an Jiaotong University, Xi'an, Shaanxi

**Bachelor of Science**, Engineering Mechanics

09/2012-06/2016

Wuhan University of Technology, Wuhan, Hubei

## Research Experience

---

Washington University, St. Louis, Missouri

09/2019-Present

Department of Biomedical Engineering

Dissertation Project: *Acoustic radiation force and its application for cell manipulation and ion channels activation*

- Theoretically and numerically solved for the acoustic radiation force by focus Gaussian ultrasound on eukaryotic cells
- Proposed a new model to account for acoustic radiation force by standing surface acoustic waves (SSAW) and test the viscoelasticity of eukaryotic cells experimentally
- Theoretically, numerically, and experimentally studied the ultrasound activation of mechanosensitive ion channels
- Used a new method to solve the Navier-Stokes equations and extend the solution to radiation force on tomato trichomes

## Publications

---

- **Peng X**, Liu Y, He W, et al. The mechanics of a sound wave impinging upon a long cylinder, and the prospect of acoustic signal transduction by tomato trichomes, (under review)
- **Peng X**, He W, Xin F, et al. Effects of coating on dynamic stress concentration in fiber reinforced composites. *International Journal of Solids and Structures*, 2021, 222: 111029.
- He W, Liu M, **Peng X**, et al. Sound absorption of petal shaped micro-channel porous materials. *Physics of Fluids*, 2021, 33(6): 063606.
- He W, **Peng X**, Xin F, et al. Ultralight micro-perforated sandwich panel with hierarchical honeycomb core for sound absorption. *Journal of Sandwich Structures & Materials*, 2021: 1099636221993880.
- **Peng X**, He W, Xin F, et al. Standing surface acoustic waves, and the mechanics of acoustic tweezer manipulation of eukaryotic cells. *Journal of the Mechanics and Physics of Solids*, 2020, 145: 104134.
- He W, **Peng X**, Chen X, et al. 3D mechanical analysis of a self-contractile cell with stress fibers reorganization. *Applied Mathematical Modelling*, 2021, 92: 710-718.
- Yin J, Liu H, Jiao J, **Peng X**, et al. Ensembles of the leaf trichomes of Arabidopsis thaliana selectively vibrate in the frequency range of its primary insect herbivore. *Extreme Mechanics Letters*, 2021: 101377.
- Liu Y, Schwartz A G, Hong Y, **Peng X**, et al. Correction of bias in the estimation of cell volume fraction from histology sections. *Journal of Biomechanics*, 2020, 104: 109705.
- Xu Z, He W, **Peng X**, et al. Sound absorption theory for micro-perforated panel with petal-shaped perforations. *The Journal of the Acoustical Society of America*, 2020, 148(1): 18-24.
- **Peng X**, He W, Xin F, et al. The acoustic radiation force of a focused ultrasound beam on a suspended eukaryotic cell. *Ultrasonics*, 2020, 108: 106205.
- Xu Z, **Peng X**, Liu X, et al. Modified theory of a microperforated panel with roughened perforations. *Europhysics Letters*, 2019, 125(3): 34004.
- **Peng X**, He W., Liu Y. F., et al. Optomechanical soft metamaterials . *Acta Mechanica Sinica*, 2017, 33(3):1-10

## Selected conference presentations

---

- Peng X, Genin G. Acoustic Radiation Force on Eukaryotic Cell Due to Standing Surface Acoustic Wave. Summer Biomechanics, Bioengineering, and Biotransport (SB3C), June, 2021, virtual meeting.
- Peng X, Genin G. Acoustic radiation force for cell manipulation. CEMB 3rd Annual Mechanobiology Symposium, January, 2021, virtual meeting
- Xiangjun Peng, Guy M. Genin, Tian Jian Lu. Standing surface acoustic waves, and the mechanics of acoustic tweezer manipulation of eukaryotic cells. Virtual Technical Meeting of the Society of Engineering Science 2020, September 29-October 1, 2020.



## **Teaching experience and computer literacy**

---

- Teaching Fellow for MEMS 255: Dynamics
- Bench mentor for CEMB boot camp
- Bench mentor for CEMB REU program
- Proficient in MATLAB, Mathematica, COMSOL, ANSYS, LS-DYNA